國立中山大學材料與光電科學學系

博士論文

Department of Materials and Optoelectronic Science

National Sun Yat-sen University

Doctorate Dissertation

CuZrAl-V/Co 金屬玻璃複合材料之微組織與機性分析

Microstructural and mechanical response of CuZrAl-V/Co bulk metallic glass composites

研究生：郭哲男

Che-Nan Kuo

指導教授：黃志青 博士

Dr. Jacob Chih-Ching Huang

中華民國 102 年 4 月

April 2013

論文審定書

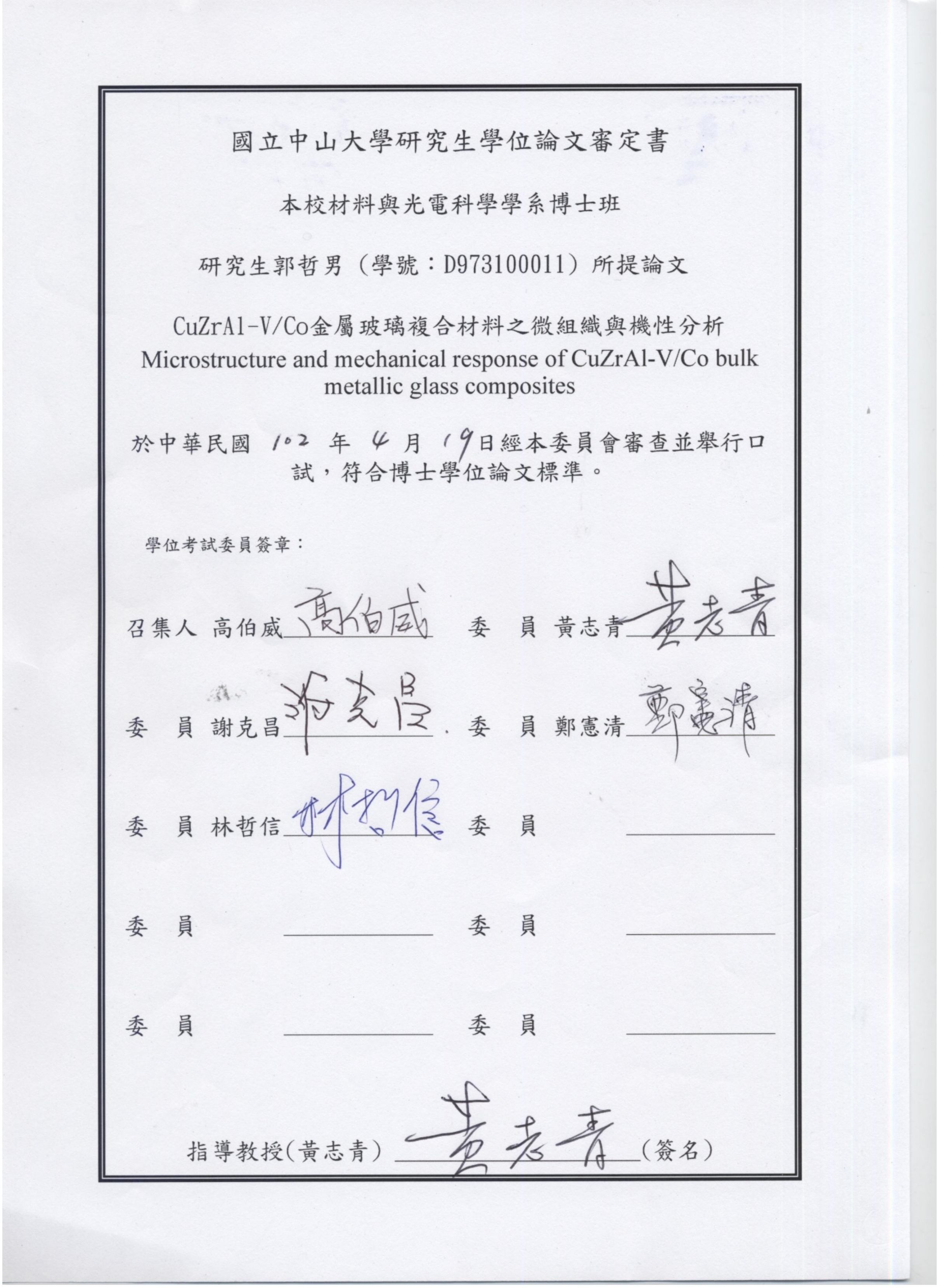

國立中山大學研究生學位論文審定書

本校材料與光電科學學系博士班

研究生郭哲男（學號：D973100011）所提論文

CuZrAl-V/Co金屬玻璃複合材料之微組織與機性分析
Microstructure and mechanical response of CuZrAl-V/Co bulk metallic glass composites

於中華民國 102 年 4 月 19 日經本委員會審查並舉行口試，符合博士學位論文標準。

學位考試委員簽章：

召集人 高伯威 高伯威　　委　員 黃志青 黃志青

委　員 謝克昌 謝克昌　　委　員 鄭憲清 鄭憲清

委　員 林哲信 林哲信　　委　員 ________

委　員 ________　　委　員 ________

委　員 ________　　委　員 ________

指導教授(黃志青) 黃志青 (簽名)

誌謝

從大學算起，待在中山大學材光系已經是第十個年頭了，如今的畢業，才真正是要離開這個地方了。在這十年裡，對我影響最大的，就是我的指導教授黃志青博士。從大學開始,我就跟老師十分熟識,每次上老師的課,下課以後我都不時找老師問問題聊天；到了大二做專題也是第一個就找老師，纏著老師不放直到老師收我為止；直到如今博士班即將畢業，老師依舊是我無話不聊的好朋友。而老師對我的影響是說不完的，學術上老師是我心中最屹立不搖的榜樣，他的熱忱、積極、毅力、對研究的敏銳度，樣樣都是我學習的好榜樣，老師除了指導我研究之外，私底下的每次聊天，更改變了我的個性與想法，使我成長。能在老師的指導下做研究，真的是很幸福的一件事，謝謝老師。

除了黃志青老師之外，在我的研究生生涯中，我受到了許多老師的照顧以及指導。首先我想感謝田納西大學的聶台岡教授，老師嚴謹而靈活的研究思維深深影響了我，跟老師合作論文時的討論更令我深受其惠，深深的改變了我研究上的思考模式以及研究方法。我想感謝我的師叔，中央大學材料工程研究所的鄭憲清教授，鄭老師常常在關鍵的時刻給我一記當頭棒喝，更在我最需要幫忙的時候提供我全力協助。感謝高伯威教授的指導以及幫忙，我一直都無法忘記當初校正 LVDT 的時候還麻煩了老師好幾次陪我做實驗，私底下一起打球一起聊天也讓我在低潮的時候能重新站起來。感謝謝克昌老師以及其研究團隊的幫忙，我幾乎所有的實驗都是在謝老師的實驗室裡完成的，在相圖方面更是受到老師相當多的指導。另外，我也想感謝沈博彥老師、張六文老師、徐瑞鴻老師、張志溥老師，雖然我並沒有受到老師們的指導，但是老師們都十分關心我，每次的談天後都讓我覺得我能在中山材光系念研究所真好，老師們對我真是太好了，謝謝老師。

除了老師們，我也要感謝瀋陽大學杜興蒿博士，杜博士是多次來我們實驗室擔任博士後研究員的學者，他對研究的投入、謙虛的態度、真誠的待人都深深影響了我，我的

研究更受到杜博士大大的幫助。還要感謝王良珠小姐以及李秀月小姐在實驗上以及儀器助教上的幫助；感謝系辦朱惠敏、顏秀芳和陳秀玉小姐在行政公務處理的幫忙；感謝華應騏大哥在做人處事上的分享以及教導；感謝黃谷正教官在公務上的幫忙以及照顧。

除了老師之外，在研究室裡最照顧我的，就是學長們，在我求學的不同時期，學長們總是給我最佳的典範以及最大的幫助。首先要感謝我的師傅，陳海明學長，海明學長從帶領我做專題研究開始，就一直是我效法的對象，當初我能通過博士班計畫書也是靠著學長的幫忙。感謝張育誠學長，除了一起吃漢堡王之外，每次路途中對於研究的討論總是讓我受益良多，是我的靠山。感謝時常笑臉迎人的洪子翔學長毫無保留的將他實驗技巧教導給我，更在我改裝實驗機台的時候給予我最大的幫助。感謝洪英博學長，雖然我們之間差最多屆，但是學長卻帶著我這個最小的學弟去買參考書，讓我覺得好溫暖。感謝李敬仁博士的教導，樹立了實驗室裡的榜樣。感謝張志溢學長時常的關心鼓勵。感謝鄭宇庭學長、賴炎暉學長把我像弟弟一樣照顧。感謝周鴻昇學長對我的督促以及嚴厲的指導。感謝實驗室雙帥裴浩然學長與劉名哲學長的提拔，你們就像溫暖的陽光一樣照亮我們。還要感謝我的肌肉同學宋大豪、實驗宅學弟官聖堯與保母陳盈翰，你們給我的幫忙真的是太多了。還要感謝實驗室裡所有的成員們，你們都是我的家人，感謝你們。

最後我要特別感謝我的父母以及家人們，在我求學生涯裡，他們無私的付出讓我能沒有後顧之憂的向著博士之路邁進，更在我最需要幫忙的時候給我最大的支援，謝謝你們，我愛你們。感謝我人見人愛的女朋友黃思庭，在我撰寫論文以及準備口試的期間給我最大的支持及鼓勵，有妳最棒的陪伴與笑容，是我每天的活力來源，謝謝妳。我還要感謝系排以及校排的所有成員們，在我求學生涯裡，你們對我來說是無可取代的夥伴，能當你們的隊友，是我的驕傲。

郭哲男 僅誌 於中山大學

摘要

CuZrAl、CuZrAl-V 與 CuZrAl-Co 合金經由吸鑄鑄造成金屬玻璃複合材料。首先 $Cu_{50}Zr_{43}Al_7$ 金屬玻璃由能量釋放的角度分析其應力-應變曲線下的鋸齒狀特徵以及破斷面與剪切帶之間的關連。為了鑄造微米尺度第二相之金屬玻璃複合材料，添加 3 至 10 原子百分比釩或鈷至 CuZrAl 合金中經由吸鑄法鑄造並分析其微結構以及機械性質。經由過飽和析出之富釩相形成尖銳尖端樹枝狀結構，導至應力集中並且降低了機械性質。另一方面，由於液態分離而形成的圓形富鈷相，由於其較低的應力集中現象而使機械性質得以提高或是維持。同時，添加 1 原子百分比之釩至 CuZrAl 合金中誘導了奈米尺度的 B2-CuZr 相，由研究發現少量添加釩之後，促使形成 B2-CuZr 相並提高了機械性質，並經由剪切帶增加、耗損能量、孿晶、應變誘導相變化以及晶粒粗化等不同的觀點分析其機械性質提升之機制。

由研究結果以及文獻參考發現，晶粒大小可能決定了應變誘導麻田散鐵相變化或是孿晶的發生與否，而晶粒大小與製程中所使用的模具吸鑄口的形貌有著相當大的關連，這項研究的最終任務是檢視尖銳或士鈍口模具對於鑄造後 B2-CuZr 相的大小以及金屬玻璃複合材料的機械性質之間的關係。由研究結果發現，當 B2-CuZr 相的大小大於關鍵尺寸後，會誘導形成麻田散鐵相變化或是孿晶，並且基於流體力學的理論建構出一個分析模型，經由與實驗結果的印證，發現模型與實驗之間的對照是十分令人滿意的。

關鍵字：金屬玻璃；複合材料；微結構；壓縮測試；鑄造；麻田散鐵相變化；孿晶

Abstract

CuZrAl and CuZrAl-V and CuZrAl-Co amorphous alloys were cast by rapid suction casting. Flow serrations and fracture morphologies of the base monolithic $Cu_{50}Zr_{43}Al_7$ bulk metallic glasses (BMGs) are first studied by compression at a low strain rate and analyzed by an energy release perspective.

Vanadium or cobalt from 3 to 10 at% is alloyed to the amorphous CuZrAl base alloys to induce precipitation in order to form the bulk metallic glass composites (BMGCs) with micro-sized second phase domains. The V-rich second phase formed during rapid cooling possesses a sharp dendrite shape, inducing stress concentration in the amorphous matrix and lowering the mechanical performance. The Co-rich phase, formed from liquid phase separation, possesses round morphology, lowering the stress concentration and raising or sustaining the mechanical properties.

Meanwhile, 1 at% vanadium was alloyed to the amorphous CuZrAl base alloy to induce nano-sized B2-CuZr phase formation in order to improve compressive plasticity. It was found that the dilute vanadium addition induced B2-CuZr formation and, thus, improved plasticity of the CuZrAl alloy. The role of vanadium on plasticity improvement was discussed in the frame of shear band multiplication, energy dissipation during shear banding, twinning/phase transformation of the B2-CuZr particles during deformation, and deformation induced B2-CuZr particle coarsening.

It was suggested that such transformation induced plasticity would show dependence on the B2 particle size, which in-turn depends on the inlet shape of the suction casting mold in use. It follows that the final task of this research was to examine the effects of the B2 size and distribution, resulted from the sharp or blunt inlet mold, on the mechanical plasticity in the CuZrAl and CuZrAlCo BMGs and BMGCs. It appears that the B2 particles need to be over some critical size to induce the martensitic/twinning transformation into the B19’ phase (sometimes with twins embedded). An analytic model, based on melt flow dynamics with or without vena contraction, is established, and the agreement between experiment and model is satisfactory.

***Keywords*:** metallic glass; composite; microstructure; compression test; casting; martensitic transformation; twinning

Content

List of Tables

List of Figures

Chapter 1 Introduction

1.1 Amorphous alloys

In contrast to crystalline materials, amorphous alloys are thermodynamically metastable materials and disordered materials that lack crystalline periodicity or are classified to lack the long-range-order (LRO) structure. Instead, higher degrees of short range order (SRO) than that in a liquid is maintained in the amorphous alloys. Due to such a structure, amorphous materials have also been called as metallic glasses, glassy metals, liquid metals, or non-crystalline metals.

When a liquid melt is cooled to a solid state slowly, the liquid melt would reach the equilibrium and solidifies into the lowest energy state structure, i.e. a crystalline lattice. By contrast, if a melted alloy is cooled rapidly, there would be not having sufficient time and energy to rearrange for heterogeneous atom nucleation. Thus, the liquid reaches the glass transition temperature and solidifies as an amorphous alloy. Hence, normally, high cooling rates are required to produce amorphous alloys in the form of ribbons, flakes, powders or rods. Furthermore, global researchers have discovered many methods to fabricate amorphous alloys by employing much lower cooling rates or various combinations of alloy compositions. By eliminating the limit of sample size to form the bulk metallic glasses (BMGs), they can expand their applications in engineering areas further. In general, BMGs need to measure a dimension over 1 mm. The largest BMGs so far reach 85 mm in billet diameter.

In comparison with crystalline materials, amorphous alloys exhibit a unique atomic structure without dislocations and grain boundaries. Due to such unique structure, amorphous alloys result in excellent properties in mechanical strength and toughness compared with those of the corresponding crystalline alloys. Moreover, bulk metallic glasses have attracted extensive interests over the past decades [1-7] due to following unique mechanical and physical properties: (1) high strength and hardness, (2) large limit of elastic deformation about 2%, (3) high elastic energy, (4) absence of distinct plastic elongation due to the inhomogeneous deformation mode, (5) good shaping and forming in the viscous state, (6) good fatigue properties, and (7) reasonable corrosion resistance. The fundamental characteristics and application fields of amorphous alloys are listed in Table 1.1 [1].

1.2 Bulk metallic glasses

Bulk metallic glasses (BMGs) have attracted wide attention because their unique properties, such as high strength, large elastic limit, good shaping properties in viscous state, and reasonable corrosion resistance [1, 5, 6, 8]. However, metallic glasses are also known for being extremely brittle, failing in a catastrophic manner, as a result of the formation of localized shear bands [2, 9]. In crystalline metals, the interactions of dislocations will produce strain-hardening and homogeneous deformation, thus, the crystalline materials can exhibit deformation stability and result in notable tensile plasticity. In comparison, due to the absence of the easy-slip deformation feature and good strain-hardening ability for most ductile crystalline alloys, strain-hardening or homogeneous deformation does not happen in BMGs during deformation. Thus, the plastic deformation in BMGs performs as an inhomogeneous deformation [2, 9].

Due to the localized shear band deformation in narrow zones when plastic deformation was initiated, shear bands propagate fast and cause the catastrophically fracture before or upon yielding, and are unable to accommodate remarkable plastic strain until failure [10, 11]. In tension, metallic glasses can be stretched elastically to typically about 2% of strain, followed by drastic shear-off fracture [9]. In compression, highly localized shear along the principal shear plane dominates and the materials usually exhibit shear softening and insufficient plastic strain [10, 12, 13].

To overcome the dilemma and extend the application in engineering fields, global researchers have made some efforts to improve the toughness of BMGs. The strategies for improving the mechanical properties have been developed and could be divided into two ways: one is intrinsic toughening for example by increasing the Poisson's ratio [14-16], and the other is extrinsic toughening by developing a composite microstructure within the glassy matrix, namely, forming the bulk metallic glass composites (BMGCs) [14, 17-22].

Recently, it was demonstrated that the plasticity of BMGs could be enhanced by introducing micron or nano-scale into the amorphous matrix [20-34]. For example, Pauly et al. [29-32] showed that the presence of B2-CuZr nanoparticles in a $Cu_{47.5}Zr_{47.5}Al_5$ alloy could apparently improve its tensile plasticity. The B2-CuZr nanoparticles, ~10 nm in the as-cast condition, were able to undergo twinning, phase-transformation, and coarsening (to about 50 nm) under deformation. These deformation processes could prevent from plastic instability and could dissipate energy, thereby improving the ductility. Wu et al. [33, 34] also demonstrated that a minor 0.5 at% addition of Co in the $Zr_{48}Cu_{47.5}Al_4Co_{0.5}$ alloy could further improve the tensile ductility, due to much larger spherical particles (or regions) up to 100 μm which contains ~80 nm B2-CuZr nanoparticles. In this Co-containing alloy, the strain hardening rate was enhanced and plastic instability was suppressed due to a B2-CuZr to

B19’-ZrCu martensitic transformation, similar to TRIP (transformation-induced plasticity) steels. The results show that BMGs have potential to exhibit remarkable plasticity for applications in many fields if some unique structures are inhered in.

1.3 Motivation

Bulk metallic glasses (BMGs) have attracted tremendous attention due to their unique properties, such as high strength, large limit of elastic deformation, good shaping properties in viscous state, and reasonable corrosion resistance, compared to their crystalline counterparts [1, 5, 6, 8]. The Cu-based BMGs have been developed due to the low cost and plastic nature of Cu. Recent developments on the Cu-based metallic glasses have resulted in several promising systems such as Cu-Zr-Ti [35, 36], Cu-Hf-Ti [36], and Cu-Ti-Zr-Ni [37], with high room temperature fracture stress ~2 GPa and elastic strain ~2%. Among them, the Cu-Zr-Al system was found to be a good candidate with high strength, high glass forming ability (GFA), and reasonable ductility [31, 38-40]. It is a suitable alloy system to study further.

However, such monolithic metallic glasses still do not exhibit sufficient and stable ductility at room temperature for industry application, owe to the localized and inhomogeneous shear band deformation at room temperature [2, 9]. The macroscopic deformation mode of BMGs is often closely associated with one single shear band along the principal shear plane. This macro principal shear band almost dominates the overall plastic deformation process until failure [12, 13]. In fracture morphologies, the characteristic of vein-like patterns spread over the fracture surface is a typical feature for BMGs. The reason for the formation of vein-like patterns can be attributed to the drop in viscosity within a shear band upon catastrophic failure. For BMGs compressed at low strain rates, the plastic region of stress-strain curve was always accompanied with numerous flow serrations.

In this study, before we try to find out how to improve the plasticity, we have to study the issue that why a shear band could cause the catastrophic failure. In the plastic region of stress-strain curve, the flow serration is obviously related with elastic energy releasing. Furthermore, the temperature rise by energy releasing, even reaching to the melt point of BMG, may play an important role in the local change of viscosity, which eventually leads to the vein-like patterns on the fracture surface. A BMG with a homogeneous glassy structure and reasonable plasticity is necessary for analyzing flow serrations and shear band propagation. Thus, flow serrations of BMGs during plastic deformation would be analyzed in an energy release perspective.

To clarify this issue, the monolithic Cu-Zr-Al BMG with a higher glass transition temperature (T_g) and melting temperature (T_m) is a good candidate for the examination of temperature rise. We estimate the energy release for one serration and for final catastrophic failure, and compare the difference in temperature rise. Fracture morphologies are also discussed based on the temperature rise.

After that, we have to find out how to stop or obstruct the propagation of shear band in order to prevent BMGs from catastrophic failure. As a result of the highly localized shearing in narrow shear bands along the principal shear planes, BMGs usually exhibit shear softening phenomena and the lack of sufficient plastic strain in their stress-strain curves [10, 12, 13]. The development of bulk metallic glass composites (BMGCs), either extrinsically by adding other second phases or intrinsically by promoting phase separation, nano/micro-scale precipitates, has been demonstrated to be a promising way in improving the plasticity.

Recently, it was demonstrated that the plasticity of BMGs can be enhanced by introducing nano-scale precipitates (or nano-scale particles embedded in micro-scale precipitate phase region) into the amorphous matrix [20-34, 41, 42]. In careful examination of the papers by Pauly et al. [29-32] and Wu et al. [33, 34], we note that the size of the B2 phase seems to impose some effects on the twining or martensitic transformation. The B2 particles smaller than about 25 nm in $Cu_{47.5}Zr_{47.5}Al_5$ [29] or about 80 nm in $Zr_{48}Cu_{47.5}Al_4Co_{0.5}$ [33] were not seen to exhibit twining or martensitic transformation.

Moreover, we notice that the influence of micro-sized precipitated phase on mechanical properties in different alloy systems could be varied with different compositions, sizes, volume fractions, or shapes of these precipitated phases. Among them, the second phase shape and morphology effects on mechanical properties of bulk metallic glass composites are of interest.

Thus, in this study, our major aim is to find out the more effective way to improve plasticity by introducing nano-scale precipitates or micro-scale precipitated phase. At the same time, it is of interest to explore what the critical size of the B2 particles is that would lead to twining or martensitic transformation induced plasticity.

In this study, two elements, V and Co, are introduced into the base CuZrAl bulk metallic glass. As shown in Table 1.2 [43], the mixing enthalpy of the binary Cu-V (+5 kJ/mol) or Cu-Co (+10 kJ/mol) system is positive and the mixing enthalpies of the other binary systems are all negative. Vanadium has similar thermodynamic features as Co with respect to the

Cu-Zr-Al system. Furthermore, minor addition of vanadium changes the crystallization mode to encourage the precipitation of Cu-Zr phase of the samples and leads to change of mechanical properties. However, glass forming ability of BMGs decreased with further increasing V content [44]. Furthermore, since the heat of mixing between the two major constituents in this system, Cu and Zr, is more negative than that between other elemental combinations, more B2-CuZr particles are expected when a small amount of V or Co is added to displace Cu from the amorphous matrix. It is suitable to examine the microstructure and mechanical response, particularly the possible occurrence of twining or martensitic transformation associated with such fine particles.

Furthermore, according to the simulated vertical sections as shown in Figures 1.1(a) and 1(b), there could be miscibility gap in the liquid state, containing two liquid phases L1 and L2. Our original goal was to cast a BMG with two glass phases. However, the V- or Co-rich liquid phase does not inherit with high glass forming ability, thus the V- or Co-rich region was found to be crystalline, imbedding in the CuZrAl-rich amorphous matrix and forming BMGCs. This allows us to examine and compare the mechanical response of these two BMGCs with different second phase shapes and morphologies.

Chapter 2 Background

2.1 The history of amorphous alloys

In 1960, Klement et al. [45] fabricated metallic glasses by using a splat quenching approach in the binary Au-Si alloy, as shown in Figure 2.1 [46]. It was recognized that this is the first method to rapidly quench from melt metallic liquid to metallic glass ribbons. Until 1970s, the technique of melt quenching was the major method to fabricate metallic glasses, and it had been extensively innovated to produce various metallic glasses. In 1970s and 1980s, the casting processes were developed to produce ribbons, wires, and sheets for the commercial manufacture [47]. Although the formation of metallic glasses was limited by high cooling rate, the development of metallic glasses still increased the attentions.

In 1970, Chen and Miller [48] produced uniform long amorphous alloy ribbon samples with 2 mm wide and 50 μm thick due to flattening out quenching of dropped alloys between two rotating wheels, as shown in Figure 2.2 [46]. This two roller technique removed the limitations of amorphous alloys, and it is a continuous process to be applied for preparing thin solidified films or foils.

In 1974, Chen et al. [49] produced amorphous alloy spheres of ternary alloy system in Pd-Si-N (N = Ag, Cu or Au). In the Pd-Cu-Si and Pd-Ag-Si ternary alloy system, some alloys showed the extended temperature interval in supercooled liquid region of 40 K. In addition, the $Pd_{77.5}Cu_6Si_{16.5}$ metallic glass could be fabricated in the millimeter scale in diameter (0.5 mm) and show the existence of glass transition. The results proposed by Chen et al. [49] enabled worldwide researchers to engage in the detailed studies in metallic glasses. At the same year, Chen [50] made systematic investigations on ternary Pd-T-P alloy systems (T = Ni, Co or Fe) and these alloys could be cast with a thickness of 1 mm. Even the Pd-Ni-P system was considered as the first production of bulk metallic glass (BMG) if one defines the millimeter scale as bulk [51].

In 1976, the chill block melt spinning method (CMBS) was developed by Liebermann and Graham [52], the method involves the formation of a melt jet by the elimination of a melt alloy through an orifice and the impingement of this jet against a rapidly moving substrate surface, as illustrated in Figure 2.3 [46]. The puddle which results from continuing impingement of melt jet serves as a local reserve from which ribbon is continuously formed and chilled. Among various rapid solidification processes, due to the simplicity in fabrication and effectiveness of rapidly solidified ribbons, the single roller chill block melt spinning becomes the most popular method.

In the beginning of 1980s, Drehamn et al. [53] subjected the samples to surface etching, followed by a succession of heating and cooling cycles. They decreased heterogeneous nucleation of crystals and then successfully produce BMG in $Pd_{40}Ni_{40}P_{20}$ with a diameter of 5 mm. In 1984, Kui et al. [54] used a boron oxide fluxing method to fabricate the $Pd_{40}Ni_{40}P_{20}$ BMG and successfully extended a critical casting thickness up to 10 mm.

In 1980, the planar flow casting (PFC) process was developed by Narasimhan and his coworkers [46], the schematic diagram is illustrated in Figure 2.4 [46]. The major difference between CBMS and PFC is that the nozzle of the PFC process is brought closer to the quenching wheel, so that the melt is more stable to suppress oscillation of puddle. Therefore, the PFC process not only allows a better control of ribbon dimension but also enhances process stability. Hence, it improves the quality of amorphous ribbons and makes wider amorphous ribbons easily.

In the late 1980s, the rare-earth materials with Al and Fe metals were investigated by Inoue's group of Tohoku University in Japan. They found a wide supercooled liquid region in the Al-La-Ni and Al-La-Cu alloy systems [55, 56] while they studied rapid solidification for these systems. The $La_{55}Al_{25}Ni_{20}$ alloy could be cast by the copper mold with water cooling into the cylindrical BMG samples with diameters up to 5 mm or sheets with similar thicknesses. Furthermore, the $La_{55}Al_{25}Ni_{10}Cu_{10}$ alloy was fabricated up to 9 mm in diameter by using the same method [57, 58].

Due to the cost and heavy weight of Pd metal, the light weight metallic glasses with the aim of improving the specific strength, such as Mg, Al, Ti and Zr-based alloys, were developed. In 1991, Inoue's group investigated the Mg–Cu–Y and Mg–Ni–Y ternary alloy systems. The largest glass forming ability (GFA) was found in the $Mg_{65}Cu_{25}Y_{10}$ alloy [59]. At the same time, the Zr–Al–Ni–Cu alloys with a high GFA and good thermal properties was developed by the same group, and the $Zr_{65}Al_{7.5}Ni_{10}Cu_{17.5}$ alloy showed the excellent critical casting thickness up to 15 mm and the extensive supercooled liquid region of 127 K [60]. In 1997, Inoue's group replaced 30% Ni (in at. %) by Cu in the $Pd_{40}Ni_{40}P_{20}$ alloy and produced an alloy with a diameter of 72 mm [61]. The Pd–Cu–Ni–P alloy system has been considered as a highest GFA alloy system. Figure 2.5 shows the critical casting thicknesses of metallic glasses over the years [62]. As show in Figure 2.5, the evolution of these alloys demonstrated that alloy composition plays an important role in the critical size of BMG.

Subsequently, Inoue [63] proposed the empirical rules to form BMGs with a high GFA and lower critical cooling rate. They succeeded in finding new multicomponent alloy systems mainly consisting of common metallic elements. With the contributions of the studies in metallic glasses, Inoue's group made many efforts in the development of metallic glasses. In 2000, the discovery of amorphous alloys with many engineering properties has been paid much attention. Inoue's group had done lots of extensive works on amorphous alloys about stabilization phenomena, crystallization behavior and fracture characteristics [1].

So far, many researchers have been searching for new alloy compositions to improve the thermal properties and mechanical behaviors and investigating the microstucture and deformation mechanism of these alloys. In 1999, Inoue et al. [64, 65] developed the high strength and good ductility composite with the amorphous matrix of Zr-Al-Cu-based BMG containing nanocrystalline phases. The mechanical properties of this alloy are better than those seen in some monolithic BMGs [64, 65]. After that, more and more global researchers paid attentions on the metallic glasses and metallic glass composites reinforced by nanocrystals.

2.2 The fabrication methods of amorphous alloys

During the past fifty years, amorphous alloys were fabricated by various methods and could be generally divided into three types [46]:

(1) from gas state to solid state: sputtering and vacuum evaporation

(2) from liquid state to solid state: splat quenching method, single or two-roller quenching process, spray forming process, chill block melt spinning process

(CMBS), planar flow casting process (PFC), casting method by a conventional metallic mold and high pressure die casting method

(3) from solid state to solid state: ion beam mixing, ion implantation, mechanical alloying (MA) and accumulative roll bonding (ARB)

In all the above mentioned methods, the liquid quenching method is the major method widely applied to fabricate different types of amorphous alloys such as powders, wires, ribbons and bulks. In liquid quenching method processing, the alloys are sucked, poured or injected into the casting mold with a high cooling rate of 10^3-10^8 K/s to result in amorphous alloys after a short period homogenization.

2.3 The forming condition of amorphous alloys

2.3.1 The glass forming ability

The amorphous alloys could be fabricated by a rapid quenching process when the quenching rate exceeds its critical cooling rate (R_c). Glass forming ability (GFA) is related to the ease of glass forming for the alloys, and the high GFA of alloy system means a larger size of amorphous alloys is obtained easily under a lower cooling rate. Moreover, GFA is very crucial indicator to understand the origins of glass formation and also important for designing and developing new metallic glasses.

The GFA is evaluated in terms of the critical cooling rate (R_c) for forming amorphous. The smaller R_c means the higher GFA of alloy system since the nucleation of a crystalline phase can be suppressed during solidification process with the minimum cooling rate. However, the parameter R_c is difficult to evaluate precisely. So far, worldwide extensive efforts have been devoted to study for a more simple and reliable criterion for quantifying GFA of amorphous alloys. Furthermore, many criteria have been proposed to describe the relative GFA of amorphous alloys on the basis of the characteristic temperatures measured by differential thermal calorimetry (DSC) or differential thermal analysis (DTA).

The most well known criterions are the supercooled liquid region, ΔT_x (= T_x-T_g, where T_x is the onset crystallization temperature and T_g is the glass transition temperature), and the reduced glass transition temperature, T_{rg} [66, 67] (= T_g/T_l, where T_g is the glass transition temperature and T_l is the liquidus temperature). Usually the ΔT_x and T_{rg} are popularly used as indicators of GFA for metallic glasses.

According to the DSC trace of the amorphous alloys in a heating process, there are two reactions before the alloys melt, one is the glass transition reaction with an endothermic phenomenon and the other is the crystallization reaction with an exothermic phenomenon. Therefore, the supercooled liquid region is defined as the region between glass transition temperature and crystallization temperature, which can be expressed as ΔT_x (= T_x-T_g). The region represents the thermal stability of alloy, i.e., the amorphous alloys with a wide ΔT_x exhibit a good thermal stability which indicates that metallic glass has superior resistance against crystallization from the supercooled liquid upon heating. Figure 2.6 [1] shows that R_c decreases with increasing ΔT_x so that the fabrication size of metallic glasses would be increased.

Another parameter is the reduced glass transition temperature T_{rg} (= T_g/T_l), proposed by

Lu et al. [66, 67], shows a better correlation with GFA than that given by $T_{rg}' = T_g/T_m$ [68] for BMGs, where T_m is the solidus temperature. The larger T_{rg} value leads a lower critical cooling rate to fabricate amorphous alloys, thus, the better GFA. Therefore, the tendency for R_c is prefer to decrease with increasing T_{rg}, as shown in Figure 2.7 [1]. In the viewpoint of T_{rg} (= T_g/T_l), selecting a proper composition close to deep eutectic point is useful for the probability of cooling fast through the supercooled liquid region and avoiding any occurrence of crystallization, thus, the GFA of the selected alloy system would be better. For most alloy systems, the glass transition temperature is affected slightly with the change of alloy composition, however, the liquidus temperature changes distinctly with changing the alloy composition. In other words, the reduced glass transition temperature T_{rg} exhibits a strong dependence on alloy composition.

Unfortunately, although both ΔT_x and T_g/T_l are used as indicators of GFA for amorphous alloys, not all amorphous alloy systems are suitable for using these two indexes to judge the degree of vitrification. Waniuk et al. [69] had confirmed that the parameter T_g/T_l is well correlated with GFA in Zr–Ti–Cu–Ni–Be alloys, whereas the glassy compositions with the largest ΔT_x are actually the poorest for glass formation. In other words, the ΔT_x value has no obvious trend with GFA in this alloy system. In addition, Inoue et al. [35, 36] also proved that the GFA for amorphous alloys is more related with T_g/T_l value in Cu-Zr-Ti ternary system rather than ΔT_x. Nevertheless, the reduced glass transition temperature T_g/T_l is not such reliable to relate with GFA in the $Pd_{40}Ni_{40-X}Fe_XP_{20}$ (X = 0 to 20) alloy systems [70], on the other hand, the supercooled liquid region ΔT_x is more reliable and useful criterion for the alloys fabrication in this alloy system.

Later, a new criterion with a purpose to infer the relative GFA among all BMGs was proposed by Lu and Liu [71, 72], which can be expressed as follows:

$$\gamma = \frac{T_x}{T_g + T_l}. \tag{2-1}$$

As illustrated in Figure 2.8 [71], to obtain an amorphous alloy with a better GFA, there are two main purposes must be considered. One is the stabilization of liquid phase, and the other is resistance of crystallization. While the amorphous alloy has a lower T_l, it represents that melting liquid phase can be maintained at low temperatures under a cooling step. When an amorphous alloy shows a lower T_g, the metastable glass phase of the alloy is more stable at low temperatures. Consequently, these two cases indicate that liquid phase is stability. On the contrary, a higher T_x of an amorphous alloy will lead a phenomenon that the glassy phase must crystallize at quite high temperature upon heating. Therefore, the three different characteristic phase transformation temperatures can be combined as the γ value. In addition, the critical cooling rate R_c (K/s) as well as critical section thickness Z_c (mm) can be connection with the γ value, as expressed by the following two equations:

$$R_c = 5.1 \times 10^{21} \exp(-117.19\gamma), \tag{2-2}$$

$$Z_c = 2.8 \times 10^{-7} \exp(41.7\gamma). \tag{2-3}$$

On the basis of these two equations, R_c and Z_c can be roughly estimated when γ is measured readily from DSC or DTA measurements.

The summary of supercooled liquid region ΔT_x, reduced glass transition temperature T_{rg},

γ value, critical cooling rate R_c and critical section thickness Z_c obtained by DSC and DTA for various alloy systems is listed in Table 2.1 [71]. In addition, the γ value reveals a stronger correlation with GFA than T_{rg} and has been widely applied to glass fabrication in the BMG systems.

Afterward, several parameters or criteria that are developed by different methods have continuously been proposed to evaluate the GFA for amorphous alloys, such as $\Delta T_{rg} = (T_x\text{-}T_g)/(T_l\text{-}T_g)$ [73], $\phi = T_{rg}(\Delta T_x/T_g)$ [74], $\delta = T_x/(T_l\text{-}T_g)$ [75]. Nevertheless, there are still not any reliable criteria to predict the GFA of metallic glasses in various alloy systems.

As aforementioned, the concept of forming amorphous alloys with better GFA is related to liquid phase stabilization ($\Delta T_x/T_l$) and crystallization resistance (T_x/T_l). The impression of lower liquidus temperature T_l to stabilize the liquid phase is similar to γ value. Therefore, higher GFA will be obtained with the lower T_l in the alloy systems, thus, GFA is proportional to $1/T_l$. In addition, since the larger ΔT_x exhibits more stability of the amorphous alloys and better GFA, GFA should be proportional to $(T_x\text{-}T_g)$. The relation between liquid phase stabilization and GFA is summarized as $(T_x\text{-}T_g)/T_l$. On the other hand, a higher crystallization resistance could be obtained with a higher crystallization temperature. With a normalization in order to result in a dimensionless parameter by T_l, GFA is proportion to the T_x/T_l value. According to these ideas, Du et al. [76] defined a new criterion which can be expressed as below:

$$\gamma_m = \frac{T_x - T_g}{T_l} + \frac{T_x}{T_l} = \frac{2T_x - T_g}{T_l}. \tag{2-4}$$

This γ_m value could be calculated easily according to the data on T_g, T_x and T_l measured by DSC and DTA and will be a simple and user-friendly indicator for GFA of BMGs. Similar to the γ value, the relationship between the γ_m value and critical cooling rate R_c (K/s) of amorphous alloys can be formulated as follows:

$$\log R_c = 14.99 - 19.441\gamma_m . \tag{2-5}$$

Since all related terms are reasonably and carefully considered for the liquid phase stability and crystallization resistance during glass formation processing, this γ_m parameter appears to reveal the best correlation with the GFA for BMGs among all parameters which have been reported before. It is believed that the statistical correction factor (R^2) can show effectiveness and consistency of various GFA parameters. Therefore, the higher R^2 value means the more reliable correlation between the proposed parameter and GFA. Based on the corresponding experimental data, the γ_m parameter exhibits the highest R^2 value among different GFA parameters. Thus, the γ_m parameter is seen to be the most reliable GFA parameter.

2.3.2 Empirical rules for the formation of amorphous alloys

Since the rapidly solidified amorphous phase is essential to suppress the nucleation and growth reaction of crystalline phase, the critical cooling rate (R_c) plays an important role in fabricating amorphous alloys. In other words, in the supercooled liquid region between the melting temperature (T_m) and the glass transition temperature (T_g), the higher the cooling rate, the lower the tendency to crystallize. Obviously, the critical cooling rate relates with the width of the supercooled liquid region, and it is also to correlate with the alloy compositions.

For an example of a binary system, most compositions of the amorphous alloys lie near the deep eutectic points. It is easy to understand by comparing the freezing of the two compositions, one is the composition away from the eutectic point and the other is near the eutectic point, as shown in Figure 2.9 [77]. The composition 1 which is located away from the eutectic point would cool through the liquidus line at a relative high temperature, thus the melt has to be cooled over a very large temperature range between the melting temperature and the glass transition temperature, which is possible to form and grow the crystalline phases. On the other hand, the temperature interval between the melting temperature and the glass transition temperature of the composition 2 which is near the eutectic point is relative small since the melt was cooled from the liquidus line at a relative low temperature, so that the thermal energy available for crystal growth is smaller and the tendency to suppress the nucleation and growth reaction of crystalline phase is larger than the other composition. Since the discovery of amorphous alloys, intense efforts have been made to understand the mechanism of amorphization for the prediction of alloy composition with better GFA and the correct designed alloy composition system would lead to metallic glasses with a cooling rate as low as 1-100 K/s.

In the past decade, the Inoue's group had developed a series of amorphous alloy systems with high GFA, and therefore they summarized and proposed three simple empirical rules for the alloy composition design to fabricate BMGs [1, 63]. The three rules are presented as follow:

(1) Multi-component system consisting of more than three main elements

If the alloy system with more than three main elements mixed together, the difference of atomic size will cause the retardation of moving atoms when quenching the melt into a solid state and the atoms cannot rearrange easily in the solidified process. Consequently, there exhibit a short-range order arrangement. The short-range order arrangement leads to denser the random packing so that the GFA of amorphous alloys will be improved with increasing the categories of the alloy main elements in such a multi-component system.

(2) Above 12% difference in atomic size ratios among the main constituent elements

According to the Hume-Rothery criterion [77], the condition to form a solid solution is that the difference of atomic size must less than about 12% between the solute and solvent. In such a condition of the atomic size difference is larger than 12%, the moving atoms will be retarded. Therefore, the viscosity of the melt increases so that the atoms cannot rearrange easily during the solidified process, as shown in Figure 2.10 [1].

(3) Negative heats of mixing among the main elements

According to the theory of thermodynamic, the heat of mixing is regarded as the atomic bending ability between two atoms in an alloy system. The larger the negative heat is, the weaker the bonding ability of the same atoms will be, but stronger the bonding ability for distinct atoms will be. Therefore, the distinct atoms tend to attract together and arrange in a random way when the liquid alloy is solidified with a large negative heat of mixing. Hence, when the alloy main elements have the larger negative heat of mixing, the amorphous alloys are easy to form.

When an alloy system satisfied with above three empirical rules, it will have a high solid/liquid interfacial energy which is favorable for the suppression of nucleation and growth of a crystalline phase, as illustrated in Figure 2.11 [1]. Therefore, it will have a higher dense degree of randomly packed atomic configurations in a supercooled liquid, and thus, it is difficult for the atoms in this liquid to rearrangement. It will lead the atomic diffusivity to decrease and the viscosity in a liquid to increase. Moreover, there always exhibits a high glass transition temperature T_g and very deep eutectic point with low liquidus temperatures T_l, leading to a high T_{rg} in such multicomponent alloys which satisfied with three empirical rules [1]. Due to these reasons, these empirical rules are certainly useful for selecting multicomponent alloy system to form BMGs. However, the development of new alloy systems for fabricating BMGs is still a very time-consuming process. In a multicomponent alloy system, hundreds of alloy compositions have been prepared and identified for glass formation, which is required to experimentally map out the GFA of every single composition in a given alloy system, in order to identify promising glass forming compositions. Thus, finding a more precise and specific criterion for the easy glass forming composition would be very useful and beneficial.

In order to form metallic glasses with a good GFA more easily, many other empirical criteria were reported. In the early work, Egami et al. [78] suggest that there is a correlation between the atomic volume mismatch of the constituent atoms and the minimum concentration of a solute in a number of binary amorphous. Based on this research, Senkov et al. [78] pointed out three main ideas: (1) the solvent element is selected with atomic radius of 0.15 nm or larger, (2) two or more solute elements are selected with atomic radii that correspond to the ratio of the radii of solvent and solute atom smaller than 0.88 or larger than 1.15, (3) the concentrations of the selected elements for an amorphous alloy are chosen in such a way that a concave upward atomic size distribution plot is produced.

Besides, Egami [78] proposed that there is a close relationship between atomic size and its concentration in certain metallic glasses. Fang et al. [79] also have suggested that an empirical criterion between bonding parametric functions which consists of atomic size parameters (δ) and electronegativity difference (ΔX) to the relationship and the width of supercooled liquid region of Mg-based bulk metallic glasses, as summarized in Figure 2.12. Shek et al. [80] have proposed that the composition of amorphous alloys and their crystalline counterparts should possess a constant value of e/a (the average valence electron number per atom number in a unit volume). In addition, Chen et al. [81] have suggested atomic size and e/a ratio as two criteria to find the best composition for BMG formation. Over and above, the electronegativity has also been used to explain the GFA of the Al- and Mg-based alloys, showing a nearly linear relationship with GFA.

Moreover, the composition of amorphous alloy appears to be an important factor for the GFA of BMG. Xi et al. [82] proposed a series of novel $Mg_{65}Cu_{25}RE_{10}$ BMGs (RE = rare earth elements, such as Gd, Nd, Sm, Dy) with different critical diameters and near eutectic compositions. In their result, the GFA of the Mg-Cu-RE alloy systems strongly depends on the electronegativity and atomic size of the RE elements. Besides, some studies have reported that minor alloying addition has shown dramatic effects on the glass formation and thermal stability of many BMGs [83, 84]. As proposed by Lu and Liu [84], adding a small amount of alloying additions (usually, less than 2 at%) into the existing BMGs leads a improvement of GFA. As indicated by the experimental evidence, alloy additions of small atoms with atomic radius smaller than 0.12 nm (such as B and Si) or large atoms with atomic radius larger than 0.16 nm (such as Y and Gd) are most effective in enhancing GFA of amorphous alloys. Further improvement of GFA has been reported in the Mg-Cu-Y alloy systems, when Cu is partially substituted with other alloy elements, such as Ag, Pd, or Zn, the GFA is improved. For example, $Mg_{65}Cu_{15}Ag_{10}Y_{10}$ [85], $Mg_{65}Cu_{15}Ag_{5}Pd_{5}Y_{10}$ [86, 87], $Mg_{65}Cu_{20}Zn_{5}Y_{10}$ [88] and $Mg_{54}Cu_{28}Ag_{7}Y_{11}$ [89] alloys all exhibit a high GFA and enabling the fabrication of BMGs in rods with diameters of 6, 7, 6 and 16 mm by a conventional Cu mold injection casting method, respectively. In the Mg-Cu-Ag-Gd alloy system, the $Mg_{54}Cu_{26.5}Ag_{8.5}Gd_{11}$ BMG [89] can also succeeded in the fabrication in a rod with a diameter of 25 mm. On the other hand, the Ma-based metallic glasses also shows remarkable effectiveness on the improvement of thermal stability and GFA with alloying additions of small atoms replacing Cu by B [90, 91]. The largest BMG billet so far is the Zr-based one measuring about 85 mm. In short summary, great efforts were made in the improvement of GFA by the addition of alloy elements on BMGs.

As aforementioned, the forming ability of BMGs becomes more matured under the great efforts of global researchers, and we can generalize a conclusion for the criteria of BMG formation. Generally speaking, it is easily to form BMG with a good GFA when the alloys satisfied with the following empirical rules: (1) the multicomponent alloy systems consist of more than three elements, (2) there is a significant difference, > 12%, in the atomic size ratios of the major constituent elements, (3) negative heats of mixing occur among the major elements, and finally (4) alloy compositions need to be close to the deep eutectic point.

2.4 Characterization of amorphous alloys

Since amorphous alloys have the disordered structure, they have unique physical and chemical properties which are different from the traditional crystalline alloys. The fundamental properties and the application fields of bulk amorphous and nanocrystalline alloys are summarized in Table 1.1 [1]. In addition, the various properties of amorphous alloy are described below.

2.4.1 Mechanical properties

Since the absence of long-range-order structure, metallic glasses exhibit the randomly atomic arrangement configuration and dense packing structure, only limited atomic displacements to resist deformation when an external stress is applied. As a result of the absence of dislocation and work hardening mechanisms in crystalline alloys, the metallic glasses exhibit some particular properties, such as the following: [1, 6, 7] : (1) high fracture strength (σ_f) and higher hardness compared with the corresponding crystalline alloys, (2) low Young's modulus (E) but much higher elastic deformation limitation of about 2% which exceeds the 0.2% yield limit of corresponding crystalline alloys, (3) high elastic energy up to the yield point compared with the corresponding crystalline alloys, and (4) absence of distinct plastic elongation due to the inhomogeneous deformation mode at room temperature, (5) good shaping and forming in the viscous state, (6) good fatigue properties. The fundamental characteristics and application fields of amorphous alloys are listed in Table 1.1 [1]. In addition, the relationship between tensile fracture strength, Vickers hardness and Young's modulus for various BMGs and conventional crystalline alloys is shown in Figure 2.13 [1]. There is a distinct difference in these fundamental mechanical properties between bulk amorphous alloys and conventional crystalline alloys.

Generally, BMGs have high tensile or compressive σ_f of 840-2100 MPa combined with E of 47-102 GPa, depending on alloy compositions [1]. Eckert et al. [31, 38, 39] successfully prepared Cu-based ductile BMGs and they show high strength (2265 MPa) and high ductility

(18%), as shown in Figure 2.14 [31, 38, 39]. Besides, this $Cu_{47.5}Zr_{47.5}Al_5$ metallic glass exhibits a ‘work-hardening’-like behavior during the compression tests, as shown in Figure 2.15 [31, 32, 38, 39]. By adding of 5 at% Al to the $Cu_{50}Zr_{50}$ glass increases the glassforming ability, and the thermal stability of the supercooled liquid. They also exhibit yield strength (1547 MPa) and good room temperature deformability. The intrinsic ductility is attributed to a heterogeneous amorphous structure, which enables easy and homogeneous nucleation of shear bands and their continuous multiplication during deformation. The interaction and intersection of the shear bands triggers their multiplication and increases the flowability of the BMG.

Under compression tests, sample geometry plays an important role in the formation of shear bands and the capability of plastic deformation [92-96]. If the aspect ratio (height to diameter) of cylindrical test sample is less than 1, shear band propagation is constrained and multiplication of shear bands is prone to form, so that the geometric effects would impose the improvement in the mechanical performance of BMGs and, thus, BMGs perform an apparent plastic strain more than 10%. This issue is not only existed in the ductile Zr-based BMGs with a higher Poisson ratio (0.35-0.4) [92-94, 96], but also in the brittle Mg-based BMGs with a lower Poisson ratio (0.3-0.35) [95].

As a result of inhomogeneous deformation, BMG samples always deform by highly shear localization and shear off at ~45^{o} with respect to the loading axis along a major shear plane with plastic strains < 2% in compression and essentially zero ductility in tension [11, 97]. Even in ductile Pd- or Zr-based systems, these BMGs still lack sufficient plasticity. However, global researchers made many efforts in the ductility of BMG. The results show that BMGs have potential to exhibit remarkable plasticity for applications in many fields if some unique structures are inhered in.

2.4.2 Magnetic properties

The two fundamental magnetic properties of materials are permeability and coercive force. In terms of permeability, magnetic materials can be classified as either soft or hard magnetic properties. For hard magnetic materials, they have the high remanence, coercivity and saturation flux density, as well as low initial permeability and high hysteresis energy losses. The muticomponent Gd-(Fe,Co), Tb-(Fe,Co), Nd-Fe(-Al) and Pr-Fe(-Al) [98-101] amorphous systems have been reported as hard magnetic materials that used for magneto-optical recording materials. On the other hand, soft magnetic materials are used in devices subjected to alternating magnetic fields and in which energy losses must be low such as the transformer cores. Based on the superior soft magnetic properties, magnetic glasses are usually applied as sensors for electronic article inspection. In addition, the sheets of glassy nanocomposites contain the nanocrystals in a glassy matrix, which are first produced by melt spinning and subsequently annealed. They still sustain their soft magnetic properties and higher saturation magnetization as well as a lower magnetostriction than the purely glassy materials. These magnetic glassy nanocomposites are currently used in transformer cores, magnetic sensors, and magnetic shielding [1, 63]. Soft magnetic amorphous alloys have also been prepared in muticomponent systems, like Fe-(Al,Ga)-(P,C,B,Si), Co-Cr-(Al,Ga)-(P,B,C), Fe-(Co,Ni)-(Zr,Nb,Ta)-B, and Co-Fe-Nb-B [102-106].

2.4.3 Chemical properties

The issue of corrosion is regarded as the weak point of polycrystalline materials since the corrosion always happen at the grain boundary. However, since the amorphous alloys do not have the defects in polycrystalline materials, such as the grain boundary, dislocation, and voids, the amorphous alloys are regarded as high corrosion resistance materials. In addition, the superior corrosion resistance of amorphous alloys could be further improved by adding alloy elements in an amorphous alloy, and even the stainless steel cannot catch up [107-111]. As proposed by Inoue et al. [1], the corrosion resistance is remarkably improved by the dissolution of Nb or Ta. In this study, the corrosion resistance of melt-spun amorphous alloys was examined in Zr-TM-Al-Ni-Cu (TM=Ti, Cr, Nb, Ta) systems in HCl and NaCl solutions.

Due to homogeneous single phase structure which is lack of grain boundaries, dislocations and other defects in crystals, amorphous alloys have outstanding corrosion resistance which is superior to the corresponding crystalline alloys. In addition, corrosion resistance could be improved by adding alloy elements in an amorphous alloy [107-111]. The corrosion resistance is the best for the Nb-containing alloy since the Nb- and Ta-containing amorphous alloys was found to exhibit good corrosion resistance in their solutions at room temperature. Due to the homogeneous microstructure, amorphous alloys with good corrosion resistance indicate they can be used in the fields of surgical and biomedical uses.

2.4.4 Other properties

Since amorphous alloys have the denser random packing structure than the corresponding crystalline alloys, amorphous alloys are good anti-radiation materials. Thus, the material structure does not change when bombarded by neutrons. The amorphous alloys also have the reasonable superconducting properties based on the electrical resistivity and critical field measurements, as reported by Li et al. [112, 113]. Moreover, the ability of hydrogen storage is also shown in many amorphous alloys, besides, their decomposing efficiency for hydrogen is up to 100% in Mg-based BMGs [114].

2.5 Mechanical behaviors of amorphous alloys

2.5.1 Stress-strain curves and fracture morphologies

The typical compressive and tensile stress–strain curves of $Zr_{59}Cu_{20}Al_{10}Ni_8Ti_3$ BMGs at different applied strain rates ranging from 4.5 x 10^{-5} to 3 x 10^{-2} s^{-1} at room temperature is shown in Figure 2.16 [97]. Under compressive test, BMGs show an initial elastic deformation behavior with an elastic strain of about 2% and then begin to yield, followed by some plastic deformation until fracture. However, in the tension test, BMGs show only an initial elastic deformation behavior and catastrophic fracture without yielding. In addition, the average tensile fracture stress of BMGs is slightly lower than the average compressive fracture stress. Moreover, the fracture stress of BMGs under tensile and compressive loading is insensitive to the applied stain rate of testing machine. In Figure 2.17 [115], shows the typical tensile and compressive fracture angle of BMGs. Generally speaking, the tensile and compressive fracture angles of most BMGs deviate from 45^o, and the fracture angle of BMG under tensile test is always smaller than 45^o. On the contrary, the compressive fracture angle is always larger than 45^o [11, 97, 116].

Even though tensile and compressive samples similarly fractured in a shear mode, the fracture morphology is distinctly different between compression and tension test. Figure 2.18 [97] shows the typical tensile and compressive fracture morphologies of the BMG fracture surfaces [11, 97, 116]. In Figure 2.18(a) [97], the tensile fracture surface reveals not only the so-called vein-like structures, but also the circular core structures. It is well known that, uniaxial tensile stress can be decomposed into the resolved shear stress along the failure plane and the resolved normal stress perpendicular to the failure plane. The resolved normal stress is outward the fracture plane, leading to the formation of circular cores, as indicate by the arrows in Figure 2.18(a) [97]. Subsequently, the resolved shear stress along the failure plane causes the veins propagation far away from the circular cores.

On the contrary, the flat fracture surface and vein-like structure are observed in the compressive fracture surface, as shown in Figure 2.18(b) [97]. The vein-like structure which spread over the whole fracture surface is the typical feature of fracture surface under compressive loading. Similarly, uniaxial compressive stress can also be decomposed into the resolved shear stress along the failure plane and normal stress perpendicular to the failure plane. The resolved normal stress is inward the fracture plane so that it is unable to produce a circular core in fracture plane, whereas the shear stress still yields the formation and propagation of veins. In addition, the vein-like structure always extends along the shear direction that parallel to fracture plane, as indicated by the arrow in Figure 2.18(b) [97].

2.5.2 Temperature effect

The mechanical behaviors of BMGs can be classified into two typical types, which are inhomogeneous deformation at room temperature and homogeneous deformation at a high temperature within the supercooled liquid region [117, 118]. The steady-state strain rate as a function of stress and temperature, of a metallic glass is illustrated in the schematic deformation mechanism map of Figure 2.19 [118]. The mechanical behaviors of BMGs at room-temperature uniaxial mechanical tests during inhomogeneous deformation have been described above. On the contrary, the mechanical behaviors of BMGs at high temperatures and low stresses usually perform a homogeneous deformation and an apparent plasticity phenomenon.

The homogeneous deformation can be divided into three parts based on the viscosity of the material [118]. Firstly, for $T > T_l$, the material has a viscosity of ~10^{-3} Pa·s and can be characterized as "fluid" or "liquid" matter. In this region, the viscosity changes slowly with temperature and the strain rate contours are almost horizontal. Secondly, for $T \approx T_g$, the material has a viscosity between 10^{15} and 10^{-10} Pa·s and can be called as "viscous" matter. In this region, the viscosity drops very fast with increasing temperature, and the strain rate contours are almost vertical around T_g. Finally, for $T < T_g$, the material has a viscosity above 10^{15} Pa·s and can be called as "solid" matter. In this region, viscosity does not change very fast with increasing temperature and the strain rate contours become more horizontal.

In compare with the localized shear bands dominated inhomogeneous deformation of BMG at room temperature, the deformation of BMG at high temperatures usually performs a homogeneous deformation. Above a critical temperature of T_g, the homogeneous deformation of BMG will start as an ideal Newtonian viscous flow and the strain rate sensitivity m value will be equal to 1 in the following constitutive equation:

$$\sigma = k\dot{\varepsilon}^{m} , \tag{2-6}$$

where σ is the yield stress, k is a constant, and $\dot{\varepsilon}$ is the strain rate. In this supercooled liquid region, BMG will exhibit the superplastic-like behavior. Due to the the superplastic-like behavior, easy formability enables the BMG to be potentially produced for micro-electro-mechanical systems (MEMS) in the micrometer and nanometer scale, as shown in Figure 2.20 [119, 120].

On the contrary, the cryogenic temperatures mechanical behaviors of BMGs have been recently presented by Li et al. [121, 122] for comparison with those at room temperature. Compared to room-temperature compression, the uniaxial compression tests of Zr-based BMGs at the ambient (300 K) and cryogenic (77 K) temperatures were performed and the resulting strength of Zr-based BMG increases at the cryogenic temperature but is accompanied by the decrease in plastic strain, as shown in Figure 2.21 [121]. And the dependence of strength variation as a function of testing temperatures in compression and microhardness is shown in Figure 2.22 [121]. In the further work, the fracture morphologies of deformed samples at 300 and 77 K demonstrate a combination of two types of vein patterns, one is the void-like and the other is river-like, indicating that fracture surface is independent of the testing temperature, as illustrated in Figure 2.23 [122]. Based on the results, Li et al. [122] proposed a linear relationship between the normalized strength (σ/E) and normalized temperature (T/T_g), which can be expressed as the following:

$$\frac{\sigma}{E} = 0.0253 - 0.0106\frac{T}{T_g}, \qquad (2\text{-}7)$$

where E is elastic modulus, T_g is the glass transition temperature and T is the testing temperature, as presented in Figure 2.24 [122]. Since the E and T_g are constants for most of amorphous alloys, the strength of BMGs increases with decreasing temperature.

2.5.3 Strain rate effect

Recently, the issue of the strain rate effects on the deformation behaviors of BMGs was had been studied and reported [123-126]. The strain rate effects on fracture morphologies of Zr-based BMGs under tension test was studied by Xiao et al. [125]. The typical vein-like, circular core and ridge-line structures appear on the fracture surface of the $Zr_{52.5}Al_{10}Ni_{10}Cu_{15}Be_{12.5}$ BMG in tension at low strain rates, as shown in Figure 2.25 [125]. At low strain rates, the shear bands propagate rapidly once the localized shear bands form, and the encounter of the neighboring shear bands results in the formation of ridge lines. These ridge lines of shear bands ultimately turn off and cause the catastrophic failure. On the contrary, at high strain rates, the fracture morphologies under tensile deformation almost consisted of microvoid-coalescence dimples caused by a localized melting mechanism during deformation process, as shown in Figure 2.26 [125]. In the other study, as reported by Mukai et al. [115], the flow serration of stress-strain curves disappeared when the applied strain rate is over a critical value. At high strain rates, BMG display weakening and fragility due to the absence of multiple shear band formation.

As proposed by Jiang et al. [127], the in-situ dynamics shear-banding operation of the geometrically constrained BMGs (height to diameter ratio = 0.5) at various strain rates was observed by using an infrared camera. And the dependence of stress as a function of the Zr-based BMGs for the flow serrations of stress-strain curves at various strain rates is presented in Figure 2.27 [127]. As compared with these curves, the serrated flow phenomenon is prone to temporarily decrease with increasing strain rate. As shown in Figure 2.28 [127], the higher strain rate, the fewer shear band and coarser shear band spacing were observed on the sample appearance. Due to these results, the shear band tends to decrease with increasing applied strain rate.

2.5.4 Sample size effect

Based on the literatures [128-137], when the sample size is reduced down to a critical size, the BMG generally presents the enhanced strength and plasticity, compared with the larger one, with the same chemical composition under compression test. Zheng et al. [128] presented that when the conventional compression tests were conducted on the $Mg_{61}Cu_{28}Gd_{11}$ BMG with a diameter as large as 4 mm and as small as 1 mm for comparison, the samples with 1 mm in diameter exhibit a higher strength and plasticity than those with 4 mm in diameter. As well known, all reported Mg-based BMGs are of the brittle nature, indicating that their plastic strain before failure is either nonexistent at all or very small under compression test. As reduced the sample size down, the probability of finding defect is very low, such as pores, un-melted particles, oxides and inclusions, so that it is beneficial to measure the intrinsic strength and plasticity for the sample with a smaller critical size. Table 2.2 [128] summarizes the previously reported mechanical properties of Mg-based BMGs under compression tests. In addition, Huang et al. [137] also reported that the plasticity of Ti-based BMG tends to increase with decreasing sample size from 6 mm to 1 mm in diameter. With a smaller sample size, there is concerned with a higher amount of free volume formed by a relatively faster quenching during solidification, so that results the better outstanding mechanical performance of BMG. The same dramatic effect have also been seen in the Zr-based BMGs [129, 131], it can generally give a conclusion that the smaller one is more ductile.

Recently, the sample size was reduced to micrometer scale as the BMG micropillars

[132-136]. As proposed by Huang's group [135, 136], the smaller size-scaled BMG micropillars was tested by microcompression to explore sample size effect on mechanical properties. The sample size effect on the yield strength of the ductile Zr-based BMG micropillars with diameters of 1 and 3.8 μm was found to be highly sensitive to sample size [136]. The similar effect was also observed from the brittle Mg-based BMG micropillars [135]. In addition, the yield strength of the BMG micropillars was found to exhibit a 30-100% increment over that of the bulk samples. As discussed first by Schuster et al. [134] and later by Lee et al. [135] and Lai et al. [136], the increase in strength with decreasing sample size can be rationalized by the Weibull statistics which is able to determine the intrinsic strength and plasticity of BMG at the situation of small sample sizes.

2.5.5 Geometric constraint effect

Under room-temperature compression test, the sample geometry significantly plays an important role in mechanical behaviors of BMG [92-96, 138-142]. The strength maintains almost invariable due to geometric constraint effect. Since the compressive plastic strain of cylindrical ductile Zr-based BMG sample commonly increases with decreasing aspect ratio [92-96]. For unconstrained samples with a higher aspect ratio which is larger than 1, shear bands can operate freely throughout the whole diameter of sample, resulting in the smaller plastic strain before failure. On the contrary, shear bands is not able to operate freely throughout the whole diameter of the constrained sample as the aspect ratio is lowered down to less than 1, so that these samples are characterized by larger plastic strain. In other words, when the shear band propagation is constrained by the upper and bottom platens during the early stage of compression, the multiplication of shear bands will tend to form, resulting in the apparent ductility. Moreover, the dependence of yield strength and plastic strain is a function of aspect ratio of the BMGs, as shown in Figure 2.29 [92].

In addition, the geometric effect could also be observed in the brittle Mg-based BMGs. As proposed by Chen et al. [95], the room-temperature compression tests were conducted on the Mg-based samples with various h/d ratios from 2, 1, 0.5 to 0.25. When the h/d ratio is 2, the fracture surface shows cleavage features, as the typical characteristic nature of the brittle Mg-based BMGs. However, when the aspect ratio is reduced to 0.25, the plastic strain is significantly enlarged up to 20% and the highly dense vein-like structures spreading over the whole fracture surface is observed, as shown in Figure 2.30 [95]. Hence, as decreasing the aspect ratio, the plastic strain is increases in most BMGs.

In addition, the aspect ratio of sample would influence the shear band propagation and the mechanical responses of BMGs, the sample alignment and geometric shape, leading to lateral motion resistance and longitudinal constraint, influence the mechanical behaviors of BMG as well [138-141]. To research the geometric effect, Wu et al. [139] proposed the concept of ‘‘stress gradient enhanced plasticity’’ for the moderation of catastrophic failure in a large stress gradient exists of various geometries BMG samples, such as orthogonal, monoclinic and transitional. Their results are shown in Figure 2.31 [139]. For the ideal orthogonal sample, the constant stress gradient indicates there appears high stress concentration throughout the whole sample during deformation. On the contrary, for the monoclinic and transitional samples, the stress concentration is localized in two opposite corners of sample. Hence, the lateral motion resistance and longitudinal constraint may restrict sample further sliding along the shear plane, resulting in the enhanced plastic strain. In the other words, the plastic strain enhancement is an artifact. The results suggest that the sample preparation and alignment during machine testing should be taken special care in order to avoid any artifact plasticity of BMGs.

2.5.6 Deformation mechanisms of metallic glasses

As well known, during deformation process, crystalline alloys would perform elastic deformation, followed by yielding, and then start plastic deformation when the resolved shear stress is over the critical resolved shear stress (CRSS) along a specific slip plane, finally, the alloys would fracture. During the plastic deformation, the dislocation is formed and starts to move along the slip direction of a slip plane in the crystalline alloys. In compared with the crystalline alloys, there is no slip system for plastic deformation in the metallic glasses due to the absence of long-range order periodically.

As shown in Figure 2.32 [10], in the two-dimensional schematic diagram of atomic deformation mechanisms for metallic glasses, there are numerous small spaces between atoms which are called free volumes. Unlike crystalline alloys, metallic glasses only allow small displacement change in atomic neighborhood under applied loading, and the local rearrangement of atoms is a relatively high energy and high stress process. Hence, the feature of metallic glasses presented the absence of sufficient plastic deformation in their stress-strain curves. To make a metallic glass to further deform, a larger applied stress would often be required so that the clusters of atoms tend to move together by a dominant shearing like a band, and it is called shear band.

In terms of the plastic deformation of metallic glasses, it could be classified into two types: one is slight plastic deformation with the nominal work softening, and the other is distinct plastic deformation accompanied with flow serrations observed in the strain-stress curves. The flow serration phenomenon indicates the operation of localized shear band deformation. Under the uniaxial compressive or tensile tests, once shear localization has begun, there would be a highly localized shearing in a narrow band, and the trend for shear-softening would urge deformation in order to accommodate some shear strains and finally the sample would fail along one major and dominant shear plane [10]. Hence, the plastic deformation of metallic glasses is inhomogeneous at room temperature due to the highly localized shearing [2, 9].

In 1977, Spaepen [118] applied the free volume model, which proposed by Turnbull and his coworkers [143, 144], to the case of glassy and interpreted the local rearrangement of atoms in metallic glasses during deformation. Subsequently, Argon [145] further proposed a concept in 1979 to demonstrate that the deformation mechanism for metallic glasses is atomic-scaled shear distortion from the viewpoint of free volume model. This theory is based on the "shear transition zone" (STZ), which is defined as a thermally activated shear band initiated around free volume regions under an applied shear stress. The STZ is a local cluster of atoms that undergoes an inelastic shear distortion from one relatively low energy configuration to a second configuration, passing an activated configuration of higher energy and volume [10]. Moreover, the free volume site and its adjacent atoms are considered as a basic shear unit for metallic glasses under an applied shear stress to produce shear deformation, as illustrated in Figure 2.33 [146]. STZs which approximately consist of a few hundreds of atoms in volume are usually observed in simulation works, which stretch over the variety of simulated compositions and empirical inter-atomic potentials [147-150]. Unlike the dislocation in crystalline alloys, which is a defect of atomic arrangement, the STZ is a usual event for the deformation of metallic glasses and not a structural defect in metallic glasses. Otherwise, STZ is called as flow defect.

The STZ is not a feature of glass structure and STZ is an event defined as an event in local volume by its transience. From the viewpoint of the activation of kinetic energy, when a metallic glass is subjected to an applied shear stress which is over a critical value, a single STZ first nucleates in the vicinity of a free volume site without significant atomic rearrangements in its surrounding glassy matrix. Subsequently, secondary STZs may occur in the vicinity of the first STZ by the assistance of a local strain field and free volume formed by the first STZ, and the later formation of STZ will follow a similar manner. Once the critical number of STZs reaches a maximum in the initial zone, the shear band that consists of these local STZs starts to propagate, resulting in the macroscopic yielding of metallic glass [151]. It suggests that the amount and distribution of free volume may dominate the plastic deformation of metallic glasses since the higher free volume sites would more readily to accommodate shear band.

Moreover, the moving of STZ is always accompanied by the releasing of adiabatic heat near the STZ [152-157]. The temperature around the shear plane will be risen if more and more STZs start moving along a shear plane. The temperature may reach the glass transition temperature and the fluid region or re-solidified-like droplets will be formed on the shear plane.

2.6 Strategies to improve mechanical properties of metallic glasses

The strategies for improving the mechanical properties have been developed and could be divided into two ways: one is intrinsic toughening by increasing the Poisson’s ratio [15, 16], and the other is extrinsic toughening by developing a composite microstructure within the glassy matrix [14, 18-22].

To improve the plasticity of BMG, BMG composites (BMGCs) have been developed by the extrinsic toughening method developing a composite microstructure within the glassy matrix [11, 14, 32, 64, 65, 158-162]. In the extrinsic toughening method, the second phase can be the precipitated crystalline phases [64, 65, 158-160], in-situ precipitation of dendrite phase [14], metal fibers [11], glassy state alloys [22-25, 163, 164], or finely dispersed porosities [161]. The second phase can act as a block to prevent shear bands from free propagation. Hence, the catastrophic failure can be retarded through the interaction between reinforcements and initially formed shear bands.

A precipitated crystalline phases Zr-Cu-Pd-Al BMGC was proposed by Fan and Inoue [65]. With various volume fraction of precipitated crystalline phases, $Zr_2(Cu,Pd)$, via annealing under compression test, they found that the plastic strain of the $Zr_{60}Cu_{20}Pd_{10}Al_{10}$ BMGC can be improved in comparison with that of the as-cast $Zr_{60}Cu_{20}Pd_{10}Al_{10}$ BMG while no distinct plastic strain is recognized in the $Zr_{55}Ni_5Cu_{30}Al_{10}$ BMG, as shown in Figure 2.34 [65]. As shown in Figure 2.35 [65], the summarized mechanical properties of the $Zr_{60}Cu_{20}Pd_{10}Al_{10}$ BMGCs shows an increase in the compressive yield strength, maximum fracture strength, Young’s modulus and plastic strain with increasing volume fraction of crystals. The plastic strain of the $Zr_{60}Cu_{20}Pd_{10}Al_{10}$ BMGCs significantly deteriorates down to 0% when volume fraction of crystals exceeds a critical value (27%), it indicates that the appropriate volume fraction of reinforcement is a key point for the ductility improvement of BMGCs.

In the representative brittle Mg-based BMG, the mechanical properties were improved by the reinforcement of ductile Nb particles with 20-50 μm in size. The result shows a high strength of 900 MPa and large plasticity of 12%, as shown in Figure 2.36 [165]. Pan et al. [165] proposed that the ductile Nb particles can effectively retard the shear band propagation to prevent from catastrophic fracture. In Figure 2.37 [165], the deformed Nb particles uniformly distribute loading and surrounding BMG matrix to promote the initiation and branch of numerous secondary shear bands.

Kim et al. [23] proposed that the phase separation into Y-rich and Zr-rich amorphous phases occurs during cooling when the Y content is above 15 at.% in $Cu_{46}Zr_{47-x}Y_xAl_7$ alloys. As shown in Figure 2.38 [23], the two-phase amorphous alloys exhibit extreme brittleness, while the single-phase amorphous alloys (x = 2, 5) exhibit enhanced plasticity from the introduction of local chemical inhomogeneity, although the microstructure consisted of an amorphous structure without any structural ordering within the resolution of high-resolution transmission electron microscopy (HRTEM) (Figure 2.39(a) [23]). However, the local compositional fluctuation in the BMG with x = 5 can be evidenced from the occurrence of phase separation during solidification with further increasing Y content. As shown in Figure 2.40 [23], A local increase of viscosity and exothermic reaction in the supercooled liquid region support the conclusion that chemical inhomogeneity in the BMG sample with x = 5 leads to the formation of nanocrystals (Figure 2.39(b) [23]) in the supercooled liquid region. The results suggest one effective way of improving the plasticity of BMGs. That is to add an element (elements) having a positive enthalpy of mixing with the constitutive elements; however, this is only effective within a limited composition range, as reported by Du et al. [13, 24, 25] and Wang et al. [16].

In the above-mentioned studies, excellent mechanical performances, such as remarkable strength and macroscopic plasticity, could be improved in these BMGCs. Hence, BMGCs have great potential in serving as engineering materials.

2.7 The development of Cu-based metallic glasses

Due to Inoue's great efforts [1, 43, 63], more and more global researchers paid attentions on the metallic glasses. After that, Cu-based BMGs are studied by world wide researchers due to the low cost and plastic natural of Cu. Many alloy systems of Cu-based metallic glasses such as Cu-Zr-Al [166, 167], Cu-Zr-Al-Ag [166, 167], Cu-Zr-Al-Gd [164], Cu-Zr-Al-Be [167], Cu-Zr-Ti [35, 36], Cu-Zr-Ti-Ag [168], Cu-Zr-Ti-B [169], Cu-Zr-Ti-B-Si [169], Cu-Zr-Ti-Sn [170], Cu-Ti-Zr-Ni [37], Cu-Ti-Zr-Ni-Si [171], Cu-Ti-Zr-Ni-Sn [172], Cu-Hf-Al [173], Cu-Hf-Al-Ag [173], and Cu-Hf-Ti [36], have been developed by the global researchers' great efforts.

Developments of Cu-based metallic glasses such as Cu-Zr-Ti [35, 36], Cu-Hf-Ti [36], Cu-Ti-Zr-Ni [37] with high room temperature fracture stress (~2 GPa) and elastic strain (~2%) have increased expectations for the application of BMGs, considering their low cost. However, like other metallic glasses, they show poor ductility at room temperature. To extend the applied engineering fields, it is necessary to improve the mechanical properties of monolithic BMGs. Subsequently, by adding of 5 at% Al to the $Cu_{50}Zr_{50}$ glass, Eckert et al. [31, 38, 39] successfully prepared Cu-based ductile BMGs and they show high strength (2265 MPa) and high ductility (18%). After that, Cu-Zr-Al alloy system has been paid attention due to the high fracture strength and high ductility. Global researchers made great efforts on the mechanical properties of the Cu-Zr-Al alloy system with an addition of other elements, as shown in Table 2.3 [23, 31, 38, 39, 164, 166].

The Cu-V-Zr-Al and Cu-Co-Zr-Al alloy systems have not been widely studied until now. In these two alloy systems, the heat of mixing is positive between Cu-Co and Cu-V but negative between other two elements. The positive heat of mixing promises a potential to cast a phase-separated BMGs in these two alloy systems. It is worth to study the shear band deformation mechanism and serration phenomenon of phase-separated BMGs during plastic deformation.

2.8 Deformation induced martensitic transformation of CuZr B2 phase

Cu-Zr-Al system was found to be a good candidate with high strength and high glass forming ability (GFA), and reasonable ductility [29-34, 38-40]. In order to improve the plasticity of BMGs, micro- or nano-scaled particles were introduced into the amorphous matrix [22-25, 27-34, 38-42]. In the research of Wu et al. [33, 34], tensile ductility was demonstrated in the $Cu_{47.5}Zr_{48}Al_4Co_{0.5}$ alloy due to the large 100 μm spherical region full of small 80 nm B2 particles, as shown in Figure 2.40(d). In the study of Wu et al. [33], the XRD trace of the as-cast specimens is typical for a BMG composite; crystalline phase peaks identified as the B2 phase are superimposed on the amorphous hump, however, the XRD pattern of the fractured samples exhibits different sharp peaks which can be identified as the martensite CuZr phase (i.e., the B19’ phase), suggesting that the martensitic transformation from B2 to B19’ has occurred during the tensile deformation, as shown in Figure 2.40(a). Also, the comparison of the cross-sectional features of the crystalline phases between the as-cast (Figure 2.40(b)) and fractured specimens (Figure 2.40(c)) provides further evidence for the occurrence of the stress-induced martensitic transformation. The TEM results also demonstrate that martensitic transformation had happened so that, after the tensile tests, the nanometer-sized crystalline monoclinic martensitic phases is shown in the fractured samples, as presented in Figures 2.40(d) and (e). The similar result is also shown in related studies. [29-34, 174]

The minor addition of Co by only 0.5 at% appeared to impose a great effect on precipitated particles due to the positive mixing enthalpy of binary Cu-Co while the mixing enthalpy of other binary constituents are all negative in the Cu-Zr-Al-Co system. Such micro-scaled regions full of B2 particles were shown to play an important role in enhancing the strain hardening rate and in suppressing plastic instability, as a result of the B2-CuZr (of the ordered body-centered cubic, BCC, structure, with a lattice constant a = 0.3262 nm) to B19'-ZrCu (monoclinic, a = 0.3278 nm, b = 0.4161 nm, c = 0.5245 nm, and $\beta = 103.88^o$) martensitic transformation, as shown in Figures 2.41 and 2.42 [175, 176], similar to TRIP (transformation-induced plasticity) steels. Meanwhile, the ~25 nm B2-CuZr nanoparticles in a $Cu_{47.5}Zr_{47.5}Al_5$ alloy (with no Co), reported by Pauly et al. [29], were seen to be able to undergo twining, phase-transformation and coarsening (to ~50 nm) under deformation. The twining, phase-transformation and coarsening processes could prevent from plastic instability and improve tensile ductility.

Chapter 3 Experimental procedures

In this study, raw materials were melted together and then suction cast into the bulk monolithic BMG and BMGC samples. Mechanical behaviors were studied and discussed among these specimens. The mechanical properties of the Cu-based BMGs compressed at room temperature and a low strain rate were investigated. To shed light on the shear-band dynamics, the flow serration and shear band propagation during inhomogeneous deformation of BMGs was analyzed in an energy release perspective. The flow chart of experimental procedures is displayed in Figure 3.1.

3.1 Raw materials

In this research, the compositions of $Cu_{50}Zr_{43}A_7$, and $(Cu_{47.5}Zr_{47.5}Al_5)_{100-x}V/Co_x$ (x = 0, 1, 3, 5 and 10) were selected for preparing the monolithic BMGs and BMGCs. The pure elements in bulk or piece form were selected to prepare the preliminary metallic glasses samples. The purities of pure elements copper, zirconium, aluminum, vanadium, and cobalt are all as pure as 99.99%. Table 3.1 lists the fundamental data related to the component elements.

3.2 Computational thermodynamic approach

In this study, two elements, V and Co, are introduced into the base CuZrAl bulk metallic glass. As shown in Table 1.2 [43], the mixing enthalpy of the binary Cu-V or Cu-Co system is positive and the mixing enthalpies of the other binary systems are all negative.

To further predict the composition of BMGCs, the computational thermodynamic approach was introduced to identify the two-liquid miscibility phase equilibrium in the liquid-temperature region for the Cu-V-Zr-Al and Cu-Co-Zr-Al alloy systems. All of the approximate liquidus projections and vertical sections of these alloy systems were calculated by Professor Xing-Jun Liu's group in Xiamen University.

In order to fabricate bulk metallic glass composites, two alloy systems based on CuZrAl were chosen, namely, the CuZrAl-V and CuZrAl-Co systems. In considering both effects of glass forming ability and liquid phase separation, special composition ranges were selected for this study, as marked by solid frames in Figures 3.2(a) and (b). According to the simulated vertical sections as shown in Figures 3.2(a) and (b), there could be miscibility gap in the liquid state, containing two liquid phases L1 and L2. Our original goal was to cast a BMG with two glass phases. However, the V- or Co-rich liquid phase does not inherit with high glass forming ability, thus the V- or Co-rich region was found to be crystalline, imbedding in the CuZrAl-rich amorphous matrix and forming BMGCs. This allows us to examine and compare the mechanical response of these two BMGCs with different second phase shapes and morphologies.

For the CuZrAl-V system, we fail to cast amorphous alloys within the two-liquid miscibility gap region (viscosity is too high with much higher V contents). Therefore the alloys with V contents from 0 to 10 at% were prepared. For the Co-containing alloys, the cast alloys are still within the two-liquid miscibility gap region. For the CuZrAl-V and CuZrAl-Co alloys under current investigation, V- or Co-rich second phases would precipitate out from the amorphous matrix, forming BMGCs upon solidification.

3.3 Sample preparations

The cylindrical rods of the Cu-based BMG were fabricated using a conventional copper mold casting method after homogeneous melting in a purified argon atmosphere with Ti-gettered purification. This method is generally recognized as one of the most convenient way to prepare BMGs. The detailed experiments are described below.

3.3.1 Arc melting

Before the next suction casting process, arc melting is first performed to prepare the preliminary Cu-based ingots under a purified argon atmosphere for the purpose of melting the component elements uniformly. A schematic diagram for the furnace is illustrated in Figure 3.3.

Before the arc melting process, raw materials were taken appropriate amounts and placed on a copper mold. To avoid elements with a higher melting point melting heterogeneously during arc melting, the elements with a lower melting point should be placed on the bottom of copper mold and the elements with a highest melting point were put on the top of copper mold, which is close to the neighborhood of negative electrode of tungsten. This step can prevent the un-melted elements from being covered in the ingot, so as to make the composition homogeneity of the ingot.

On the other hands, to avoid the ingot oxidizing, the high-purity argon gas needs to be purged into the arc-melting furnace to flush oxygen away and, then, to turn on the vacuum pump to achieve a high vacuum atmosphere environment without impurities inside the arc-melting furnace. It is necessary to repeat this process at least four times to ensure high vacuum inside the arc-melting furnace. After these procedures, the inner environment of arc-melting furnace must be refilled with high purity argon gas of 0.15 bar.

Finally, a high voltage was added between two electrodes, and hence the arc was formed with extensive heat and bright light. The elements could be mixed together and formed the preliminary ingots under a Ti-gettered argon atmosphere. To enable the melt to be rapidly quenched and to increase the heat exchange rate, cold water was required to flow throughout the bottom of copper mold in the cooling system. Besides, the arc melting process must be repeated at least three times to confirm the elements were mixed homogeneously in the ingot.

3.3.2 Suction casting

Suction-cast rods measuring 2 mm in diameter, with the compositions $(Cu_{47.5}Zr_{47.5}Al_5)_{100-x}V/Co_x$ (x = 0, 1, 3, 5, and 10) (in at%), were fabricated using the BÜHLER Mini Arc Melting System MAM-1, as shown in Figure 3.4. After a short period homogenization about 2 s by arc melting at about 2500 K, the melt was immediately in-situ sucked into a water-cooled copper mold with internal cylindrical-shaped cavities to fabricate the Cu-based alloy rods under a purified argon atmosphere. The various copper molds with the cylindrical-shaped cavities inside could be replaced to fabricate the cylindrical alloy rods with various sample sizes in diameter. The illustration of the suction casting process is illustrated in Figure 3.3.

3.3.3 Suction casting with different inlet edged molds

In order to clarify the second-phase size effect, resulting from two cast furnaces, on the mechanical plasticity, two samples of the same composition but with different second-phase sizes were prepared. Figure 3.5 shows these two suction cast furnaces with different inlet edges from the tank to the pipe and different area-reduction rates. The ingots were initially prepared at the tank by arc melting under a purified argon atmosphere. After a short period homogenization about 2 s by arc melting at about 2500 K, the melt was in-situ sucked into a cylindrical-shaped cavities Cu mold cooled by water. Figure 3.5(a) presents the furnace with sharp inlet edged mold (termed as the S mold) with fast area-reduction rate, inducting the special vena contraction fluid mechanism [177, 178], which is due to the sudden change in diameter across the inlet, as shown in Fig. 3.5(c). Due to the sharp inlet edge, the fluid streamlines cannot closely follow the sharp angle in the mold wall and thus the converging streamlines follow a smooth path leading to the narrowing of the flow. Therefore, flow separation is occurred and the recirculating separation zones is created at the entrance of the narrower pipe, called the vena contraction. The vena contraction will lead several effects on flow instability to minimize the second phase size. In comparison, the vena contraction will not occur in the furnace equipped with the mold with blunt inlet edge and gradual area reduction (termed as the B mold) shown in Fig. 3.5(b). The fluid behavior difference is thought to impose impact on the resulting second-phase size.

Two alloys are adopted in this study, $Cu_{47.5}Zr_{47.5}Al_5$ and $Cu_{47.5}Zr_{48}Al_4Co_{0.5}$ (at%), in comparison with the previous reports [29, 30, 32, 41]. To form more B2 phases easily and to enlarge the size difference, Co needs to be added, namely, applying the $Cu_{47.5}Zr_{48}Al_4Co_{0.5}$ [33, 34]. Since there are several 100 μm spherical regions with numerous B2 particles in this alloy, liquid separation must have happened at high temperatures, the co-containing alloys are more suitable to examine the influence of fluid behaviors with different inlet edges from the tank to the pipe and different area-reduction rates during casting on the second phase particle size. For the mechanical response, both alloys were examined.

3.4 Identifications of amorphous nature

3.4.1 X-ray diffraction analyses

The amorphous nature of all as-cast cylindrical alloy rods fabricated by the conventional copper mold casting methods was first examined by X-ray diffraction (XRD) using the SIEMENS D5000 X-ray Diffractometer with Cu K_α radiation (λ = 1.5406 Å) in this study. A graphite monochrometer with 0.02 mm was used. The operating current and voltage are 30 mA and 40 kV, respectively. The range of diffraction angle (2θ) is within 20^o to 80^o at a scanning rate of 0.1^o per four seconds.

To confirm the fully amorphous state of the as-cast rod without the outer oxidative layers of sample surfaces, the as-cast rod was cut to expose the center cross-sectional surface and the cross-sectional surface of samples were ground by silicon carbide abrasive papers with water and completely polished before XRD examination.

3.4.2 Thermal analyses

The thermal properties of samples were analyzed using the applied instruments, SETARAM DSC 131 differential scanning calorimeter (DSC), with a constant heating rate of

0.33 K/s (or 20 K/min). For a non-isothermal heating course, GFA parameters associated with the glass transition temperature (T_g), crystallization temperature (T_x), supercooled liquid region ($\Delta T_x = T_x - T_g$) can be obtained in the resulting DSC curve.

3.4.3 Qualitative and quantitative analyses

After complete grinding and polishing, the cross-section surface of the samples were examined by the JEOL JSM-6330 scanning electron microscopy (SEM) with energy dispersive X-ray spectrometer (EDS) to examine the quality and quantity of designed compositions to identify the component elements and composition percentage.

3.5 Mechanical tests

3.5.1 Sample preparation

Before mechanical testing, the test samples were first sliced from the as-cast cylindrical rods using a Buehler diamond cutter. The two ends and cylindrical surfaces of the cut samples were ground by silicon carbide abrasive papers with water and then polished completely. To confirm that the test sample would be ground with an ideally perpendicular alignment between the compression surface and cylindrical axis, the top and bottom cross-sectional surfaces were carefully ground and polished by a custom sample jig. The jig was not only used to ensure parallelism between two ends of cut sample, but also to confirm that the two ends are exactly perpendicular to the longitudinal axis of sample.

If the test sample is ground and polished by hand (without the jig), it is possible to produce a slight misalignment between the compression surface and the cylindrical axis. For example, there is a geometrical defect since some samples produced by this way showed tilts of ~1° or slightly more. Wu et al. [140] has reported the information related to this subject. Therefore, it is seriously required during the sample preparation required for the subsequent compression tests.

3.5.2 Compression test

Room-temperature compression tests were performed on the cylindrical glassy rods with 2 mm in diameter at an initial strain rate of 1 x 10^{-4} s^{-1} by the Instron 5582 universal testing machine. The height-to-diameter ratio (h/d) ~2 for the test sample, providing a nominal aspect ratio of 2:1, as recommended by ASTM E9-89a (2000) for testing high strength materials. In addition, the test samples were sandwiched between two WC bearing blocks under the crossheads of the Instron testing machine. The black MOLY (molybdenum disulfide, zinc oxide in special high quality grease) was used as lubricant to decrease the friction between the test samples and WC platens. The test sample was centered carefully on the loading axis to ensure the uniaxial loading. The applied strain can be calculated according to the crosshead displacement after correction for machine compliance. To confirm the reliability of mechanical properties, multiple compression tests were performed. According to the stress-strain curve, the compressive strength, observed elastic modulus, plastic strain, and elongation can be determined. To accurately measure the change of sample displacement during deformation, the Instron 5582 universal testing machine was equipped with the Instrton 2601 Linear Variable Differential Transformer (LVDT) displacement transducer, and Figure 3.6 shows the Instron 5582 universal testing machine with the LVDT displacement transducer.

3.6 SEM observations

To observe the morphologies of fracture surfaces and side view for deformed samples, the sample was examined by the secondary electron image (SEI) and backscattered electron image (BEI) to observe the microstructure using the JEOL JSM-6330 scanning electron microscopy (SEM), operated at 10 kV.

3.7 TEM observations

A Tecnai Field-Emission transmission electron microscopy (TEM), operated at 200 kV, was used to characterize the microstructures and the composition of precipitates and phases. TEM foil samples were prepared by focus ion beam (FIB) milling. The volume fraction of the B2 particles was measured by [179]

$$f = \left(\frac{-4\pi r}{2\pi r + 8t}\right)\ln(1 - A), \tag{3.1}$$

where r is the average diameters of the B2 particle, t is the TEM foil thickness (~50 nm), and A is the projected area fraction of the particles.

Chapter 4 Results

4.1 Sample observations

The Cu-based alloys can be successfully prepared by the conventional copper mold casting method. The appearance of the as-cast $Cu_{50}Zr_{43}Al_7$ cylindrical rod and the copper molds are shown in Figure 4.1. The size of the as-cast cylindrical rods is 2 mm in diameter and ~30 mm in length. All as-cast cylindrical rods show lustrous appearances and smooth surfaces, indicating that complete filling into the mold cavities was achieved during suction casting. The surface of the $Cu_{50}Zr_{43}Al_7$ and $(Cu_{47.5}Zr_{47.5}Al_5)_{100-x}V/Co_x$ (x = 0, 1, 3, 5, and 10) rods is glossy and shiny, which is identical to the characteristic that the general metallic glasses always have. The cut samples reveal no observable macro-defect over the entire sample for the cross-sectional view cut from the as-cast cylindrical rods.

4.2 Monolithic bulk metallic glasses

4.2.1 XRD and SEM/EDS analyses

The composition and amorphous nature of the cast $Cu_{50}Zr_{43}Al_7$ base alloys were first examined by SEM/EDS and XRD. All the compositions of the as-cast rods are close to the designed composition based on the SEM/EDS characterization. The XRD pattern of the cross-sectional surface cut from the 2 mm as-cast rods consists of a board diffraction peak characteristic of the amorphous structure without distinct crystalline peaks, as shown in Figure 4.2.

4.2.2 Mechanical properties

The representative engineering stress-strain curve obtained from the $Cu_{50}Zr_{43}Al_7$ BMG compressed at a low strain rate of 1 x 10^{-4} s^{-1} is shown in Figure 4.3. The yield stress is ~1.9 GPa with an elastic modulus of ~90 GPa and elastic strain of ~2%, as well as the compressive failure strain of ~3%, as generally reported for the Cu-Zr-Al BMGs. Macroscopically, the strain-strain curve is noted to exhibit numerous flow serrations in the plastic region, as indicated in Figure 4.3. Each flow serration is characterized by load drop and load rise. However, the first detectable serration occurs at a stress level ~0.8 of yielding stress (~1.5 GPa), well before the macroscopic yielding. It was noticed that the first onset of yielding in the metallic glassy micropillar samples (1-4 μm in diameter) is over 2-3 GPa [135, 136]. The serrations in the μm-sized pillars in a recipient plasticity stage have been demonstrated to be caused by the emission of uncorrelated tiny shear bands [180]. As compared with the corresponding μm-sized BMG pillar samples, the premature yielding in the current mm-sized BMG sample appears to be associated with the fact that a relatively higher population of structure flaws, such as casting pores, unmelted particles and oxides.

4.2.3 Fracture surface observations

The side and fracture surface morphologies of tested samples were characterized after compression by SEM. Figure 4.4 shows that the tested samples fractured along a plane inclined approximately 42^{o} with respect to the loading axis, consistent with the yielding mechanism proposed by Zhang et al. [11, 97, 116, 181]. Several shear bands are observed on the side view of sample surface. Figure 4.5 shows the vein-like patterns observed all over the fracture surface. As proposed by Spaepen [182], the vein-like patterns can imply the evidence for a direction of shear band propagation along one shear plane. Some intermittent shear regions with regularly spaced striations are also observed on the fracture surface, as indicated in Figure 4.6, suggesting that shear band consecutively propagates along the principal shear plane. It is found that there are resolidified-like droplets along with nearby vein-like patterns on the fracture surface, as shown in Figure 4.7.

In Figure 4.5, the average spacing between regularly spaced striations caused by shear events is measured to be 2.6 μm (scattering from 1.8 μm to 4.5 μm). Note that the shear plane has been tilted into the horizontal plane for SEM observation. It is consistent with our general sense that the spacing between two striations observed on the fracture surface is close to the order of a few micrometers. Moreover, the average shear offset on the shear plane for one serration in the load-displacement curve (Figure 4.3) is estimated to be 1.7 μm (scattering from 0.8 μm to 4.7 μm). As reported in literatures, the amplitude of serration increases with increasing deformation strain. Note that the current serration spacing values of ~1.7 μm have been transformed into the shear offset on the shear plane, which is in a similar range as the spacing between two striations (~2.6 μm).

The above result demonstrates that there is a correspondence between the major flow serrations observed in the stress-strain curve and the regularly spaced striations on the fracture surface, suggesting that major flow serrations are a result of consecutive shear band propagation on previously existing shear bands.

4.3 BMGCs with micro-sized second phases

To clarify the different issues of BMGCs, the experimental results of BMGCs are divided into three parts according to the different research purposes, which are: BMGCs with micro-sized second phases (when V or Co contents are 3 at% or higher, as presented in this Sec. 4.3), BMGCs with nano-sized second phases (when V contents are lower than 3 at%, as presented in Sec. 4.4), and BMGCs cast by two different molds (with different melt flow natures, as presented in Sec. 4.5).

4.3.1 Microstructure analyses

Figure 4.8 shows the XRD patterns obtained from various as-cast 2 mm $(Cu_{47.5}Zr_{47.5}Al_5)_{100-x}V_x$ and $(Cu_{47.5}Zr_{47.5}Al_5)_{100-x}Co_x$ (x = 0, 3, 5, and 10) (in at%) samples. The single broad diffuse hump is evident for the $Cu_{47.5}Zr_{47.5}Al_5$ sample, characteristic of amorphous structure. There is no apparent crystalline peak in this base amorphous alloy. By contrast, the XRD patterns show numerous crystalline peaks above the broad-like diffraction hump/peaks in the CuZrAl-V and CuZrAl-Co alloys, with V or Co contents of 3% or above. The $(Cu_{47.5}Zr_{47.5}Al_5)_{97}V_3$ and $(Cu_{47.5}Zr_{47.5}Al_5)_{95}V_5$ samples show the presence of pure V (body-centered cubic), $Al_{23}V_4$ (hexagonal close-packed), CuZu (ordered cubic) and CuZr (monoclinic) crystalline peaks. And $(Cu_{47.5}Zr_{47.5}Al_5)_{90}V_{10}$ shows the presence of pure V, $Al_{23}V_4$ and CuZr. To ensure these samples were not completely crystallized, DSC scans were subsequently conducted, as shown in Figure 4.9. The results reveal the existence of glass transition (T_g) at ~695 K and crystallization (T_x) temperatures at ~740 K in these samples, with a supercooled liquid region, ΔT_x, about 45 K. No apparent variation of T_g, T_x and ΔT_x with the V content was observed, suggesting these high-V containing alloys are composites consisting of V and $Al_{23}V_4$ particles dispersed in an amorphous matrix. In parallel, $(Cu_{47.5}Zr_{47.5}Al_5)_{97}Co_3$, $(Cu_{47.5}Zr_{47.5}Al_5)_{95}Co_5$ and $(Cu_{47.5}Zr_{47.5}Al_5)_{90}Co_{10}$ show the presence of

Co_2Zr (cubic) and $CuZr_2$ (tetragonal), and CuZr crystalline peaks.

The backscattered electron image (BEI) SEM micrographs of $(Cu_{47.5}Zr_{47.5}Al_5)_{97}V_3$, $(Cu_{47.5}Zr_{47.5}Al_5)_{95}Co_3$, $(Cu_{47.5}Zr_{47.5}Al_5)_{90}V_{10}$, and $(Cu_{47.5}Zr_{47.5}Al_5)_{90}Co_{10}$ are shown in Figures 4.10-4.13. All of these micrographs show obvious phase contrast indicative of the presence of crystalline phases in the glassy matrix. There exist chemical differences between the darker and brighter regions according to the EDS results, as two examples presented in Table 4.1.

In Figures 4.10 and 4.12, the darker dendritic phases, formed during rapid cooling, are indexed to be the precipitated V and V_4Al_{23} phases, and the brighter matrix is CuZrAl amorphous phase with dispersed minor CuZr (cubic) and CuZr (monoclinic) nano particles. As shown in these images, the morphology of these precipitated phases is quite sharp, especially for those dendrite arm tip. The volume fraction of the precipitated phase (V plus V_4Al_{23}) increased obviously with increasing V content, as listed in Table 4.2.

In comparison, the second phase morphology in the Co-containing alloys is more rounded and the tip appears to be smoother, as shown in Figures 4.11 and 4.13. According to XRD and SEM/EDS (Table 4.1) results, the brighter region is mostly the Co-rich phases (brighter as a result of much lower Al content not owing to the high Co content), and the darker region is the Cu-Zr-Al amorphous matrix with dispersed CuZr (cubic) nano particles. In brighter region, there are the spherical Co_2Zr (face-centered cubic) particles containing some minor $CuZr_2$ (tetragonal) phase. We have noted that the dispersion of such particles are not uniform, being more near the rod surface. Figures 4.11 and 4.13 represent the areas with a higher particle density. The volume fraction of the compound precipitated phase (Co_2Zr plus $CuZr_2$) increased with increasing Co content based on quantitative measurement from the

SEM/BEI micrographs, as listed in Table 4.2.

4.3.2 Mechanical properties

Room temperature uniaxial compression tests of the as-cast $(Cu_{47.5}Zr_{47.5}Al_5)_{100-x}V/Co_x$ (x = 0, 3, 5 and 10) BMGC rods specimens were conducted, with a specimen aspect ratio of ~2 (2 mm in diameter and 4 mm in length). Each alloy was tested for 3-5 times, and the representative engineering stress-strain curves are shown in Figure 4.14 and 4.15. These stress-strain curves are shifted horizontally for easy observation. The mechanical properties are also summarized in Table 4.2.

First, the base BMG $Cu_{47.5}Zr_{47.5}Al_5$ exhibits the yield strength of 1.8 GPa and fracture strain of 4.5%. The V-containing $(Cu_{47.5}Zr_{47.5}Al_5)_{97}V_3$, $(Cu_{47.5}Zr_{47.5}Al_5)_{95}V_5$ and $(Cu_{47.5}Zr_{47.5}Al_5)_{90}V_{10}$ composite samples tend to fragment into several pieces by a catastrophic fracture before or upon yielding and exhibit no obvious plastic deformation. The compressive fracture strength for $(Cu_{47.5}Zr_{47.5}Al_5)_{97}V_3$ is ~1.9 GPa with a fracture strain of 2.0%. For $(Cu_{47.5}Zr_{47.5}Al_5)_{95}V_5$ and $(Cu_{47.5}Zr_{47.5}Al_5)_{90}V_{10}$, the compressive fracture strengths decrease to ~1.3 and ~1.1 GPa with reduced fracture strains of 1.4% and 1.3%, respectively. In contrast, the Co-containing BMGCs exhibited notable compressive plasticity. The average fracture strains are 8.2%, 3.6%, and 3.4% for $(Cu_{47.5}Zr_{47.5}Al_5)_{97}Co_3$, $(Cu_{47.5}Zr_{47.5}Al_5)_{95}Co_5$, and $(Cu_{47.5}Zr_{47.5}Al_5)_{90}Co_{10}$, respectively. The average compressive yield strengths are 2.0, 1.9 and 1.5 GPa for the 3 at%, 5 at%, and 10 at% Co alloys, respectively.

The different plasticity behaviors in the V or Co containing BMGCs, with V/Co contents of 3% or above inherent with micro-sized second phases, are found to be related to the second phase shape, as discussed in Sec. 5.2.

4.4 BMGCs with nano-sized second phases

4.4.1 Microstructure analyses

When the V content is lower than 3 at%, e.g., 1 at%, the second phase appears in the nano-scale. X-ray diffraction (XRD) patterns obtained from various as-cast $Cu_{47.5}Zr_{47.5}Al_5$ and $(Cu_{47.5}Zr_{47.5}Al_5)_{99}V_1$ (in at%) samples are presented in Figure 4.16. The patterns from $Cu_{47.5}Zr_{47.5}Al_5$ and $(Cu_{47.5}Zr_{47.5}Al_5)_{99}V_1$ samples are noted to consist of a single broad diffraction peak, indicating the amorphous structure. The broad diffuse hump locates between 35^o to 45^o and there is no apparent crystalline peak.

SEM micrographs (backscattered electron image, BEI) of the as-cast $Cu_{47.5}Zr_{47.5}Al_5$ and $(Cu_{47.5}Zr_{47.5}Al_5)_{99}V_1$ samples are shown in Figures 4.17 and 4.18, respectively. These micrographs are essentially featureless, without any phase contrast, indicating a homogeneous microstructure without any appreciable micro-sized second phase that can be resolved by the SEM resolution.

Microstructures of samples were then examined using bright-field and high-resolution TEM. In the as-cast samples, no phase contrast is discernible in the TEM micrographs taken from $Cu_{47.5}Zr_{47.5}Al_5$, but some B2-CuZr particles measuring about 3-5 nm in size were observed in $(Cu_{47.5}Zr_{47.5}Al_5)_{99}V_1$. After deformation, few B2-CuZr phases with crystalline lattice fringes (4–6 nm in size) become apparent in $Cu_{47.5}Zr_{47.5}Al_5$ at high magnifications, as shown in Figure 4.19. More B2 precipitates were seen in the deformed $(Cu_{47.5}Zr_{47.5}Al_5)_{99}V_1$

specimens, measuring slightly larger to 8-11 nm (Figure 4.20. Note that such B2 particles are much finer than those observed previously [29, 33]. The volume fractions of the fine B2 phase were also measured using Eqn. (3.1), and the data are included in Table 4.3.

To demonstrate the effect of V on the phase separation, TMA was conducted to measure the viscosity of $Cu_{47.5}Zr_{47.5}Al_5$ and $(Cu_{47.5}Zr_{47.5}Al_5)_{99}V_1$ as a function of temperature and the results are given in Figure 4.21. It is noted that, in the supercooled liquid region, $(Cu_{47.5}Zr_{47.5}Al_5)_{99}V_1$ BMG sample exhibits a minimum viscosity (η_{min}) of ~6 x10^9 Pa.s, which is higher than ~2 x10^9 Pa.s for $Cu_{47.5}Zr_{47.5}Al_5$. It is a three-fold increase in viscosity by adding 1 at% V into the $Cu_{47.5}Zr_{47.5}Al_5$. This increase is consistent with the notion that a composite (nanocrystals dispersed in a glass matrix) is usually more viscous than its monolithic counterpart. Thus, the TMA result supports the idea that the addition of V to $Cu_{47.5}Zr_{47.5}Al_5$ causes phase separation.

4.4.2 Mechanical properties

Uniaxial compression tests were conducted on the as-cast $Cu_{47.5}Zr_{47.5}Al_5$ and $(Cu_{47.5}Zr_{47.5}Al_5)_{99}V_1$ samples at room temperature. Representative engineering stress-strain curves for these samples are shown in Figure 4.22 and the mechanical properties are summarized in Table 4.4. For easy observation, the curve of $(Cu_{47.5}Zr_{47.5}Al_5)_{99}V_1$ sample is shifted relatively to the right by 0.01 strain. $Cu_{47.5}Zr_{47.5}Al_5$ and $(Cu_{47.5}Zr_{47.5}Al_5)_{99}V_1$ alloys exhibit notable compressive plasticity and, specifically, the fracture strains are 4.7 and 9.4%, respectively. Both alloys have the yield strength of about 1.8 GPa.

The plastic region in the stress-strain curves of $Cu_{47.5}Zr_{47.5}Al_5$ and $(Cu_{47.5}Zr_{47.5}Al_5)_{99}V_1$

is serrated, similar to other metallic glasses exhibiting compressive strain, and each serration corresponds to the propagation of one shear band [12, 183]. The total numbers of serration to failure are counted to be 113 and 259 for $Cu_{47.5}Zr_{47.5}Al_5$ and $(Cu_{47.5}Zr_{47.5}Al_5)_{99}V_1$, who fracture at 4.7 and 9.4%, respectively. There is no obvious difference in the number of shear bands per unit strain (~35 shear bands per 1% strain) in these two samples. Special effort was also made to estimate the amplitude of stress serrations in Figure 4.22. The serration amplitude was 0.0126 GPa in $Cu_{47.5}Zr_{47.5}Al_5$ and only slightly higher (0.0159 GPa) in $(Cu_{47.5}Zr_{47.5}Al_5)_{99}V_1$; the average stress serrations are also similar. It is pointed out that the first discernible strain burst (marked on the curves in Figure 4.22) is associated with shear band formation. It occurs at 1.47 GPa in $Cu_{47.5}Zr_{47.5}Al_5$ and at a slightly lower value of 1.35 GPa in $(Cu_{47.5}Zr_{47.5}Al_5)_{99}V_1$. These stresses correspond to 0.78 and 0.73σ_y, where σ_y is the "macroscopic" yield strength of the alloy, i.e. the stress plateau in the plastic region. The ratios are in good agreement with that reported in other BMG alloys (~ 0.79σ_y) [184-186].

The role of vanadium on plasticity improvement was discussed in the frame of shear band multiplication, energy dissipation during shear banding, twinning/phase transformation of the B2-CuZr particles during deformation, and deformation induced B2-CuZr particle coarsening, as discussed in Sec. 5.3.

4.5 BMGCs cast by two different molds

4.5.1 Microstructure analyses

Figure 4.23 shows the XRD patterns obtained from the as-cast (AC) $Cu_{47.5}Zr_{47.5}Al_5$ (simplified as CZA in this figure) and $Cu_{47.5}Zr_{48}Al_4Co_{0.5}$ (simplified as CZA-Co in this figure) samples cast by using two different mold inlets, i.e., the sharp S and blunt B molds. The broad diffuse hump is evident of the amorphous structure, except for $Cu_{47.5}Zr_{48}Al_4Co_{0.5}$ cast by the B mold, where the peaks associated with the ordered BCC CuZr B2 phase are seen.

Also shown in Figure 4.23 include the XRD patterns of the deformed (DF) samples. Since the XRD patterns of the AC and DF $Cu_{47.5}Zr_{47.5}Al_5$ alloys, using the S or B mold, are all the same; the DF patterns for $Cu_{47.5}Zr_{47.5}Al_5$ are not shown. But the XRD patterns for the DF $Cu_{47.5}Zr_{48}Al_4Co_{0.5}$ samples, using both the S and B molds, reveal extra peaks from the martensitic B19' phase, with some peaks associated with the retained B2 phase.

The cast microstructures were also examined by SEM, under the backscattered electron image (BEI) mode, as compiled in Figure 4.24 and 4.25. Since the CuZr B2 particles precipitated out in the $Cu_{47.5}Zr_{47.5}Al_5$ alloy cast by the S and B molds are both very fine and minor (Table 4.5), the BEI images are basically featureless under SEM at low magnifications, the same is for the $Cu_{47.5}Zr_{48}Al_4Co_{0.5}$ alloy cast by the S mold, as shown in Figure 4.24. The result shows that there is no micro-scaled crystalline phase in the former three samples. By distinct contrast, there is huge gray region, containing numerous fine particles, in the $Cu_{47.5}Zr_{48}Al_4Co_{0.5}$ alloy cast by the B mold as shown in Figure 4.25. The shape and dispersion of such gray regions change at different inlet locations, being larger and near-rectangle-shaped at the entrance from 3 mm pipe into 2 mm pipe, and near-spherical-shaped and smaller in the 2 mm pipe, as shown in Figure 4.25.

Systematic high resolution TEM characterizations on the as-cast $Cu_{47.5}Zr_{47.5}Al_5$ and $Cu_{47.5}Zr_{48}Al_4Co_{0.5}$ alloys, using either the S or B mold, reveal that there are some fine particles, indexed to be the B2 CuZr phase [42]. The measured average size and the approximate volume fraction are listed in Table 4.5. Upon plastic deformation, the B2 phase is mostly transformed to the B19' martensitic phase, based on detailed analyses from multiple selected area diffraction (SAD) patterns, as shown in Figure 4.26. Note that there are twins embedded inside some martensitic particles, as an example demonstrated in Figure 4.26.

4.5.2 Mechanical properties

The room temperature uniaxial compression tests were conducted on $Cu_{47.5}Zr_{47.5}Al_5$ and $Cu_{47.5}Zr_{48}Al_4Co_{0.5}$ cast by the S and B molds. Each alloy was tested for 3-5 times, and the representative engineering stress-strain curves are shown in Figure 4.27, and the average mechanical data are summarized in Table 4.5. For easy observation, each stress-strain curve in Figure 4.27 is shifted horizontally. Appreciable plasticity can be observed, especially for the Co-containing alloys (>20%). Overall, the plasticity for the samples cast by the B mold appears to be higher. The $Cu_{47.5}Zr_{48}Al_4Co_{0.5}$ alloys cast by the B mold even exhibit slight work hardening behavior, as shown in curve d and the insert in Figure 4.27. In many previous studies, BMGs or BMG composites showing work hardening during deformation would greatly improve the deformation instability and result in notable tensile plasticity, as discussed by, for example, Wu et al. [33, 34]. The samples prepared by the blunt inlet and gradual area reduction B mold do exhibit more ductile behavior.

An analytic model, based on melt flow dynamics with or without vena contraction, is settled, and the agreement between experiment and model is satisfactory. The effect of the mold inlet edge on microstructure and mechanical properties of cast sample was discussed in Sec. 5.4. Furthermore, the effects of B2 size on martensitic/twinning transformation and mechanical plasticity was discussed in Sec. 5.5.

Chapter 5　Discussion

5.1　Flow serrations of monolithic BMGs from energy release perspective

We noticed that vein-like patterns were only observed on the fracture surface and the sheared surface obtained from the deformed BMG samples without failure only shows intermittent shear region, which is consistent with the results of Song et al. [12], who observed regularly spaced striations on the sheared surface. Compared with the brittle Mg-based and the current more ductile Cu-based BMGs, Mg-based BMGs tend to fragment into several pieces by a catastrophic fracture before or upon yielding and fracture surface mainly consists of the cleavage structures [95, 128]. The fracture morphologies of the current $Cu_{50}Zr_{43}Al_7$ BMG present a slightly more ductile fracture characteristic with the coexistence of vein-like patterns and intermittent shear region on the fracture surface.

Since flow serration is a result of macro and major shear band propagation [184, 187], the energy release during shear band propagation or at failure can be roughly estimated based on the accumulated area under one serration in the stress-displacement curve. Note that the minor serration caused by the concurrent multiple shear-band emission is not of the major concern of this paper; only the major serrations caused by the propagation of the principal shear-band is analyzed here. As represented by the inserted triangles in Figure 5.1, the energy release ($\mathit{\Delta} E$) can be expressed as

$$\mathit{\Delta} E = \tau_y \Delta u_s \cong \sigma_y \Delta u_s / 2 \ , \tag{5.1}$$

where τ_y is the shear yield stress, $\mathit{\Delta} u_s$ is the shear offset and σ_y is the yield stress. Note that the shear offset on the shear plane inclined ~42° with respect to the loading axis can be converted by the axial displacement. Based on the Eqn. (5.1), the average energy release in the serrated region is estimated to be ~$1.8\text{x}10^3$ J/m^2 for the current $Cu_{50}Zr_{43}Al_7$ BMG. Note that this average value is taken from several serrations in the stress-strain curve. The energy release at failure is also estimated to be ~$2.2\text{x}10^5$ J/m^2, which is noted to be about two orders of magnitude larger than those for each serration event.

This result suggests that the energy release at failure is sufficiently high to cause a temperature rise and, thus, shear band may be heated up by the high accumulated fracture energy, resulting in a local change of viscosity within a shear band, as discussed in the previous literatures [188-191].

To further clarify this issue, the temperature rises during shear band propagation and at failure are also estimated for comparison. As reported by Zhang et al. [188], the evolution of the temperature profiles after shear deformation in metallic glasses can be given by the thin-film solution of the heat equation:

$$\Delta T = \left(\frac{H}{2\rho C\sqrt{\pi\alpha}}\right)\frac{1}{\sqrt{t}}exp\left(-\frac{x^2}{4\alpha t}\right), \tag{5.2}$$

where ΔT here is the temperature rise above ambient temperature; H is the heat content of the shear band caused by one shear event; ρ, C and α are the density, specific heat capacity and thermal diffusivity of BMG, respectively; x is a half-width of hot zone from the center of shear band; and t is the elapsed time of one shear event. For the current $Cu_{50}Zr_{43}Al_7$ BMG, ρ, C, α and x are taken to be $7.1\text{x}10^3$ kg/m^3, 391 J/(kgK), $2.3\text{x}10^{-6}$ m^2/s and 0.4 μm, respectively, which are taken from the data on the $(Cu_{50}Zr_{50})_{92}Al_8$ BMG [188] with a closely similar composition to the present alloy. Recently, Song and Nieh [184] and Chen et al. [187] performed the similar compression tests using high-sensitivity strain-gauges directly attached to two opposite sides of test sample to trace flow serrations for three Zr-based [184] and Pd-based and Mg-based [187] BMGs. In their studies, the elapsed time during shear band propagation for one serration (t) lasts for ~10^{-3} s. Based on the previous studies [184, 187], t is assumed to be 10^{-3} s for the current $Cu_{50}Zr_{43}Al_7$ BMG. Here we also assume that the energy release (ΔE) for one serration or at failure is completely converted into heat (H). Taking the above parameters into the Eq. (2), the temperature rise during each serration (or the shear band intermittent propagation) and at failure can be roughly estimated to be ~7 K and ~471 K, respectively. The measured values about one shear serration event and final failure are tabulated in Table 5.1.

Taking into account of the ambient temperature of ~300 K, the resulting temperatures are ~307 K for one shear event and ~771 K at failure, respectively. In our parallel thermal analyses, the T_g of the current $Cu_{50}Zr_{43}Al_7$ BMG is 723 K. It is evident that the temperature rise during each shear band intermittent propagation is significantly low (only a few degrees Kelvin), which is consistent with the results of Han and Li [191], and the resulting temperature (307 K) is well below T_g (723 K). Therefore, local heating seems unlikely to be the primary cause of the change in viscosity during a propagating shear band. The change in viscosity appears to be associated with excess free volume generation within a shear band, which has been recently demonstrated by Song and Nieh [184].

However, at failure, the resulting temperature (~771 K) is much higher than T_g (723 K) and in the supercooled liquid region as a viscous flow state, suggesting that the resulting temperature is sufficiently high to make the viscosity within a shear band dramatically drop.

As reported by Yang et al. [189], they proposed a criterion to predict the temperature rise within a shear band. Upon a catastrophic failure, the resulting temperature theoretically predicted within a shear band is close to T_g. Even if the elapsed time upon failure is in an instant, the sudden temperature rise will become significantly large. If we exaggeratedly assume that t decreases by one order of magnitude from 10^{-3} s to 10^{-4} s and, then, ΔT will increase accordingly from 471 K to 1490 K for the current $Cu_{50}Zr_{43}Al_7$ BMG. It is noted that the resulting temperature of 1790 K is much higher than the melting temperature of ~1100 K for the present alloy, namely, local melting might occur while BMG separates along the fracture surface upon a instant failure. That is why the resolidified-like droplets with vein-like patterns are simultaneously observed on the separated surface, as shown in Figure 4.7.

For the current $Cu_{50}Zr_{43}Al_7$ BMG, the dependences of energy releases and temperature rises for one shear event and at failure as a function of shear events during plastic deformation, together with fracture morphologies, are plotted in Figure 5.2. During inhomogeneous deformation in BMG, the uncorrelated multiple shear bands form and, then a principal shear band soon develops and dominates the deformation process until failure. Afterward, the principal shear band starts to propagate along the major shear plane. Since small accumulated energy release for one shear event can quickly conduct away, it seems unlikely that the viscosity within a shear band dramatically drops, and, thus, shear band will not shear through the sample. Instead, the shear band would consecutively propagate in a small distance, which eventually leads to the intermittent shear region with regularly spaced striations on the fracture surface.

As intermittent shear events occur, the contact cross-sectional area of upper and lower sheared samples becomes smaller and smaller with increasing sliding, thus the true stress is actually higher than the engineering stress. Meanwhile, in terms of the sample geometry, the deviation from the uniaxial applied loading becomes more and more obvious with intermittent sliding. Once BMG hardly sustain the geometrical instability, BMG will be unable to accommodate shear band propagation and, thus, the principal shear band will run away with a large shear offset and lead to a catastrophic failure caused by the high accumulated fracture energy, resulting in the vein-like patterns and re-solidified-like droplets observed on the fracture surface.

This result suggests that the poor plasticity of monolithic bulk metallic glasses is due to the geometrical instability due to intermittent shear events and sudden temperature rise, which is due to high accumulated fracture energy, to cause the dramatic drop in viscosity. Once the BMG hardly sustains the geometrical instability, if there is no obstruction for shear ban propagation, the principal shear band will run away with a large shear offset and lead to a catastrophic failure. Therefore, it is hard to improve plasticity obviously by intrinsic toughening such as increasing the Poisson’s ratio or increasing the randomly distributed free volume. Thus, extrinsic toughening, such as introduced micro-sized or nano-sized particles, would be the promised way to improve the deformation stability of BMGs.

5.2 Mechanical response of micro-scaled phases in CuZrAl-V/Co BMGCs

For the CuZrAl-V alloy system, since the compositions are outside the two-liquid miscibility gap, the precipitated V-rich phases are postulated not to be formed by two-liquid phase separation in the melt. Instead, these precipitated phases are thought to be formed as a result of oversaturation of V content during rapid cooling. The melt did not separate into two liquids and the V-rich phases were precipitated during cooling due to the oversaturation of V content. Thus, the precipitate shape and tip are rather sharp, as shown in Figures 4.10 and 4.12. Moreover, since Al was attracted by V to form the V_4Al_{23} phase, Al is in depletion within the CuZrAl amorphous matrix, hence, a small amount of CuZr (cubic) and CuZr (monoclinic) phases were precipitated within the CuZrAl amorphous matrix. The effect from the minor B2 CuZr phase will be presented in a separate paper. Here we only address the effect of the V- or Co-rich phases on the mechanical response.

In comparison, the brighter domain is the Co-rich phases and the darker matrix is the amorphous matrix in the CuZrAl-Co alloy system, as shown in Figures 4.11 and 4.13. According to the EDS results, as shown in Table 4.1, there exist chemical differences between darker and brighter regions, especially for the Cu and Co contents. Different from the V-containing alloys, the precipitated Co-rich phases appear to have been formed during high-temperature induction melting within the two-liquid phase equilibrium as shown in Figure 1.2(b), as a result of the positive heat of mixing between Cu and Co. Since Co-Zr has the most negative heat of mixing, -23 kJ/mol as shown in Table 1.2, CoZr-rich domain would form in the liquid state. The rest contents formed the CuZrAl-rich domain. During cooling from the liquid state, the two domains with different glass forming ability partition individually in the solidified phases. Based on the XRD, SEM/EDS and TEM results, it is concluded that the brighter region in $(Cu_{47.5}Zr_{47.5}Al_5)_{95}Co_5$ and $(Cu_{47.5}Zr_{47.5}Al_5)_{90}Co_{10}$ are the mixture of dominant crystalline Co_2Zr (face-centered cubic) plus minor $CuZr_2$ (tetragonal) particles. This is because that the CoZr-rich composition has poor glass forming ability. The CuZrAl region transform into amorphous matrix due to high glass forming ability.

Due to the difference of the morphology and tip shape of precipitated phases in the V- and Co-containing alloy systems, there exists a difference in stress concentration of these two alloy systems under deformation. Considering the tip of those brittle precipitated phase as a notch-tip inside the specimen, the concentrated stress at the tip of precipitated phase can be assessed using the linear elastic fracture mechanics [192]. The variation of the normal stress on the plane of the notch, σ_t, under applied stress, σ_0, with a root-radius ρ and a distance ahead of the notch-tip a (Figure 5.3(a)) is given by:

$$\sigma_t = \sigma_0 \, [1 + 2 \, (a/\rho)^{1/2}]. \tag{5.3}$$

Considering the long axis of the precipitated phase is not always perpendicular to loading direction. The factor F_θ is introduced into this equation [192]:

$$\sigma_t = \sigma_0 \, [1 + 2 \, (a/\rho)^{1/2}] \cdot F_\theta \, . \tag{5.4}$$

In any case, the ratio of precipitated phase length over root-radius, a/ρ, for the precipitated phase tip will dominate the degree of stress concentration.

By inserting proper data from the current measurements, we obtain the ratio of stress at the precipitated phase tip over applied stress and the angle factor, as listed in Table 4.2. Obviously, there is higher degree of stress concentration, $\sigma_t/(F_\theta \sigma_0)$, in the V-additive alloys than in the Co-additive alloys by a factor of ~3.5.

The difference of stress state in these two systems can be explained in Figure 5.3. Figures 5.3(b) and 5.3(c) compare the difference in stress concentration with sharp and rounded precipitated phase tip of the V- and Co-containing alloys. Since there is a high degree of stress concentration at the tips of V-rich sharp precipitated phase, cracks are more likely to be initiated at such sites, causing premature failure and much lower plastic deformation. Also, stress concentration sites would increase with increasing volume fraction of precipitated phases. Thus, fracture strengths and strains were seen to decrease with increasing V content.

With the lower degree of stress concentration in the Co-containing alloys with round Co-rich phases, as shown in Figure 5.3(c), the stresses are more uniformly distributed on the surface of rounded precipitations. Cracks are less likely to form. Instead, debonding could occur at the later stage of deformation. Overall, the mechanical response of the Co-containing BMGC tends to be more promising.

However, seems there are limit of plasticity improvement by introducing micro-sized second phase due to the stress concentration on the sharp interface between matrix and brittle second phase. Thus, to toughen the BMGCs, rounded tough second phases are must to be select to increasing the deformation stability via absorbing strain energy and obstructing shear band propagation.

5.3 Effects of V on phase formation and plasticity improvement

Recently, it was demonstrated that the plasticity of BMGs could be enhanced by introducing micron or nano-scale into the amorphous matrix [20-34]. For example, Pauly et al. [29-32] showed that the presence of B2-CuZr nanoparticles in a $Cu_{47.5}Zr_{47.5}Al_5$ alloy could apparently improve its tensile plasticity. The B2-CuZr nanoparticles, ~10 nm in the as-cast condition, were able to undergo twinning, phase-transformation, and coarsening (to about 50 nm) under deformation. These deformation processes could prevent from plastic instability and could dissipate energy, thereby improving the ductility. Wu et al. [33, 34] also demonstrated that a minor 0.5 at% addition of Co in the $Zr_{48}Cu_{47.5}Al_4Co_{0.5}$ alloy could further improve the tensile ductility, due to much larger spherical particles (or regions) up to 100 μm which contains ~80 nm B2-CuZr nanoparticles. In this Co-containing alloy, the strain hardening rate was enhanced and plastic instability was suppressed due to a B2-CuZr to B19'-ZrCu martensitic transformation, similar to TRIP (transformation-induced plasticity) steels.

Since vanadium has similar thermodynamic features as Co with respect to the Cu-Zr-Al system. The mixing enthalpy of the binary Cu-V (+5 kJ/mol) or Cu-Co (+10 kJ/mol) system is positive and the mixing enthalpies of the other binary systems are all negative, as shown in Table 1.2 [43]. Furthermore, minor addition of vanadium changes the crystallization mode to encourage the precipitation of Cu-Zr phase of the samples and leads to change of mechanical properties. However, glass forming ability of BMGs decreased with further increasing V content [44]. Furthermore, since the heat of mixing between the two major constituents in this system, Cu and Zr, is more negative than that between other elemental combinations, more B2-CuZr particles are expected when a small amount of V is added to displace Cu from the amorphous matrix. Hence, small amount addition of V is introducing into Cu-Zr-Al alloy system to produce BMGCs with nano-sized CuZr B2 phase.

The data presented so far indicate that the addition of 1 at% V to $Cu_{47.5}Zr_{47.5}Al_5$ improves the compressive plasticity but higher V addition degrades the plasticity. The fact that the serration density, i.e. shear band numbers per unit strain, is essentially the same in both $Cu_{47.5}Zr_{47.5}Al_5$ and $(Cu_{47.5}Zr_{47.5}Al_5)_{99}V_1$ (Figure 4.22) suggests that the observed plasticity enhancement in $(Cu_{47.5}Zr_{47.5}Al_5)_{99}V_1$ is not a result of shear-band multiplication, as often reported in BMGs with improved plasticity [16]. The amplitude of stress serration is associated with energy dissipation during shear band propagation. Our data indicate that the serration amplitude in the two alloys is comparable (0.0126 GPa vs 0.0159 GPa) suggesting that the energy dissipated during shear band propagation in the two alloys is also similar. In other words, the presence of V appears to have insignificant effect on the energy dissipation during plastic deformation.

Strain burst on a stress-strain curve is associated with shear band formation [183]. The first discernible burst is considered the very onset of yielding and is affected by the initial free volume content in a BMG alloy [193, 194]. The result that $(Cu_{47.5}Zr_{47.5}Al_5)_{99}V_1$ has a lower strength (1.35 GPa) than that of $Cu_{47.5}Zr_{47.5}Al_5$ (1.47 GPa) suggests that the 1 at% V addition might have higher free volume content. However, according to Spaepen’s constitutive equation and related deviation [193], the yield strength was found to be extremely sensitive to the free volume content. It follows that such a small change in strength is unlikely to be caused by an appreciable change in free volume. Thus, the observed improved plasticity is unlikely resulted from significant increase in free volume caused by the V addition, either.

As mentioned before, the addition of V to the $Cu_{47.5}Zr_{47.5}Al_5$ alloy could cause the melt to separate into the Cu-rich and V-rich regions during casting because a positive heat of mixing between Cu and V. To demonstrate the effect of V on the phase separation, TMA was conducted to measure the viscosity of $Cu_{47.5}Zr_{47.5}Al_5$ and $(Cu_{47.5}Zr_{47.5}Al_5)_{99}V_1$ as a function of temperature and the results are given in Figure 4.21. It is noted that, in the supercooled liquid region, $(Cu_{47.5}Zr_{47.5}Al_5)_{99}V_1$ BMG sample exhibits a minimum viscosity (η_{min}) of ~6 x 10^9 Pa.s, which is higher than ~2 x 10^9 Pa.s for $Cu_{47.5}Zr_{47.5}Al_5$. It is a three-fold increase in viscosity by adding 1 at% V into the $Cu_{47.5}Zr_{47.5}Al_5$. This increase is consistent with the notion that a composite (nanocrystals dispersed in a glass matrix) is usually more viscous than its monolithic counterpart. Thus, the TMA result supports the idea that the addition of V to $Cu_{47.5}Zr_{47.5}Al_5$ causes phase separation.

When V concentration is high (>1 at%), however, intermetallic $Al_{23}V_4$ is formed (see Figure 4.10 and 4.12). It suggests that V has a higher affinity to Al than to Cu or Zr. In other words, V and Al atoms tend to agglomerate or cluster in the glass matrix and form $Al_{23}V_4$ when the V concentration is excessive (> 1%), as indicated in Table 4.3. Intermetallic particles are usually brittle, especially when their sizes are larger than ~µm. In the current case, the dimension of $Al_{23}V_4$ is about 1-5 µm. Upon loading, $Al_{23}V_4$ is weaker than the strong amorphous matrix, thus fractures first whilst the amorphous matrix is still in the elastic range. At the same time, the sharp tip of the phase becomes the stress concentration site, thus, the fractured $Al_{23}V_4$ subsequently becomes shear band initiation site and exacerbates the fracture process.

When V content is low, for example, in the $(Cu_{47.5}Zr_{47.5}Al_5)_{99}V_1$ alloy, no V-containing compound could be found in the sample. Since V is practically insoluble in Al [195], Cu and Zr constituents in the alloy apparently open up the Al-V solid-solution phase field. Also, since the heat of mixing of Cu-Zr and V-Al is more negative than that of Cu-Al and V-Zr, it results in the formation of the Cu-Zr rich and V-Al rich regions, i.e. the depletion of Al from the original Cu-Zr-Al matrix. Aluminum depletion produces an amorphous matrix with a higher Cu-Zr content and, thus, thermodynamically favors the formation of B2-CuZr particles during cooling. In fact, the composition of the amorphous matrix is close to equimolar Cu-Zr.

Pauly et al. [29] pointed out that the presence of fine B2-CuZr could enhance plasticity and prevent catastrophic failure in $Cu_{47.5}Zr_{47.5}Al_5$. The B2 particles greater than about 25 nm appeared to have undergone twinning transformation. The microstructure of the current V-containing alloy was examined using TEM. Bright-field and high-resolution TEM micrographs taken from deformed $Cu_{47.5}Zr_{47.5}Al_5$ and $(Cu_{47.5}Zr_{47.5}Al_5)_{99}V_1$ are given in Figures 4.19 and 4.20, which show the dispersion of nanocrystals in the amorphous matrix. Through the determination of the lattice constant by fast Fourier transformation (FFT) filter of the ordered regions, the nanocrystals in both samples are identified to be B2 CuZr, as shown in Figures 4.19 and 4.20. No nanocrystal was discernible in the as-cast $Cu_{47.5}Zr_{47.5}Al_5$, but a slight amount of nanocrystals was observed in the deformed sample. Both the density and size of the B2 phase in the deformed $Cu_{47.5}Zr_{47.5}Al_5$ and $(Cu_{47.5}Zr_{47.5}Al_5)_{99}V_1$ are much higher than that in the as-cast specimens, as indicated in Table 4.3.

In addition, more and larger B2 nanocrystals are observed in the deformed $(Cu_{47.5}Zr_{47.5}Al_5)_{99}V_1$ sample (~7.2 vol% and ~10 nm in diameter) as compared to that in the deformed $Cu_{47.5}Zr_{47.5}Al_5$ (~1.5 vol% and ~5 nm in diameter). It is evident that deformation can induce precipitate growth in the current BMGs, consistent with the previous observation [29]. Twinning and phase transformation in B2-CuZr have been suggested to contribute to the ductility improvement in CuZrAl-based metallic glasses [29, 33]. However, in the current study, no twin formation or phase transformation of the current fine B2-particles (all less than 10 nm) was observed in the $(Cu_{47.5}Zr_{47.5}Al_5)_{99}V_1$ alloy, excluding the possibility that twinning or phase transformation has contributed to the observed plasticity enhancement. A plausible explanation might be related to the size of B2 particles. When the B2 particles are measured greater than ~25 nm, the accumulated shear stress within the B2 phase is high enough to induce twinning or even martensitic transformation. But if the B2 phase is too small, as in the range of 10 nm or less, twinning or martensitic transformation would not be able to proceed. There seems to be a critical size for the induction of twinning or martensitic transformation.

Pauly et al. [29] suggested that deformation-induced growth of B2-CuZr could dissipate energy, prevent catastrophic shear band propagation and, thus, improve plasticity. In the current $(Cu_{47.5}Zr_{47.5}Al_5)_{99}V_1$ sample, the mean size of B2 particles increases from the initial 3-5 nm to 10 nm, and the volume fraction also increases from 0.8 vol% to 7.2 vol% after deformation. However, the number of B2 particles in the sample is noted to decrease after deformation; specifically, they are 12 x 10^4 /m^3 and 8.4 x 10^4 /m^3 in samples before and after deformation. The reduction of particle number indicates that some small CuZr particles were dissolved during plastic deformation. The observation is also consistent with the fact that volume fraction of the B2 phase increases from 0.8 vol% to only 7.2 vol%; the volume fraction is evaluated to be 12.5% if all initial particles grow simultaneously. It further suggests that the nucleation of new B2 particle during deformation was negligible. In the following, we perform an analysis to elucidate the energy balance during deformation.

The initial and final energy densities of the system, as illustrated in Figure 5.4, are $n_o(4\pi r_o^3/3)G_p + n_o(4\pi r_o^2)\gamma_{p-m} + (1-f_o)G_m$ and $n_1(4\pi r_1^3/3)G_p + n_1(4\pi r_1^2)\gamma_{p-m} + (1-f_1)G_m$, where the subscripts 0 and 1 represent the initial and final states, respectively. In the expressions, G_p and G_m are the energy density of the particle and matrix, r is the average diameters of the B2 particle, n is the number density per unit volume of the B2 particles, and γ_{p-m} is the particle-matrix interface energy, and f $(=n(4\pi r^3/3))$ is the volume fractions of the B2 particle. Assuming there is no heat loss, energy balance would require the mechanical work (W) done to be

$$W = (f_1 - f_o)(G_p - G_m) + 3\gamma_{p-m}\left(\frac{f_1}{r_1} - \frac{f_o}{r_o}\right) \quad (5.5)$$

In the equation, (G_p - G_m) is essentially the crystallization energy, which is estimated to be 2.21 x 10^9 J/m^3 from previous DSC measurements [196, 197]. Substitute data from the current measurements, we obtain γ_{p-m} = 0.293 J/m^2 as the particle-matrix interface energy in the $(Cu_{47.5}Zr_{47.5}Al_5)_{99}V_1$ sample. To our best knowledge, there is no experimental datum for the crystallized particle-amorphous matrix interface energy in any metallic glass system, although it was expected to be low [198]. The only available datum is for silicon, which is about 0.4 J/m^2 [199]. In comparison, the crystalline-crystalline interface energy, for example, the θ' precipitate-aluminum interface is about 1.5 J/m^2 [200]. The current estimation of γ_{p-m} for B2-CuZr appears to be in the right range.

Since the interface energy is directly related to the coarsening, within the classical coarsening theory [201], the above reasonable extracted interface energy implies that the coarsening argument is logical. From the energy point of view, our current results appear to indirectly support the idea of Pauley et al. [29], i.e. plasticity improvement in $(Cu_{47.5}Zr_{47.5}Al_5)_{99}V_1$ is attributable to the dynamic coarsening of B2-CuZr particles, when the B2 particles are too small to induce twinning or martensitic transformation. The fine B2 particles in the current alloys appear to be unstable, and would undergo coarsening during deformation. It is expected that once the B2 particles grow larger to a level of a few tens of nanometers, twinning or martensitic transformation might be induced.

5.4 Effect of cast mold inlet orifice on plasticity of Cu-Zr-Al glassy alloys

In the previous research using the commercial mini-suction furnace [41, 42], the B2 particles are all smaller than 5 nm in the as-cast condition and there was no twining or martensitic transformation observed in the Cu-Zr-Al or Cu-Zr-Al-V alloys during deformation. In comparison, the B2 particle size in other reported papers was about 25 nm in $Cu_{47.5}Zr_{47.5}Al_5$ [29] and about 80 nm in $Cu_{47.5}Zr_{48}Al_4Co_{0.5}$ [33, 34]. The size of the B2 phase seems to impose some effects on the twining or martensitic transformation. While the composition influence via the minor addition of Co [33, 34] or V [42] have been researched, another factor that has not been thoroughly considered might be the cast condition. Thus, in the following research, two different suction cast furnaces, with different inlet orifice edges from the tank to the pipe and different area-reduction rates, were introduced to explore the B2 size effects on the mechanical plasticity. This would allow us to examine the effects of cast mold inlet orifice on the resulting microstructures and second-phase morphology, and in-turns the mechanical response.

The data presented in Sec. 4.5 indicate that the microstructures are resulted from different flow characteristics during casting by using different mold inlets. In what follows, three aspects are considered in terms of the vena contraction [177, 178], sudden flow velocity change, and Reynolds number to assess the suction cast conditions and the consequence on resulting alloy microstructures.

First, for the sharp inlet edged mold as shown in Figure 3.5(c), the tank cross-sectional area (A_1) is much larger than pipe area (A_3) so that there would be a sudden change in diameter across the inlet. Since the inlet edged is sharp so that the fluid streamlines cannot abruptly change direction when the mold diameter contracted suddenly. In such a case, the streamlines are unable to closely follow the sharp angle in the mold wall. The converging streamlines follow a smooth path, leading to the narrowing of the flow. As a result, there is flow separation, creating recirculating separation zones at the entrance of the narrower pipe. The main flow would be contracted at the separated flow areas (A_2) and later on be expanded again to cover the full pipe area (A_3), it is called the vena contraction [177, 178]. The contracted flow can be expressed by using the Borda–Carnot equation, with the coefficient of contraction μ which is defined by [177, 178]

$$\mu = \frac{A_2}{A_3} \ . \tag{5.6}$$

According to the measurements by Weisbach [178], the contraction coefficient for a sharp edged contraction can be approximately expressed as [178]:

$$\mu \ = 0.63 + 0.37\left(\frac{A_3}{A_1}\right)^3 . \tag{5.7}$$

By substituting the suction furnace with the sharp edged mold, we obtain μ = 0.63 (it is about 0.6300049), or the contracted area at the entrance of the narrower pipe A_2 is equal to $0.63A_3$. Since the fluid experiences a sharp cross-sectional area reduction from the tank into the inlet, there is a violent fluid-direction change so that the fluid would be highly unstable. Moreover, when the fluid flows into the entrance, the violent fluid-direction change would induce the flow separation so that the fluid streamlines no longer follow the mold surface. As shown in region 1 in Figure 5.5(a), if there are two miscible liquids due to liquid phase separation in the fluid, one presented in white color and one in gray color [13, 14], the diameter of the separated liquid would reduce dramatically through the inlet and vena contraction.

Secondly, due to the fluid is non-compressible and the mass of the fluid is in conservation, the velocity must change dramatically from the tank to the pipe through the sharp cross-section reduction near the inlet and especially at the vena contraction. Since the fluid is continuous, the volumetric flow rate through any cross-section A_a or A_b has to be equal, thus we have

$$A_a v_a = A_b v_b , \tag{5.8}$$

where v_a and v_b are the mean flow velocity at the cross-sections A_a and A_b, respectively. Meanwhile, the overall time for the fluid to flow through each region would equal the time for ingot shrink (t_s) in the tank. Since t_s can be easily measured, the mean flow velocity at any position in regions 1, 2 and 3 can be roughly calculated, as shown below:

$$\frac{L_1}{v_1} + \frac{L_2}{v_2} + \frac{L_3}{v_3} + \frac{L_4}{v_4} + \frac{L_5}{v_5} = t_s , \tag{5.9}$$

where L_1, L_2, L_3, L_4, and L_5 are the lengths of tank, vena contraction, pipe of 4 mm, pipe of 3 mm, and pipe of 2 mm, respectively. Meanwhile, the v_1, v_2, v_3, v_4, and v_5 are the mean flow velocity of these five regions. Note that v_2, v_3, v_4, and v_5 are all a function of v_1 following Eqn. (5.8) by inputting each cross-sectional area. Thus, v_1 can be roughly calculated by Eqn. (5.9) with corresponding v_2, v_3, v_4, and v_5. It follows that the mean flow velocity at any position in regions 1, 2 and 3, as well as the velocity change across any cross-sectional area change, can be easily calculated, as listed in Table 5.2.

As shown in Table 5.2 and Figure 5.6, the velocities of each region in the sharp mold are fast and the velocity change when the cross section reduction is significant, especially in the vena contraction region which is as high as 2107 m/s^2 in the narrow region. As a result, the inertia of the fluid flow is large when the fluid flows through the sudden reduced area. As shown for region 2 in Figure 5.5(a), the violent velocity rise and velocity change would bring huge fluid flow inertia, cutting the separated liquid block into small pieces.

For region 3 in Figure 5.5(a), the mean flow velocity is fast and thus the inertial forces of the fluid would affect the stability of the fluid flowing. However, it is hard to indicate the stability of the fluid flowing by only the mean flow velocity. To further characterize the flow turbulent degree, the Reynolds number (R_e) is introduced as given by [202, 203]:

$$R_e = \frac{vL}{\nu} , \tag{5}$$

where v is the mean flow velocity of the fluid (m/s) at any cross-section, L is a pipe diameter (m), and ν is the kinematic viscosity (m^2/s) of the melt. The Reynolds number is used to characterize different flow modes, such as laminar or turbulent flow. For low Reynolds numbers $R_e < 2300$ [203], laminar flow occurs where viscous forces are dominant, characterized by smooth and constant fluid motion. In the interval between $R_e = 2300 - 4000$, laminar and turbulent flows are both possible. It is called the transition flow, depending on other factors such as pipe roughness and flow uniformity. At high Reynolds numbers $R_e > 4000$, turbulent flow occurs, dominated by inertial forces with frequent chaotic eddies, vortices and other flow instabilities. Substitute current data plus the kinematic viscosity of $Cu_{90}Al_{10}$ at 1450°C, which is approximate 4.5×10^{-7} m^2/s [204], we can obtain the Reynolds numbers under different pipe diameters and mean flow velocities, as also listed in Table 5.2.

As shown in Table 5.2, in the tank (region 1), where the ingot was melt, for the S mold, R_e is about 916 (< 2300) and thus the laminar flow occurs. The melt which has undergone liquid phase separation at high temperatures remain two miscible liquids as large blocks, as shown for region 1 in Figure 5.5(a). When the fluid passes through the inlet into the pipe entrance (region 2), R_e increases dramatically to 7500 (> 4000) with a sudden increase of mean flow velocity. As a result, turbulent flow occurs and the chaotic eddies would force the miscible liquid into small pieces, which then flows into the pipe, as shown for region 2 in Figure 5.5(a). The velocity in region 3 is still relatively high with R_e about 5953 and thus the fluid is still unstable so that the small separated liquids would tend to decompose during the flowing, as shown in the insert for region 3 in Figure 5.5(a).

On the other hand, the B mold would lead to lower mean flow velocity, velocity change, and Reynolds numbers. The fluid becomes more stable and it is benefit to retain the separated miscible liquid, as shown in Figure 5.5(b). Since the cross-section of the tank of the B mold in our study is rectangle, the separated liquid was shaped up into a cuboid shape. With gradual cross-sectional area reduction, the size of the separated liquid was reduced but the appearance was maintained. Thus the huge rectangle-shaped CuZr-rich phase was maintained before the fluid flow into the 2 mm mold, as shown in the inset of Figure 5.5(b). The fluid is laminar flow and remains stable until the mold diameter is reduced to 2 mm where the temperature is already lower and the melt become viscous and finally solidified. Here the Reynolds number was raised to the transition range of 3483 (Table 5.2), the minor chaotic eddies and fluid flow inertia would render huge rectangle-shaped CuZr-rich phase region searated into several smaller near-spherical-shaped regions, as shown in the lower insert in Figure 5.5(b).

5.5 Effects of B2 size on martensitic/twinning transformation and mechanical plasticity

It is demonstrated above that the B2 particles in samples cast by the blunt mold would result in more and larger B2 particles, as compared with those cast by the sharp mold. And such B2 particles, greater than the threshold size (approximately in the range around 15-20 nm), would undergo martensitic transformation from the ordered BCC B2 phase into the monoclinic B19’ phase. In some of the larger transformed B19’ particles, embedded twins are also found. Such complex martensitic/twinning transformation would help in absorbing the dynamic energy from the propagating shear bands in the Cu based BMGs, preventing catastrophic single major shear-band propagation along the principal shear direction and thus improving plasticity significantly. The martensitic/twinning transformation induced plasticity (TRIP), similar to the toughening mechanisms in TRIP steel or Y-ZrO_2, is indeed very promising in BMGs.

In the Co-containing $Cu_{47.5}Zr_{48}Al_4Co_{0.5}$ alloys, this effect is particularly more pronounced. This is because that the Co with a positive heat of mixing with Cu (+10 kJ/mol [43]) would promote Cu to form more CuZr B2 partilces [41]. Thus, more B2 particles, aggregating together to form the gray region (Figure 4.25) if the blunt mold is in use, would impose a highly positive factor on the mechanical performance. The toughening mechanism would even induce work hardening in the flow stress curve, characteristic of ductile behavior in metallic materials.

Chapter 6 Conclusion

The microstructural and mechanical response of the Cu-based bulk metallic glasses (BMGs) and bulk metallic glass composites (BMGCs) are systematically researched in this thesis. It starts from the energy release of shear banding propagation in the fully amorphous base CuZrAl BMGs, followed by the characterization and analysis of the BMGCs with micro- or nano-sized second phases. Finally, the size effects of the second phases on the mechanical plasticity are examined more in details by using different cast molds.

1. During one shear event, the energy release and temperature rise are significantly low (~$1.8\text{x}10^3$ J/m^2 and ~7 K), resulting that shear band will not shear off the sample but to consecutively propagate in a small distance, which leads to the intermittent shear region on the fracture surface. However, due to high accumulated fracture energy about $2.2\text{x}10^5$ J/m^2, the sudden temperature rise about 471 K is sufficient high to cause the dramatic drop in viscosity within a shear band upon a catastrophic failure, resulting in the vein-like patterns and re-solidified droplets on the fracture surface. The result suggests that the poor plasticity of monolithic bulk metallic glasses is due to the geometrical instability due to intermittent shear events and sudden temperature rise due to high accumulated fracture energy. If there is no obstruction for shear band propagation, the principal shear band will run away with a large shear offset and lead to a catastrophic failure when the BMG is hard to sustain the geometrical instability.

2. Microstructures and mechanical response of the two alloy systems of CuZrAl-V/Co are examined and compared. Stress concentration associated with the second crystalline phase in the amorphous metallic matrix plays an important role in the deformation

mechanism in bulk metallic glass composites. In the V-containing alloys, the tips of dendritic precipitate V-rich phases (formed during rapid cooling) are quite sharp. Stress can be easily concentrated around these tips, inducing micro-cracks and lowering the mechanical response. With increasing such dendritic precipitates with sharp tips, both the strength and plasticity would degrade. In contrast, the Co-rich round phase is formed already in the melt at high temperatures via liquid phase separation. Upon rapid cooling, round crystalline second phases are retained. The stress concentration level was calculated to be much lower, and the mechanical response of the Co-containing BMGC is more promising.

3. Microstructural examination showed that V was dissolved in the amorphous matrix and would promote the formation of B2-CuZr precipitates in $(Cu_{47.5}Zr_{47.5}Al_5)_{99}V_1$. Plasticity improvement was observed only in the $(Cu_{47.5}Zr_{47.5}Al_5)_{99}V_1$ alloy and, specifically, fracture strain doubles from 4.7 to 9.4 %. Shear-band multiplication, energy dissipation by viscous flow serration, mechanical twinning and deformation-induced phase transformation of B2-CuZr particles were excluded as the possible mechanism for the current fine B2 particles measuring 3-5 nm. An energy-balance analysis based on deformation-induced B2 particle coarsening produced an interfacial energy of 0.293 J/m^2 for the B2 particle-glassy matrix interface. This energy value agrees with the available amorphous-crystal interface energy in the literature for silicon, which is about 0.4 J/m^2. The result appears to indirectly support the idea suggested by Pauley et al. that plasticity in $(Cu_{47.5}Zr_{47.5}Al_5)_{99}V_1$ is caused by dynamic coarsening of the B2-CuZr particles. It is expected that once the B2 particles grow larger to a level of a few tens of nanometers, twinning or martensitic transformation might be induced.

4. Thus, to enlarge the B2 particles, blunt inlet edge mold is introduced to cast Cu-Zr-Al and Cu-Zr-Al-Co BMGCs. This study explores the effects of the B2 size and distribution, resulted from the sharp or blunt inlet cast mold, on the mechanical plasticity in the CuZrAl and CuZrAlCo bulk metallic glasses. With the sharp mold, the resulting B2 CuZr phase is smaller and fewer, and dispersed randomly in the glass matrix, consistent with the fluid dynamic model prediction by the vena contraction, velocity change and the he Reynolds number arguments. In contrast, with the blunt mold, the more stable fluid results in more and larger B2 particles aggregating as large gray rounded regions.

5. It is found that the B2 particles need to be over a critical size to induce the martensitic transformation into the B19' phase (sometimes with twins embedded). Such martensitic/twinning mechanisms occurred during deformation can effectively help in absorbing the dynamic energy from the propagating shear bands in the Cu based BMGs, preventing catastrophic single major shear-band propagation along the principal shear direction and thus improving plasticity significantly. The martensitic/twinning transformation induced plasticity (TRIP), similar to the toughening mechanisms in TRIP steel or Y-ZrO_2, is indeed very promising in BMGs.

References

[1] Inoue A, Acta Mater. 2000;48:279.

[2] Pampillo CA, J. Mater. Sci. 1975;10:1194.

[3] Chen HS, Rep. Prog. Phys. 1980;43:353.

[4] Greer AL, Science 1995;267:1947.

[5] Johnson WL, MRS Bull. 1999;24:42.

[6] Wang WH, Dong C, Shek CH, Mater. Sci. Eng. R-Rep. 2004;44:45.

[7] Chen MW, Annu. Rev. Mater. Res. 2008;38:445.

[8] Huang JC, Chu JP, Jang JSC, Intermetallics 2009;17:973.

[9] Liu CT, Heatherly L, Easton DS, Carmichael CA, Schneibel JH, Chen CH, Wright JL, Yoo MH, Horton JA, Inoue A, Metall. Mater. Trans. 1998;A29:1811.

[10] Schuh CA, Hufnagel TC, Ramamurty U, Acta Mater. 2007;55:4067.

[11] Zhang ZF, Wu FF, He G, Eckert J, J. Mater. Sci. Technol. 2007;23:747.

[12] Song SX, Bei H, Wadsworth J, Nieh TG, Intermetallics 2008;16:813.

[13] Chen HM, Du XH, Huang JC, Jang JSC, Nieh TG, Intermetallics 2009;17:330.

[14] Hays CC, Kim CP, Johnson WL, Phys. Rev. Lett. 2000;84:2901.

[15] Schroers J, Johnson WL, Phys. Rev. Lett. 2004;93:255506.

[16] Liu YH, Wang G, Wang RJ, Zhao DQ, Pan MX, Wang WH, Science 2007;315:1385.

[17] Conner RD, Dandliker RB, Johnson WL, Acta Mater. 1998;46:6089.

[18] Das J, Tang MB, Kim KB, Theissmann R, Baier F, Wang WH, Eckert J, Phys. Rev. Lett. 2005;94:205501.

[19] Jang JSC, Ciou JY, Hung TH, Huang JC, Du XH, Appl. Phys. Lett. 2008;92:011930.

[20] Xing LQ, Li Y, Ramesh KT, Li J, Hufnagel TC, Phys. Rev. B 2001;64:180201.

[21] Yao KF, Ruan F, Yang YQ, Chen N, Appl. Phys. Lett. 2006;88:122016.

[22] Du XH, Huang JC, Hsieh KC, Lai YH, Chen HM, Jang JSC, Liaw PK, Appl. Phys. Lett. 2007;91:131901.

[23] Park ES, Kim DH, Acta Mater. 2006;54:2597.

[24] Du XH, Huang JC, Chen HM, Chou HS, Lai YH, Hsieh KC, Jang JSC, Liaw PK, Intermetallics 2009;17:607.

[25] Du XH, Huang JC, Hsieh KC, Jang JSC, Liaw PK, Chen HM, Chou HS, Lai YH, Adv. Eng. Mater. 2009;11:387.

[26] Makino A, Li X, Yubuta K, Chang C, Kubota T, Inoue A, Scr. Mater. 2009;60:277.

[27] Park JM, Na JH, Kim DH, Kim KB, Mattern N, Kühn U, Eckert J, Philos. Mag. 2010;90:2619.

[28] Hofmann DC, Suh JY, Wiest A, Duan G, Lind ML, Demetriou MD, Johnson WL, Nature 2008;451:1085.

[29] Pauly S, Gorantla S, Wang G, Kühn U, Eckert J, Nat. Mater. 2010;9:473.

[30] Pauly S, Liu G, Wang G, Kühn U, Mattern N, Eckert J, Acta Mater. 2009;57:5445.

[31] Pauly S, Das J, Duhamel C, Eckert J, Adv. Eng. Mater. 2007;6:487.

[32] Pauly S, Das J, Bednarcik J, Mattern N, Kim KB, Kim DH, Eckert J, Scr. Mater. 2009;60:431.

[33] Wu Y, Xiao YH, Chen GL, Liu CT, Lu ZP, Adv. Mater. 2010;22:2770.

[34] Wu Y, Wang H, Wu HH, Zhang ZY, Hui XD, Chen GL, Ma D, Wang XL, Lu ZP, Acta Mater. 2011;59:2928.

[35] Inoue A, Zhang W, Zhang T, Kurosaka K, Mater. Trans., JIM 2001;42:1149.

[36] Inoue A, Zhang W, Zhang T, Kurosaka K, Acta Mater. 2001;49:2645.

[37] Lin XH, Johnson WL, J. Appl. Phys. 1995;78:6514.

[38] Eckert J, Das J, Kim KB, Baier F, Tang MB, Wang WH, Zhang ZF, Intermetallics 2006;14:876.

[39] Duhamel C, Das J, Pauly S, Lee KS, Eckert J, Rev. Adv. Mater. Sci. 2008;18:527.

[40] Zhang Q, Zhang W, Xie G, Inoue A, Mater. Trans., JIM 2007;48:1626.

[41] Kuo CN, Huang JC, Du XH, Liu XJ, Nieh TG, J. Alloys Compd. 2013;XX:XX.

[42] Kuo CN, Huang JC, Du XH, Chen YC, Liu XJ, Nieh TG, Mater. Sci. Eng., A 2013;561:245.

[43] Takeuchi A, Inoue A, Mater. Trans., JIM 2000;41:1372.

[44] Aghamiry E, Gholampour R, Khademian N, Mater. Sci. Eng. A 2012;547 80.

[45] Klement W, Willens RH, Duwez P, Nature 1960;187:869.

[46] 吳學陞, 工業材料 1999;149:154.

[47] Kavesh S. Metallic Glasses. Mark Park, OH: ASM International, 1978.

[48] Chen HS, Miller CE, Rev. Sci. Instrum. 1970;41:1237.

[49] Chen HS, Turnbull D, Acta Metall. 1969;17:1021.

[50] Chen HS, Krause JT, Sigety EA, J. Non-Cryst. Solids 1974;13:321.

[51] Chen HS, Acta Metall. 1974;22:1505.

[52] Liebermann HH, Graham CD, IEEE Trans. Magn. 1976;12:921.

[53] Drehman AJ, Greer AL, Turnbull D, Appl. Phys. Lett. 1982;41:716.

[54] Kui HW, Greer AL, Turnbull D, Appl. Phys. Lett. 1984;45:615.

[55] Inoue A, Zhang T, Masumoto T, Mater. Trans., JIM 1989;30:965.

[56] Inoue A, Yamaguchi H, Zhang T, Masumoto T, Mater. Trans., JIM 1990;31:104.

[57] Inoue A, Kita K, Zhang T, Masumoto T, Mater. Trans., JIM 1989;30:722.

[58] Inoue A, Zhang T, Masumoto T, Mater. Trans., JIM 1990;31:425.

[59] Inoue A, Kato A, Zhang T, Kim SG, Masumoto T, Mater. Trans., JIM 1991;32:609.

[60] Zhang T, Inoue A, Masumoto T, Mater. Trans., JIM 1991;32:1005.

[61] Inoue A, Nishiyama N, Kimura H, Mater. Trans., JIM 1997;38:179.

[62] Telford M. The case for bulk metallic glass, 2004.

[63] Inoue A. Bulk Amorphous Alloys. Zurich: Trans. Tech., 1998-1999.

[64] Fan C, Takeuchi A, Inoue A, Mater. Trans., JIM 1999;40:42.

[65] Fan C, Inoue A, Appl. Phys. Lett. 2000;77:46.

[66] Lu ZP, Li Y, Ng SC, J. Non-Cryst. Solids 2000;270:103.

[67] Lu ZP, Tan H, Li Y, Ng SC, Scr. Mater. 2000;42:667.

[68] Li Y, Ng SC, Ong CK, Hng HH, Goh TT, Scr. Mater. 1997;36:783.

[69] Waniuk TA, Schroers J, Johnson WL, Appl. Phys. Lett. 2001;78:1213.

[70] Shen TD, He Y, Schwarz RB, J. Mater. Res. 1999;14:2107.

[71] Lu ZP, Liu CT, Acta Mater. 2002;50:3501.

[72] Lu ZP, Liu CT, Phys. Rev. Lett. 2003;91:115505.

[73] Xiao XS, Fang SS, Xia L, Li WH, Hua Q, Dong YD, J. Alloys Compd. 2003;351:324.

[74] Fan GJ, Choo H, Liaw PK, J. Non-Cryst. Solids 2007;353:102.

[75] Chen QJ, Shen J, Zhang DL, Fan HB, Sun J, McCartney DG, Mater. Sci. Eng., A 2006;433:155.

[76] Du XH, Huang JC, Liu CT, Lu ZP, J. Appl. Phys. 2007;101:086108.

[77] Reed-hill RE, Abbaschian R. Physical Metallurgy Principles: I.T. Publishing, 3rd, 1994.

[78] Egami T, Mater. Sci. Eng., A 1997;226:261.

[79] Fang SS, Xiao X, Lei X, Li WH, Dong YD, J. Non-Cryst. Solids 2003;321:120.

[80] Shek CH, Wang YM, Dong C, Mater. Sci. Eng., A 2000;291:78.

[81] Chen W, Wang Y, Qiang J, Dong C, Acta Mater. 2003;51:1899.

[82] Xi XK, Zhao DQ, Pan MX, Wang WH, Intermetallics 2005;13:638.

[83] Ma D, Cao H, Ding L, Chang YA, Hsieh KC, Pan Y, Appl. Phys. Lett. 2005;87:171914.

[84] Lu ZP, Liu CT, J. Mater. Sci. 2004;39:3965.

[85] Park ES, Kang HG, Kim WT, Kim DH, J. Non-Cryst. Solids 2001;279:154.

[86] Amiya K, Inoue A, Mater. Trans., JIM 2001;42:543.

[87] Amiya K, Inoue A, Mater. Trans., JIM 2000;41:1460.

[88] Men H, Hu ZQ, Xu J, Scr. Mater. 2002;46:699.

[89] Ma H, Shi LL, Xu J, Li Y, Ma E, Appl. Phys. Lett. 2005;87:181915.

[90] Cheng YT, Hung TH, Huang JC, Hsieh PJ, Jang JSC, Mater. Sci. Eng., A 2007;449:501.

[91] Cheng YT, Hung TH, Huang JC, Jang JSC, Tsao CYA, Lee F, Intermetallics 2006;14:866.

[92] Zhang ZF, Zhang H, Pan XF, Das J, Eckert J, Philos. Mag. Lett. 2005;85:513.

[93] Liu FX, Liaw PK, Wang GY, Chiang CL, Smith DA, Rack PD, Chu JP, Buchanan RA, Intermetallics 2006;14:1014.

[94] Jiang WH, Fan GJ, Choo H, Liaw PK, Mater. Lett. 2006;60:3537.

[95] Chen HM, Chang YC, Hung TH, Du XH, Huang JC, Jang JSC, Liaw PK, Mater. Trans., JIM 2007;48:1802.

[96] Bei H, Xie S, George EP, Phys. Rev. Lett. 2006;96:105503.

[97] Zhang ZF, Eckert J, Schultz L, Acta Mater. 2003;51:1167.

[98] Inoue A, Zhang T, Zhang W, Takeuchi A, Mater. Trans., JIM 1996;37:99.

[99] Inoue A, Zhang T, Takeuchi A, Zhang W, Mater. Trans., JIM 1996;37:636.

[100] Chaudhar.P, Cuomo JJ, Gambino RJ, Appl. Phys. Lett. 1973;22:337.

[101] Buschow KHJ, Vanderkraan AM, J. Magn. Magn. Mater. 1981;22:220.

[102] Inoue A, Takeuchi A, Zhang T, Metall. Mater. Trans. 1998;A29:1779.

[103] Inoue A, Shinohara Y, Gook JS, Mater. Trans., JIM 1995;36:1427.

[104] Inoue A, Koshiba H, Zhang T, Makino A, J. Appl. Phys. 1998;83:1967.

[105] Inoue A, Katsuya A, Mater. Trans., JIM 1996;37:1332.

[106] Inoue A, Fujita K, Zhang T, Makino A, Mater. Trans., JIM 1998;39:327.

[107] Qin CL, Zhang W, Asami K, Kimura H, Inoue A, J. Mater. Res. 2007;22:1710.

[108] Qin CL, Asami K, Zhang T, Zhang W, Inoue A, Mater. Trans., JIM 2003;44:1042.

[109] Pang SJ, Zhang T, Asami K, Inoue A, Acta Mater. 2002;50:489.

[110] Pang S, Zhang T, Asami K, Inoue A, Mater. Trans., JIM 2002;43:2137.

[111] Asami K, Qin CL, Zhang T, Inoue A, Mater. Sci. Eng., A 2004;375-377:235.

[112] Li Y, Bai HY, Wen P, Liu ZX, Zhao ZF, J. Phys. 2003;15:4809.

[113] Li Y, Bai HY, J. Non-Cryst. Solids 2005;351:2378.

[114] Tanaka H, Senoh H, Kuriyama N, Aihara K, Terashita N, Nakahata T, Mater. Sci. Eng., B 2004;108:81.

[115] Mukai T, Nieh TG, Kawamura Y, Inoue A, Higashi K, Intermetallics 2002;10:1071.

[116] Zhang ZF, He G, Eckert J, Schultz L, Phys. Rev. Lett. 2003;91:045505.

[117] Spaepen F, Scr. Mater. 2006;54:363.

[118] Spaepen F, Acta Metall. 1977;25:407.

[119] Schroers J, Pham Q, Desai A, J. Microelectromech. Syst. 2007;16:240.

[120] Schroers J, Nguyen T, O'Keeffe S, Desai A, Mater. Sci. Eng., A 2007;449:898.

[121] Li HQ, Tao KX, Fan C, Liaw PK, Choo H, Appl. Phys. Lett. 2006;89:041921.

[122] Li HQ, Fan C, Choo H, Liaw PK, Mater. Trans., JIM 2006;48:1752.

[123] Dalla Torre FH, Dubach A, Siegrist ME, Loffler JF, Appl. Phys. Lett. 2006;89:091918.

[124] Zhang J, Park JM, Kim DH, Kim HS, Mater. Sci. Eng., A 2007;449:290.

[125] Xiao XS, Fang SS, Xia L, Li WH, Hua Q, Dong Y, J. Non-Cryst. Solids 2003;330:242.

[126] Jiang WH, Liu FX, Jiang F, Qiu KQ, Choo H, Liaw PK, J. Mater. Res. 2007;22:2655.

[127] Jiang WH, Fan GJ, Liu F, Wang GY, Choo H, Liaw PK, Int. J. Plast. 2008;24:1.

[128] Zheng Q, Cheng S, Strader JH, Ma E, Xu J, Scr. Mater. 2007;56:161.

[129] Xie S, George EP, Intermetallics 2008;16:485.

[130] Wu WF, Han Z, Li Y, Appl. Phys. Lett. 2008;93:061908.

[131] Wu FF, Zhang ZF, Mao SX, Eckert J, Philos. Mag. Lett. 2009;89:178.

[132] Volkert CA, Donohue A, Spaepen F, J. Appl. Phys. 2008;103:083539.

[133] Schuster BE, Wei Q, Hufnagel TC, Ramesh KT, Acta Mater. 2008;56:5091.

[134] Schuster BE, Wei Q, Ervin MH, Hruszkewycz SO, Miller MK, Hufnagel TC, Ramesh KT, Scr. Mater. 2007;57:517.

[135] Lee CJ, Huang JC, Nieh TG, Appl. Phys. Lett. 2007;91:161913.

[136] Lai YH, Lee CJ, Cheng YT, Chou HS, Chen HM, Du XH, Chang CI, Huang JC, Jian SR, Jang JSC, Nieh TG, Scr. Mater. 2008;58:890.

[137] Huang YJ, Shen J, Sun JF, Appl. Phys. Lett. 2007;90:081919.

[138] Yang Y, Ye JC, Lu J, Liu FX, Liaw PK, Acta Mater. 2009;57:1613.

[139] Wu WF, Zhang CY, Zhang YW, Zeng KY, Li Y, Intermetallics 2008;16:1190.

[140] Wu WF, Li Y, Schuh CA, Philos. Mag. 2008;88:71.

[141] Jiang WH, Qiu KQ, Liu FX, Choo H, Liaw PK, Adv. Eng. Mater. 2007;9:147.

[142] Wang K, Fujita T, Zeng YQ, Nishiyama N, Inoue A, Chen MW, Acta Mater. 2008;56:2834.

[143] Cohen MH, Turnbull D, J. Chem. Phys. 1959;31:1164.

[144] Polk DE, Turnbull D, Acta Metall. 1972;20:493.

[145] Argon AS, Acta Metall. 1979;27:47.

[146] Yang B, Liu CT, Nieh TG, Appl. Phys. Lett. 2006;88:221911.

[147] Srolovitz D, Vitek V, Egami T, Acta Metall. 1983;31:335.

[148] Schuh CA, Lund AC, Nat. Mater. 2003;2:449.

[149] Falk ML, Phys. Rev. B 1999;60:7062.

[150] Argon AS, Kuo HY, Mater. Sci. Eng. 1979;39:101.

[151] Pan D, Inoue A, Sakurai T, Chen MW, Proc. Natl. Acad. Sci. U.S.A. 2008;105:14769.

[152] Leamy HJ, Wang TT, Chen HS, Metall. Mater. Trans. B 1972;3:699.

[153] Pampillo CA, Reimschuessel AC, J. Mater. Sci. 1974;9:718.

[154] Spaepen S, Turnbull D, Scr. Metall. 1974;8:563.

[155] Chou CPP, Spaepen F, Acta Metall. 1975;23:609.

[156] Dai LH, Yan M, Liu LF, Bai YL, Appl. Phys. Lett. 2005;87:141916.

[157] Yang B, Morrison ML, Liaw PK, Buchanan RA, Wang GY, Liu CT, Denda M, Appl. Phys. Lett. 2005;86:141904.

[158] Fan C, Inoue A, Mater. Trans., JIM 2000;41:1467.

[159] Fan C, Ott RT, Hufnagel TC, Appl. Phys. Lett. 2002;81:1020.

[160] Fan C, Qiao DC, Wilson TW, Choo H, Liaw PK, Mater. Sci. Eng., A 2006;431:158.

[161] Wada T, Inoue A, Greer AL, Appl. Phys. Lett. 2005;86:251907.

[162] Pauly S, Das J, Mattern N, Kim DH, Eckert J, Intermetallics 2009;17:453.

[163] Park BJ, Chang HJ, Kim DH, Kim WT, Chattopadhyay K, Abinandanan TA, Bhattacharyya S, Phys. Rev. Lett. 2006;96:245503.

[164] Park ES, Kyeong JS, Kim DH, Scr. Mater. 2007;57:49.

[165] Pan DG, Zhang HF, Wang AM, Hu ZQ, Appl. Phys. Lett. 2006;89:261904.

[166] Sung DS, Kwon OJ, Fleury E, Kim KB, Lee JC, Kim DH, Kim YC, Met. Mater. Int. 2004;10:575.

[167] Kim YC, Lee JC, Cha PR, Ahn JP, Fleury E, Mater. Sci. Eng., A 2006;437:248.

[168] Dai CL, Guo H, Shen Y, Li Y, MA E, Xu J, Scr. Mater. 2006;54:1403.

[169] Hu CJ, Wu HM, J. Alloys Compd. 2007;434-435:390.

[170] Zhang QS, Zhang HF, Deng YF, Ding BZ, Hu ZQ, Scr. Mater. 2003;49:273.

[171] Zhang T, Inoue A, Mater. Trans., JIM 1999;40:301.

[172] Li C, Saida J, Kiminami M, Inoue A, J. Non-Cryst. Solids 2000;261:108.

[173] Inoue A, Zhang W, Appl. Phys. Lett. 2003;83:2351.

[174] Inoue A, Zhang W, Tsurui T, Yavari AR, Greer AL, Philos. Mag. Lett. 2005;85:221.

[175] Seo JW, Schryvers D, Acta mater. 1998;46:1165.

[176] Schryvers D, J. Phys. 1995;5:1047.

[177] Garde RJ. Fluid Mechanics Through Problems: New Age International, 1997.

[178] Oertel H, Prandtl L, Böhle M, Mayes K. Prandtl's Essentials of Fluid Mechanics: Springer, 2004.

[179] Gurland J. Quantitative Microscopy. New York: McGraw-Hill, 1968.

[180] Ye JC, Lu J, Yang Y, Liaw PK, Intermetallics 2010;18:385.

[181] Zhang ZF, Eckert J, Phys. Rev. Lett. 2005;94:094301.

[182] Spaepen F, Acta Metall. 1975;23:615.

[183] Wright WJ, Saha R, Nix WD, Mater. Trans., JIM 2001;42:642.

[184] Song SX, Nieh TG, Intermetallics 2009;17:762.

[185] Song SX, Wang XL, Nieh TG, Scr. Mater. 2010;62:847.

[186] Kuo CN, Chen HM, Du XH, Huang JC, Intermetallics 2010;18:1648.

[187] Chen HM, Huang JC, Song SX, Nieh TG, Jang JSC, Appl. Phys. Lett.

2009;94:141914.

[188] Zhang Y, Stelmashenko NA, Barber ZH, Wang WH, Lewandowski JJ, Greer AL, J. Mater. Res. 2007;22:419.

[189] Yang B, Liu CT, Nieh TG, Morrison ML, Liaw PK, Buchanan RA, J. Mater. Res. 2006;21:915.

[190] Lewandowski JJ, Greer AL, Nat. Mater. 2006;5:15.

[191] Han Z, Li Y, J. Mater. Res. 2009;24:3620.

[192] Hull D, Clyne TW. An Introduction To Composite Materials: Cambridge, 1996.

[193] Wang JG, Zhao DQ, Pan MX, Wang WH, Song SX, Nieh TG, Scr. Mater. 2010;62:477.

[194] Wang L, Bei H, Gao YF, Lu ZP, Nieh TG, Acta Mater. 2011;59:7627.

[195] Nagasaki S, Hirabayashi M. Binary Alloy Phase Diagrams. Beijing, China: Metallurgical Industry Press, 2004.

[196] Xu D, Lohwongwatana B, Duan G, Johnson WL, Garland C, Acta Mater. 2004;52:2621.

[197] Tang MB, Zhao DQ, Pan MX, Wang WH, Chin. Phys. Lett. 2004;21:901.

[198] Hirata A, Hirotsu Y, Matsubara E, Ohkubo T, Hono K, Phys. Rev. B 2006;74:184204.

[199] Bernstein N, Aziz MJ, Kaxiras E, Phys. Rev. B 1998;58:4579.

[200] Boyd JD, Nicholson RB, Acta Mater. 1971;19:1101.

[201] Christian J. The Theory of Transformation in Metals and Alloys. Oxford: Pergamon Press, 1975.

[202] Reynolds O, Philos. Trans. R. Soc. London 1883;174:935.

[203] Rott N, Annu. Rev. Fluid Mech. 1990;22:1.

[204] Konstantinova N, Kurochkin A, Popel P, EPJ Web of Conferences 2011;15:1.

[205] Lu XY, Kolbe M, Herlach DM, Mater. Res. Soc. 2003;754:21.

Tables

Table 1.1 Fundamental properties and application fields of bulk amorphous and nanocrystalline alloys [1].

Fundamental characteristic	Application field
High strength	Machinery structural materials
High hardness	Optical precision materials
High fracture toughness	Die materials
High impact fracture energy	Tool materials
High fatigue strength	Cutting materials
High elastic energy	Electrode materials
High corrosion resistance	Corrosion resistant materials
High wear resistance	Hydrogen storage materials
High viscous flowability	Ornamental materials
High reflection ratio	Composite materials
Good soft magnetism	Writing appliance materials
High frequency permeability	Sporting goods materials
High magnetostriction	Bonding materials
Efficient electrode (Chlorine gas)	Soft magnetic materials
High hydrogen storage	High magnetostrictive materials

Table 1.2 Relationship between the heats of mixing among the component elements in the Cu-V-Zr-Al and Cu-Co-Zr-Al alloy system (unit: kJ/mol) [43].

	Cu	V	Co	Zr	Al
Cu		+5	+10	-23	-1
V	+5		--	-4	-16
Co	+10	--		-41	-19
Zr	-23	-4	-41		-44
Al	-1	-16	-19	-44	

Table 2.1 Summary of ΔT_x (= T_x - T_g), T_{rg} (= T_g/T_l), γ (= $T_x/(T_g+T_l)$), critical cooling rate R_c and critical section thickness Z_c for typical BMGs [71].

Alloy	T_x-T_g	T_g/T_l	$T_x/(T_g+T_l)$	R_c(K/s)	Z_c(mm)
$Mg_{80}Ni_{10}Nd_1$	16.3	0.517	0.353	1251.4	0.6
$Mg_{75}Ni_{15}Nd_{10}$	20.4	0.57	0.379	46.1	2.8
$Mg_{70}Ni_{15}Nd_{15}$	22.3	0.553	0.373	178.2	1.5
$Mg_{65}Ni_{20}Nd_{15}$	42.1	0.571	0.397	30	3.5
$Mg_{65}Ni_{25}Nd_{10}$	54.9	0.551	0.401	50	7
$Zr_{66}Al_8Ni_{26}$	35.6	0.537	0.368	66.6	
$Zr_{66}Al_8Cu_7Ni_{19}$	58.4	0.552	0.387	22.7	
$Zr_{66}Al_8Cu_{12}Ni_{14}$	77.4	0.559	0.401	9.8	
$Zr_{66}Al_9Cu_{16}Ni1_9$	79.5	0.561	0.403	4.1	
$Zr_{65}Al_{7.5}Cu_{17.5}Ni_{10}$	79.1	0.562	0.403	1.5	16
$Zr_{57}Ti_5Al_{10}Cu_{20}Ni_8$	43.3	0.591	0.395	10	10
$Zr_{38.5}Ti_{16.5}Ni_{9.75}Cu_{15.25}Be_{20}$	48	0.628	0.415	1.4	
$Zr_{39.88}Ti_{15.12}Ni_{9.98}Cu_{13.77}Be_{21.}$	57	0.625	0.42	1.4	
$Zr_{41.2}Ti_{13.8}Cu_{12.5}Ni_{10}Be_{22.5}$	49	0.626	0.415	1.4	50
$Zr_{42.63}Ti_{12.37}Cu_{11.25}Ni_{10}Be_{23.75}$	89	0.589	0.424	5	
$Zr_{44}Ti_{11}Cu_{10}Ni_{10}Be_{25}$	114	0.518	0.404	12.5	
$Zr_{45.38}Ti_{9.62}Cu_{8.75}Ni_{10}Be_{26.25}$	117	0.503	0.397	17.5	
$Zr_{46.25}Ti_{8.25}Cu_{7.5}Ni_{10}Be_{27.5}$	105	0.525	0.402	28	
$La_{55}A_{l25}Ni_{20}$	64.3	0.521	0.388	67.5	3
$La_{55}Al_{25}Ni_{15}Cu_5$	67.6	0.526	0.394	34.5	
$La_{55}Al_{25}Ni_{10}Cu_{10}$	79.8	0.56	0.42	22.5	5
$La_{55}Al_{25}Ni_5Cu_{15}$	60.9	0.523	0.389	35.9	
$La_{55}Al_{25}Cu_{20}$	38.9	0.509	0.366	72.3	3
$La_{55}Al_{25}Ni_5Cu_{10}Co_5$	76.6	0.566	0.421	18.8	9
$La_{66}Al_{14}Cu_{20}$	54	0.54	0.399	37.5	2
$Pd_{40}Cu_{30}Ni_{10}P_{20}$	78.9	0.69	0.464	0.1	72
$Pd_{81.5}Cu_2Si_{16.5}$	37	0.577	0.387	2	
$Pd_{79.5}Cu_4Si_{16.5}$	40	0.585	0.392	500	0.75
$Pd_{77.5}Cu_6Si_{16.5}$	41	0.602	0.4	100	1.5
$Pd_{77}Cu_6Si_{17}$	44	0.569	0.388	125	2
$Pd_{73.5}Cu_{10}Si_{16.5}$	40	0.568	0.385	2	
$Pd_{40}Ni_{40}P_{20}$	63	0.585	0.409	0.167	25
$Nd_{60}Al_{15}Ni_{10}Cu_{10}Fe_5$	45	0.552	0.393	5	
$Nd_{61}Al_{11}Ni_8Co_5Cu_{15}$	24	0.598	0.394	6	
$Cu_{60}Zr_{30}Ti_{10}$	50	0.619	0.409	4	
$Cu_{54}Zr_{27}Ti_9Be_{10}$	42	0.637	0.412	5	
$Ti_{34}Zr_{11}Cu_{47}Ni_8$	28.8	0.597	0.389	100	4.5
$Ti_{50}Ni_{24}Cu_{20}B_1Si_2Sn_3$	74	0.554	0.393	1	

Table 2.2 Summary of the mechanical properties of the previously reported Mg-based BMGs under compression tests [128].

Alloy composition (at%)	Sample diameter (mm)	$_f$ (MPa)	$_p$ (%)
$Mg_{65}Cu_{20}Ag_{10}Y_2Gd_8$	1	956	0.3
$Mg_{65}Cu_{20}Ag_5Gd_{10}$	1	909	0.5
$Mg_{65}Cu_{15}Ag_{10}Gd_{10}$	1	935	0.2
$Mg_{65}Cu_{7.5}Ni_{7.5}Zn_5Ag_5Y_{10}$	1	832	0
$Mg_{65}Cu_{7.5}Ni_{7.5}Zn_5Ag_5Y_5Gd_5$	1	928	0.57
$Mg_{65}Cu_{15}Ag_5Pd_5Gd_{10}$	2	817	0.2
$Mg_{75}Cu_{15}Gd_{10}$	2	743	0
$Mg_{75}Cu_5Ni_{10}Gd_{10}$	2	874	0.2
$Mg_{65}Cu_{25}Gd_{10}$	2	834	0
$Mg_{65}Ni_5Cu_{20}Gd_{10}$	2	904	0.15
$Mg_{65}Cu_{7.5}Ni_{7.5}Zn_5Ag_5Y_{10}$	4	490-650	0
$Mg_{65}Cu_{15}Ag_5Pd_5Y_{10}$	5	770	0
$Mg_{61}Cu_{28}Gd_{11}$	4	461-732	0
$Mg_{61}Cu_{28}Gd_{11}$	1	1040-1100	0.4

Table 2.3 Summary of the mechanical properties of the previously reported Cu-Zr-Al-(Y, Gd, Ag) BMGs under compression tests [23, 31, 38, 39, 164, 166].

Alloy composition (at%)	d (mm)	E (MPa)	σ_f (MPa)	ε_p (%)
$Cu_{46}Zr_{47}Al_7$	1	85	1960	1.2
$Cu_{46}Zr_{45}Al_7Y_2$	1	85	1870	3.1
$Cu_{46}Zr_{42}Al_7Y_5$	1	85	1750	3.1
$Cu_{46}Zr_{37}Al_7Y_{10}$	1	85	1640	0
$Cu_{46}Zr_{32}Al_7Y_{15}$	1	85	1090	0
$Cu_{46}Zr_{46}Al_7Gd_1$	1	97	2070	1.75
$Cu_{46}Zr_{45}Al_7Gd_2$	1	97	2080	2.28
$Cu_{46}Zr_{44}Al_7Gd_3$	1	97	2050	0.7
$Cu_{46}Zr_{43}Al_7Gd_4$	1	97	2020	0.47
$Cu_{46}Zr_{42}Al_7Gd_5$	1	97	1920	0
$Cu_{50}Zr_{50}$	2	84	1794	4.0
$Cu_{47.5}Zr_{47.5}Al_5$	2	84	2265	16
$Cu_{46}Zr_{47}Al_7$	2	95	1900	0
$Cu_{43}Zr_{43}Al_7Ag_7$	2	115	1850	8.0
$Cu_{46}Zr_{46}Al_7Gd_1$	2	94	2020	0.47
$Cu_{46}Zr_{45}Al_7Gd_2$	2	94	2030	2.05
$Cu_{46}Zr_{44}Al_7Gd_3$	2	94	1980	1.44
$Cu_{46}Zr_{43}Al_7Gd_4$	2	94	1860	0
$Cu_{46}Zr_{42}Al_7Gd_5$	2	93	1790	0

d: sample diameter

E: Young’s modulus

σ_f: compressive fracture strength

ε_p: plastic elongation

Table 3.1 Fundamental data related to the component elements in this study.

Symbol	Atomic weight	Structure	Electron-negativity	Atomic size (Å)	Melting point (^oC)	Density (g/cm^3)	Poisson ratio
Cu	63.546	FCC	2.00	1.28	1084	8.96	0.34
Zr	91.220	HCP	1.33	1.60	1855	6.49	0.34
Al	26.982	FCC	1.61	1.43	660	2.70	0.35
V	50.942	BCC	1.63	1.32	1902	6.11	0.37
Co	58.933	HCP	1.88	1.25	1495	8.90	0.31

FCC: face-centered cubic

HCP: hexagona close-packed

BCC: body-centered cubic

Table 4.1 Representative EDS results of the $(Cu_{47.5}Zr_{47.5}Al_5)_{90}V_{10}$ and $(Cu_{47.5}Zr_{47.5}Al_5)_{90}Co_{10}$ alloys. The composition data are averaged from 10 measurements.

Alloy	Element	Average (at%)	Darker Domain (at%)	Brighter Domain (at%)
$(Cu_{47.5}Zr_{47.5}Al_5)_{90}V_{10}$	Cu	44.56	42.27	49.41
	Zr	43.35	38.08	43.54
	V	9.00	14.58	3.93
	Al	3.09	5.07	3.12
	Total	100.00	100.00	100.00
$(Cu_{47.5}Zr_{47.5}Al_5)_{90}Co_{10}$	Cu	44.17	55.73	35.58
	Zr	42.78	32.29	41.43
	Co	10.09	1.04	20.72
	Al	2.96	10.94	2.27
	Total	100.00	100.00	100.00

Table 4.2 Summary of volume fractions, the ratio of precipitated phase length over root-radius a/ρ, precipitate orientation factor $\sigma_t/(F_\theta\ \sigma_0)$, and mechanical properties such as elastic modulus (E), yield stress (σ_y), plastic strain (ε_p), and total strain (ε_t) of the as-cast Cu-based BMG compressed at a strain rate of 1 x 10^{-4} s^{-1} at room temperature. All of data were averaged by at least three tests, and the maximum standard deviation is 6%, except for the precipitate volume fraction of the Co-containing alloys where the second-phase particle distribution is not uniform.

Specimen	E (GPa)	σ_y (GPa)	ε_p (%)	ε_t (%)	Precipitated phase (vol%)	a / ρ	$\sigma_t / (F_\theta\ \sigma_0)$
$Cu_{47.5}Zr_{47.5}Al_5$	87	1.8	2.7	4.7	--	--	--
$(Cu_{47.5}Zr_{47.5}Al_5)_{97}V_3$	88	1.9	0	2.0	8	7.75	6.60
$(Cu_{47.5}Zr_{47.5}Al_5)_{95}V_5$	85	1.3	0	1.4	10	13.17	8.26
$(Cu_{47.5}Zr_{47.5}Al_5)_{90}V_{10}$	84	1.1	0	1.3	15	14.50	8.62
$(Cu_{47.5}Zr_{47.5}Al_5)_{97}Co_3$	91	2.0	6.2	8.2	20	1.34	3.32
$(Cu_{47.5}Zr_{47.5}Al_5)_{95}Co_5$	91	1.9	1.7	3.6	26	1.92	3.77
$(Cu_{47.5}Zr_{47.5}Al_5)_{90}Co_{10}$	89	1.5	1.7	3.4	29	1.99	3.82

Table 4.3 Summary of the volume fractions in various specimens under the as-cast and after deformed conditions. The volume fraction for the as-cast $Cu_{47.5}Zr_{47.5}Al_5$ is quite low, difficult to be calculated to a precise value, thus shown as <0.5% in the Table.

Specimen	As cast		After deformed	
	B2 ZrCu	V-containing phase	B2 ZrCu	V-containing phase
$Cu_{47.5}Zr_{47.5}Al_5$	<0.5%	0	1.5±0.2%	0
$(Cu_{47.5}Zr_{47.5}Al_5)_{99}V_1$	1±0.3%	0	7.2±1%	0

Table 4.4 Summary of mechanical properties of the as-cast Cu-based BMG at a strain rate of 1 x 10^{-4} s^{-1} at room temperature.

Specimen	E (GPa)	σ_y (GPa)	ε_e (%)	ε_p (%)	ε_t (%)
$Cu_{47.5}Zr_{47.5}Al_5$	87	1.8	2.0	2.7	4.7
$(Cu_{47.5}Zr_{47.5}Al_5)_{99}V_1$	87	1.8	2.0	7.4	9.4

Table 4.5 Summary of microstructural and mechanical properties of the as-cast $Cu_{47.5}Zr_{47.5}Al_5$ and $Cu_{47.5}Zr_{48}Al_4Co_{0.5}$ BMGs. The $Cu_{47.5}Zr_{48}Al_4Co_{0.5}$ BMG, cast by the B mold, exhibits apparent work hardening, indicating the more ductile nature. The particles size and volume fraction for the major second phase B2 or its transformed martensitic B19' phase under the as-cast (AC) and deformed (DF) states are also compiled in this table. Note that d is the particle size, and V_f is the volume fraction. The experimental errors are all within 10%.

Specimen	Mold type	AC B2 d (nm)	AC B2 V_f	E (GPa)	σ_y (GPa)	ε_t (%)	DF B19' d (nm)	DF B19' V_f
$Cu_{47.5}Zr_{47.5}Al_5$	S mold	~3	<0.5%	87	1.8	~5	~5	~1.5%
$Cu_{47.5}Zr_{47.5}Al_5$	B mold	~10	<1%	84	1.7	17	~20	~5%
$Cu_{47.5}Zr_{48}Al_4Co_{0.5}$	S mold	~4	~1%	85	1.7	20	~10	~3%
$Cu_{47.5}Zr_{48}Al_4Co_{0.5}$	B mold	~20	~10%	84	1.7	23	~25	~10%

Table 5.1 The measured values about one shear event for the $Cu_{50}Zr_{43}Al_7$ BMG. H^* is the heat content of the shear band induced by one single shear; x is a half-width of hot zone from the center of shear band; t is the elapsed time of one single shear event; ρ, C and α are the density, specific heat capacity and thermal diffusivity of BMG, respectively; and ΔT is the temperature rise above ambient temperature. Note that the H of $1.8\text{x}10^3$ J/m^2 is an average value based on several major serrations in the stress-strain curve. The values of x, t, ρ, C and α are extracted from the results of Zheng et al. [128].

Event	H^* (J/m^2)	x (μm)	t (s)	ρ (kg/m^3)	C (J/(kgK))	α (m^2/s)	ΔT (K)
Shear	$1.8\text{x}10^3$	0.4	$1\text{x}10^{-3}$	$7.1\text{x}10^3$	$3.9\ \text{x}10^2$	$2.3\ \text{x}10^{-6}$	7
Failure	$2.2\text{x}10^5$						471

Table 5.2 Calculated flow velocity, Velocity change when diameter reduction, and the Reynolds number for the two cast routes, one using sharp inlet edged mold and one using blunt inlet edged and gradual cross-sectional area reduction mold. The kinematic viscosity of $Cu_{90}Al_{10}$ at 1450°C = 4.5 x 10^{-7} m^2/s [204].

Position	Cast by the S mold			Cast by the B mold		
	Flow velocity (m/s)	Velocity change (m/s^2)	Reynolds number (vL/ν)	Flow velocity (m/s)	Velocity change (m/s^2)	Reynolds number (vL/ν)
Region 1, tank	0.03	20.7	916	0.02	0.1	274
Region 2, vena contraction	2.13	2107.0	7500	--	--	--
Region 3, pipe of 4 mm	--	--	--	0.20	6.0	1741
Region 3, pipe of 3 mm	--	--	--	0.35	30.3	2322
Region 3, pipe of 2 mm	1.34	--	5953	0.78	--	3483

Figures

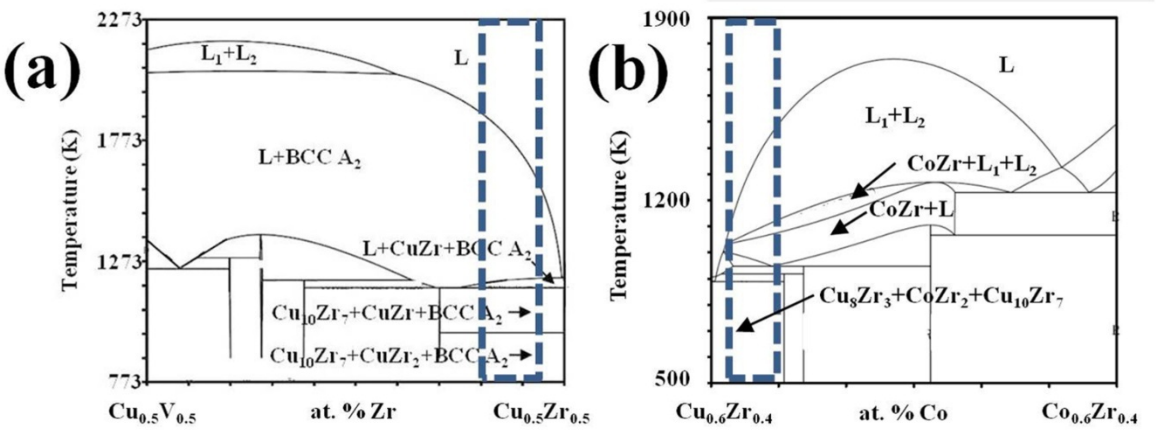

Figure 1.1 The vertical section of (a) the Cu-Zr-V alloy system at 50 at% Cu, and (b) the Cu-Zr-Co alloy system at 40 at% Zr. The selected composition range in this study is indicated by the frame. (c) XRD curves for the alloys with V and Co contents from 0 to 10 at%.

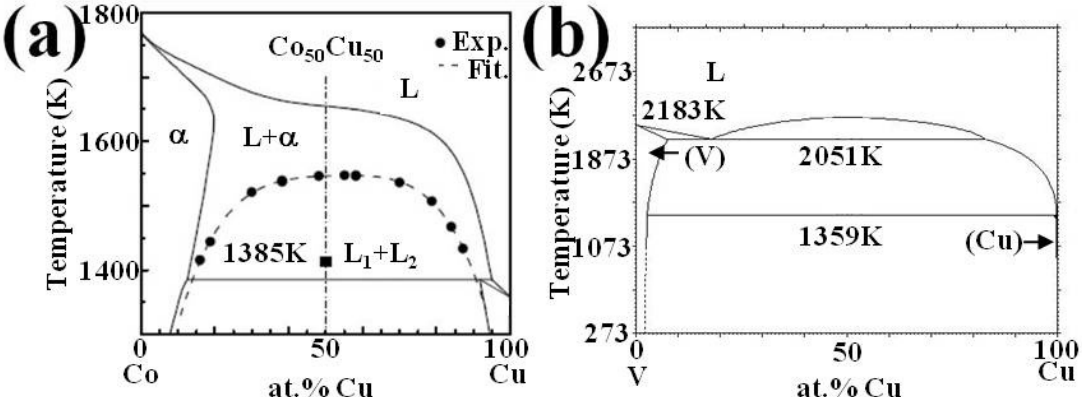

Figure 1.2 The related phase diagrams: (a) the Co-Cu binary [205] (b) the V-Cu binary [195] and (c) the simulated $Cu_{50}V_{50}Zr_0$ to $Cu_{50}V_0Zr_{50}$ section.

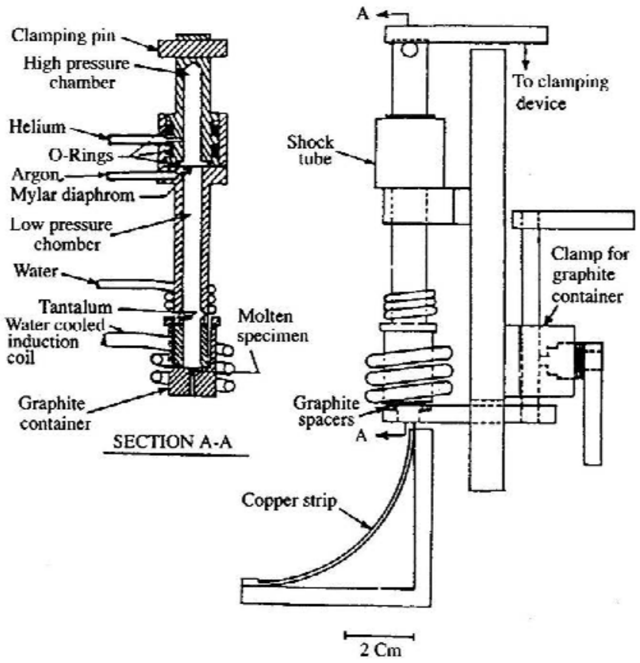

Figure 2.1 A schematic diagram of the splat quenching method [46].

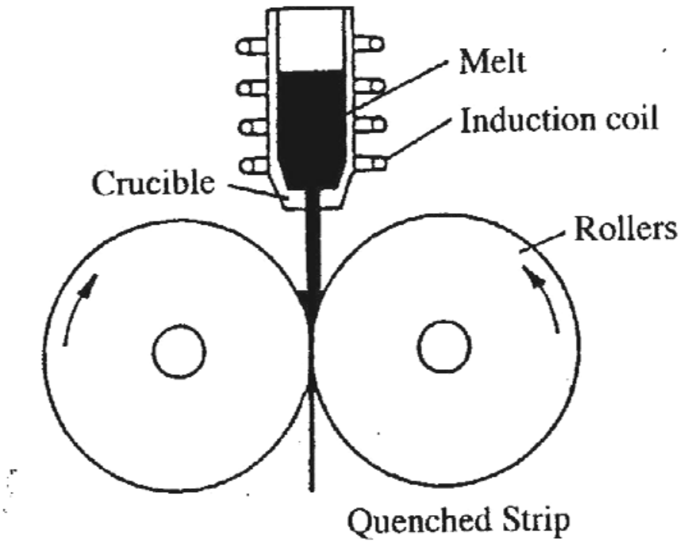

Figure 2.2 A schematic diagram of the two roller quenching method [46].

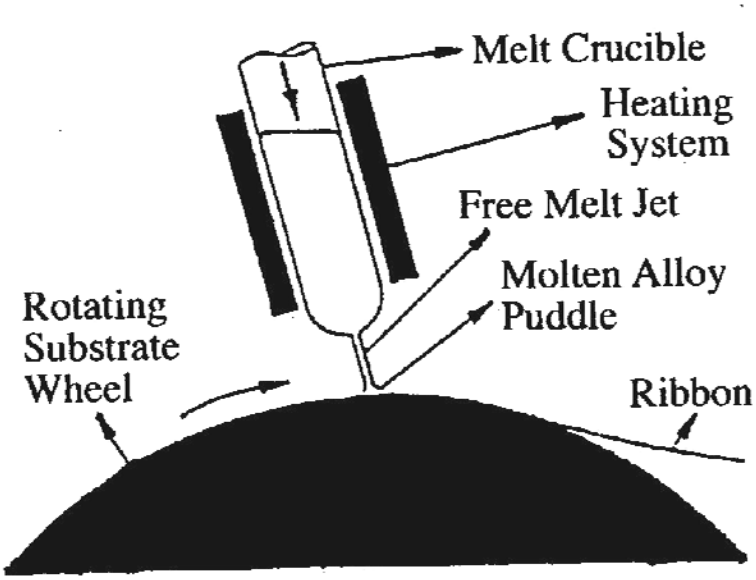

Figure 2.3   A schematic diagram of the chill block melt spinning [46].

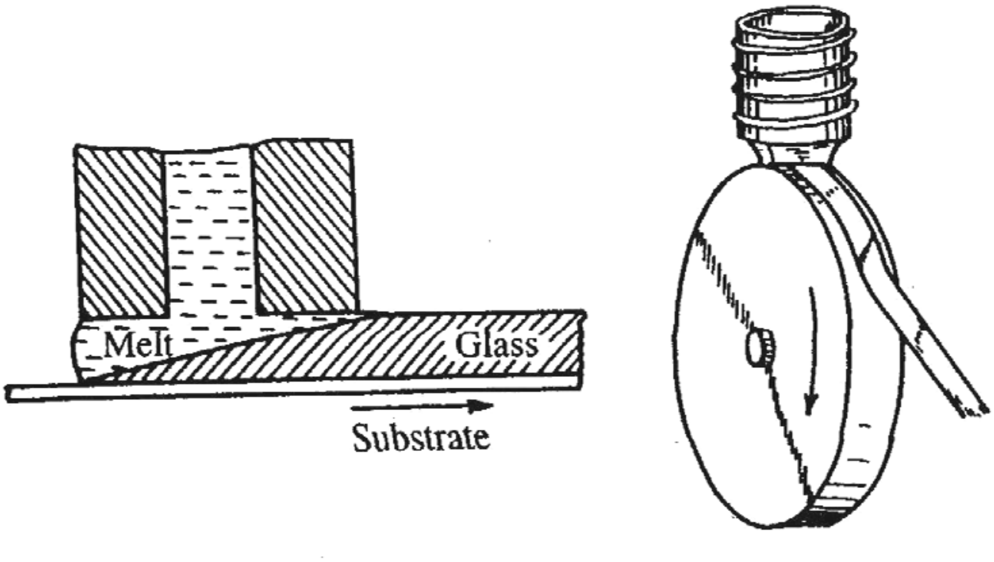

Figure 2.4   A schematic diagram of the planar flow casting process [46].

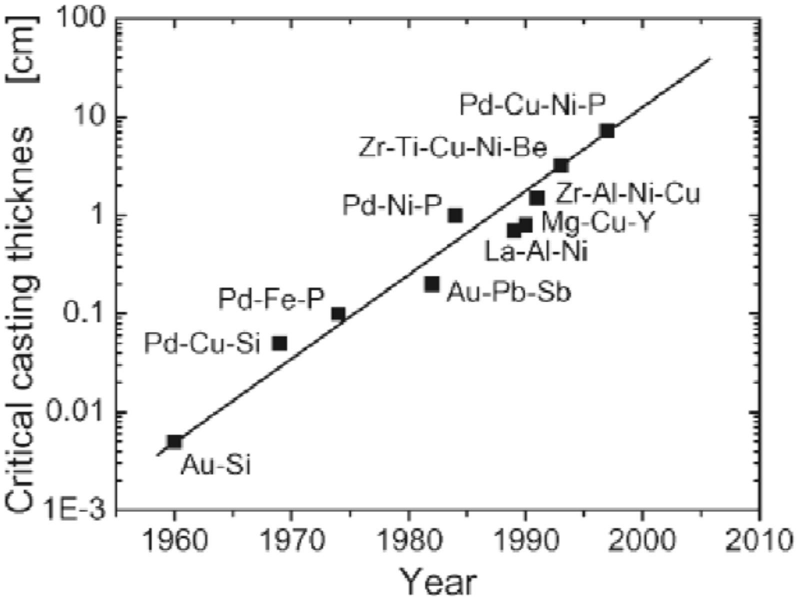

Figure 2.5 Critical casting thicknesses for glass formation as a function of the year and corresponding alloy [62].

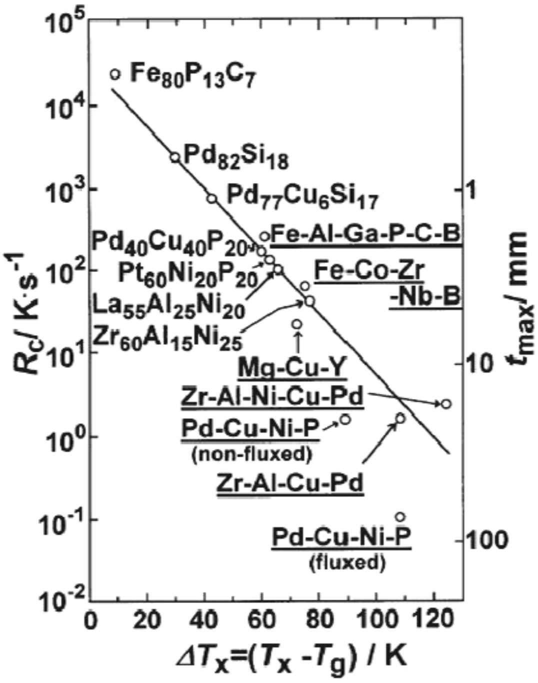

Figure 2.6 Relationship between the critical cooling rate (R_c), the maximum sample thickness (t_{max}) and supercooled liquid region (ΔT_x) for BMG systems [1].

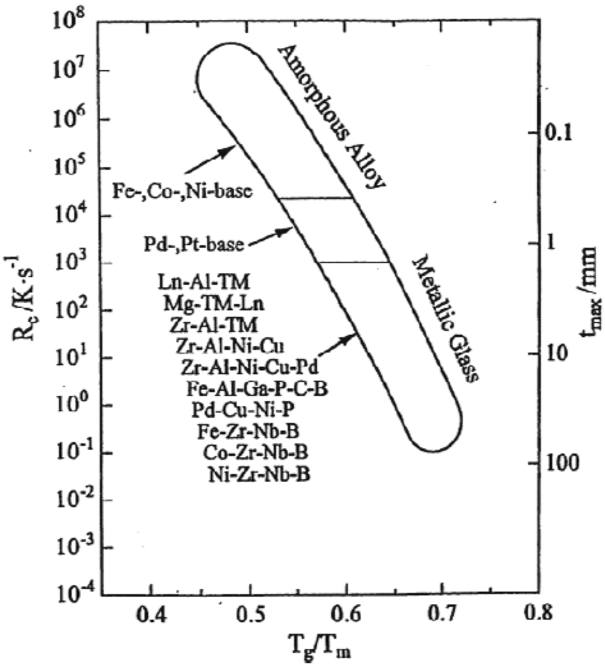

Figure 2.7 Relationship between the critical cooling rate (R_c), the maximum sample thickness (t_{max}) and reduced glass transition temperature (T_g/T_m) for BMG systems [1].

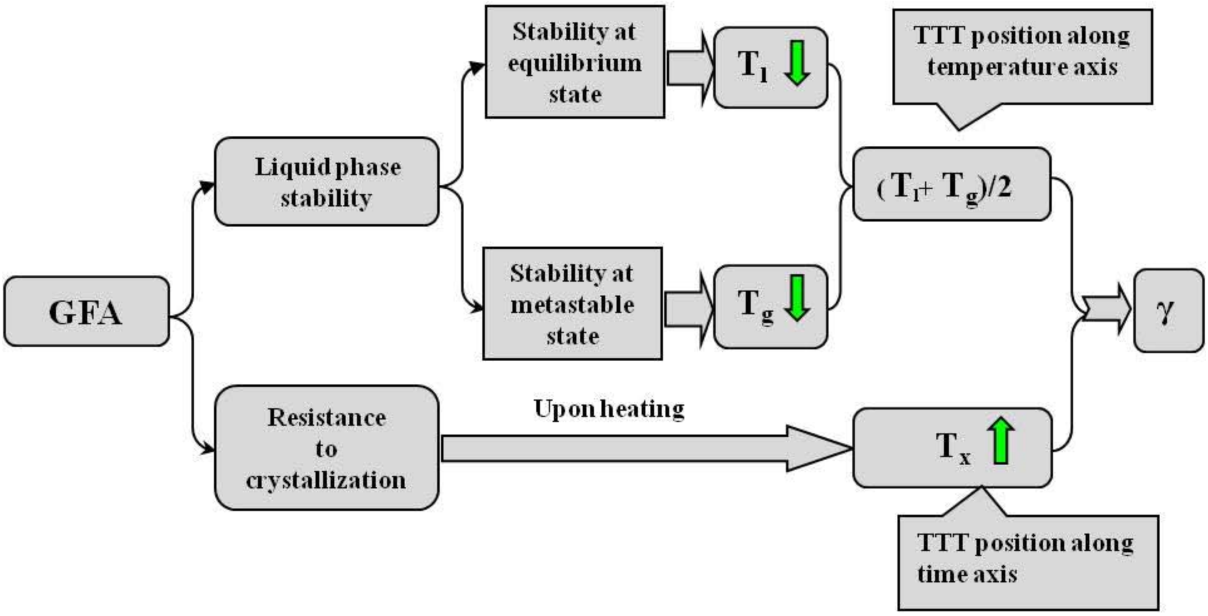

Figure 2.8 The γ parameter of GFA for metallic glasses [71].

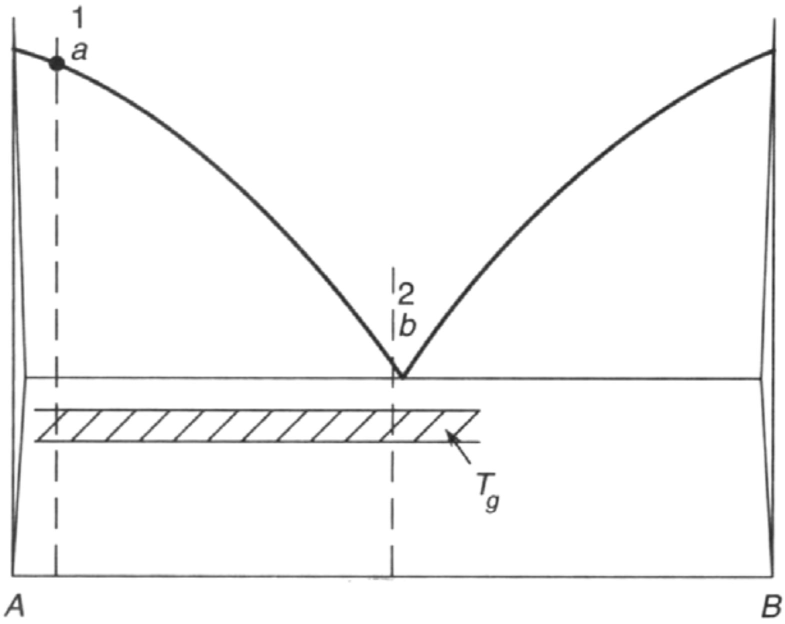

Figure 2.9 A illustration of binary alloy system in phase diagram with a single deep eutectic point [77].

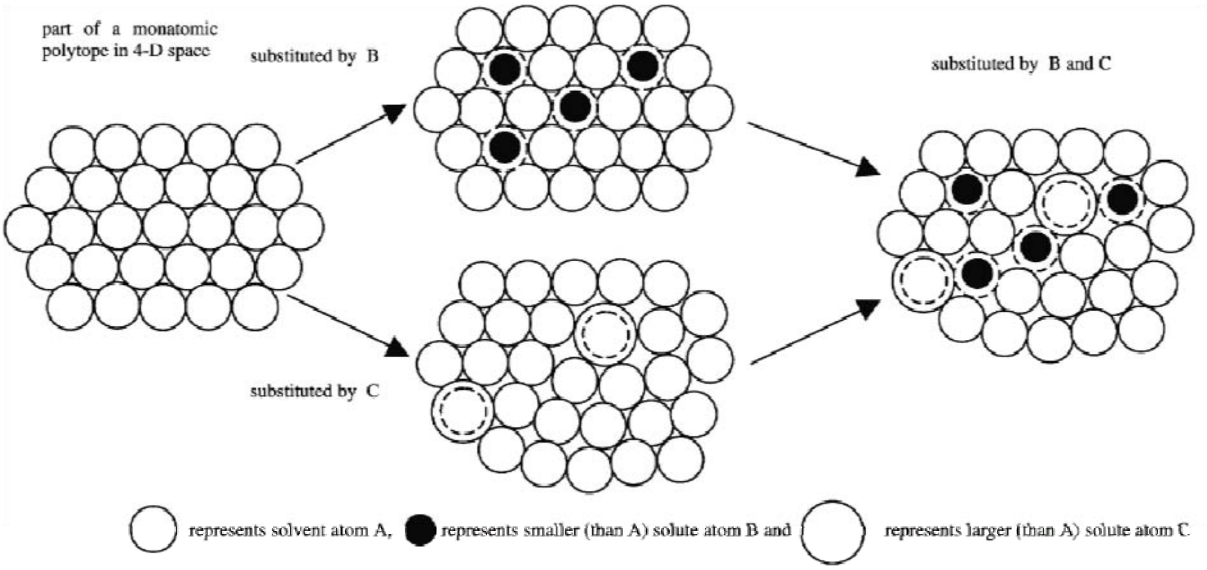

Figure 2.10 The atomic configuration of different atomic size systems [1].

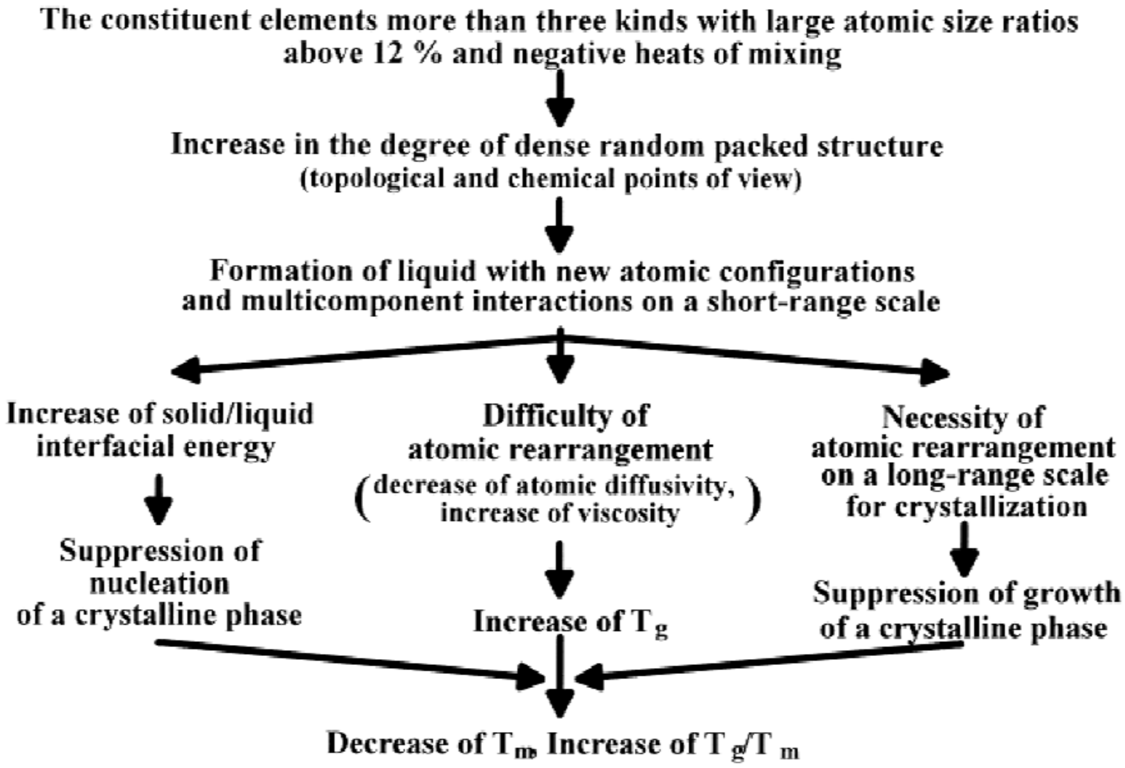

Figure 2.11 Mechanisms for the stabilization of supercooled liquid and high glass-forming ability for the multicomponent alloys which satisfy three empirical rules [1].

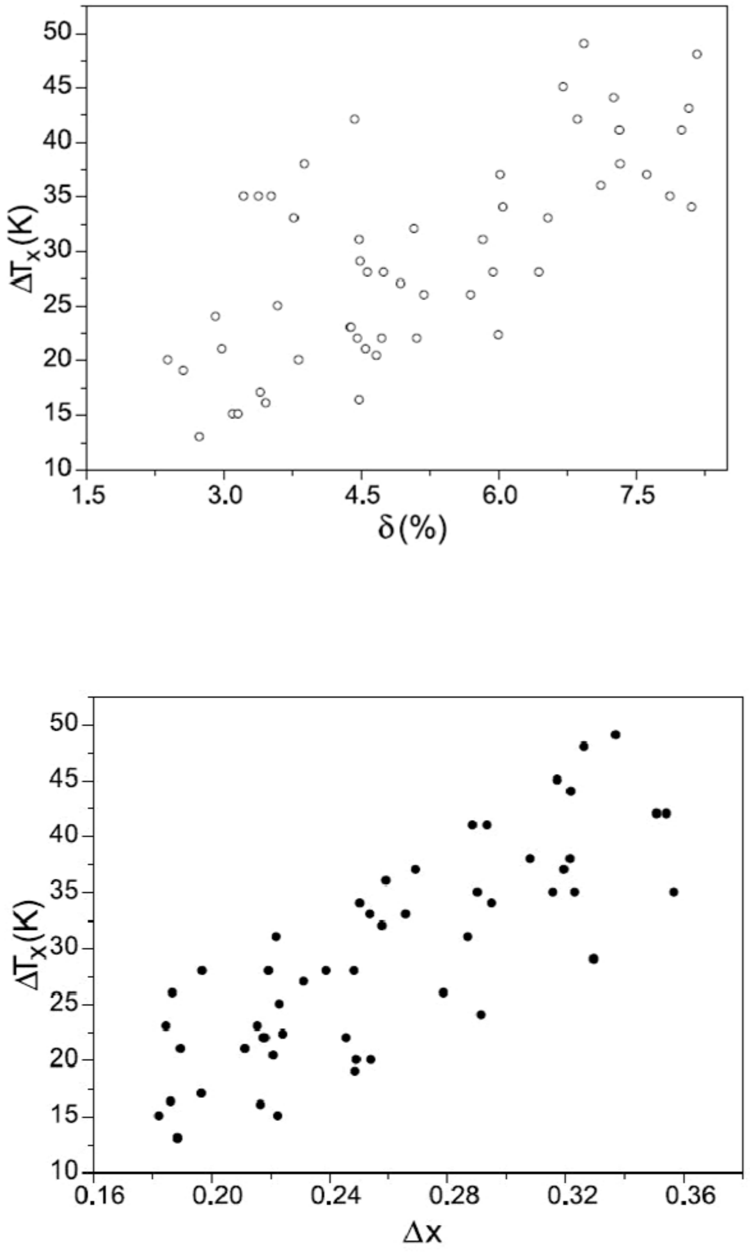

Figure 2.12 The relationship between the bond parameters, including electronegativity difference (Δx) and atomic size parameters (δ), and the temperature interval of supercooled liquid region (ΔT_x) in Mg-Based bulk metallic glasses [79].

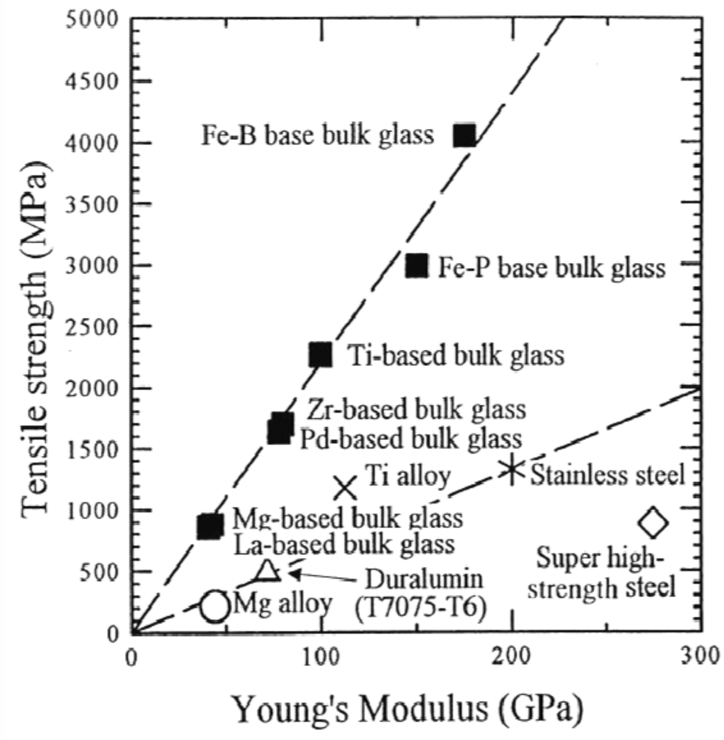

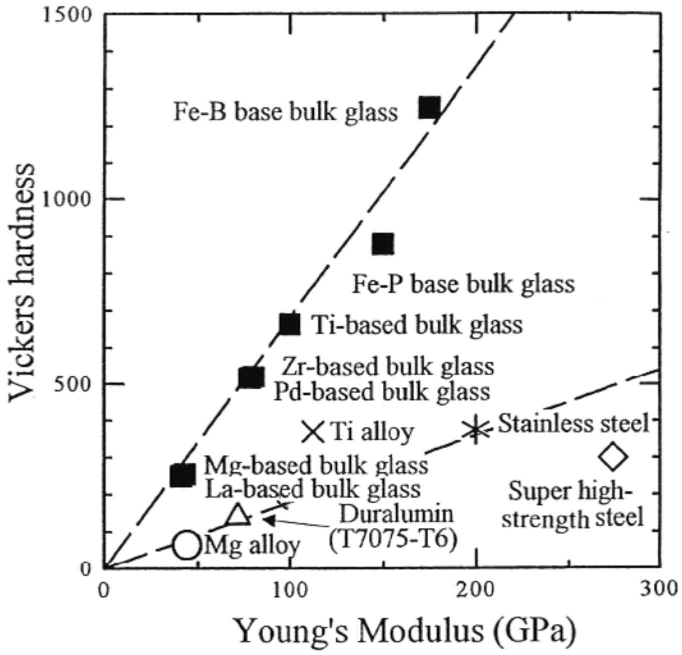

Figure 2.13 Relationship between tensile fracture strength, Vickers hardness and Young's modulus for bulk amorphous alloys and conventional crystalline alloys [1].

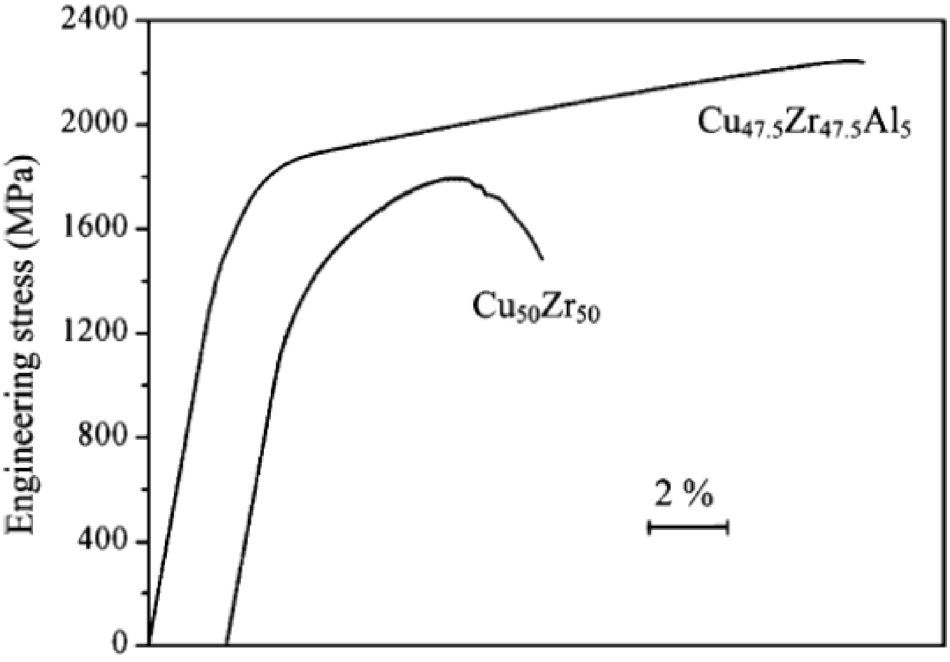

Figure 2.14 Stress–strain curves of $Cu_{50}Zr_{50}$ and $Cu_{47.5}Zr_{47.5}Al_5$ under compression at a initial strain rate of 8×10^{-4} s^{-1} [38].

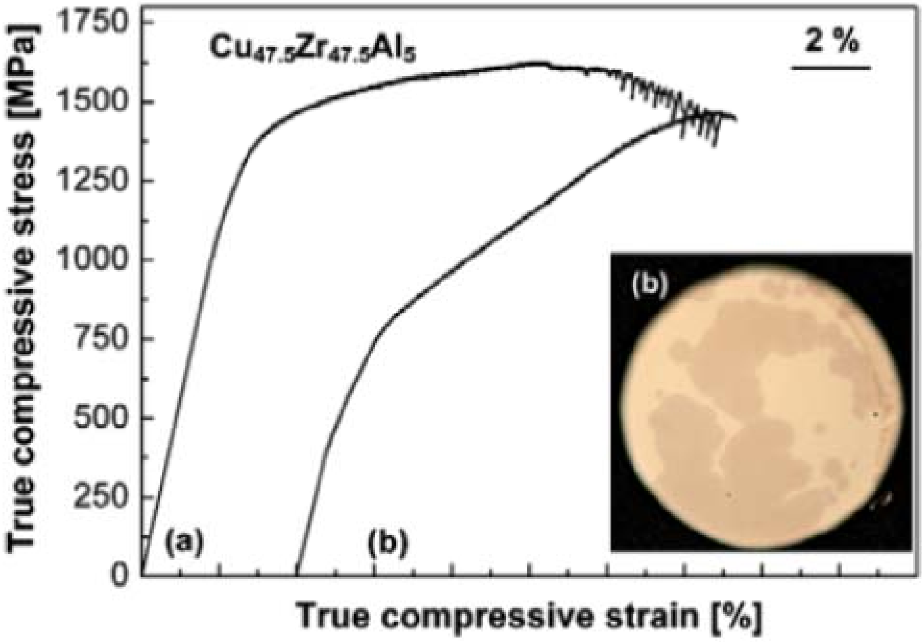

Figure 2.15 True stress–strain curves of $Cu_{47.5}Zr_{47.5}Al_5$ under compressive loading from (a) the bottom part of a rod and (b) the top part of the rod. With increase in the crystalline volume fraction (b) the work-hardening effect is much more pronounced. The inset shows the cross-section of the specimen taken from the top of the 2 mmdiameter rod. The darker phase consists of B2 crystals and the glassy phase appears brighter. [32]

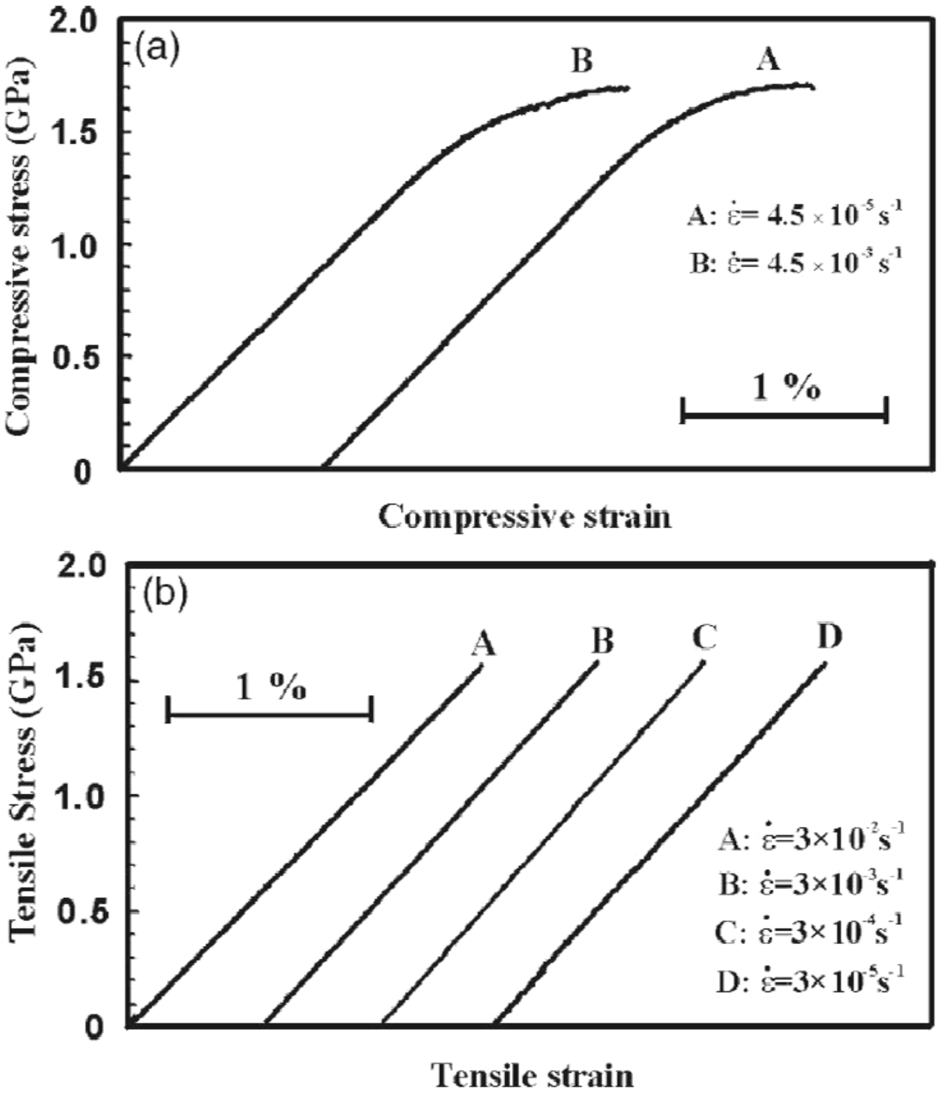

Figure 2.16 Typical (a) compressive and (b) tensile stress–strain curves of the $Zr_{59}Cu_{20}Al_{10}Ni_8Ti_3$ BMGs at different applied strain rates ranging from 4.5 x 10^{-5} to 3 x 10^{-2} s^{-1} [97].

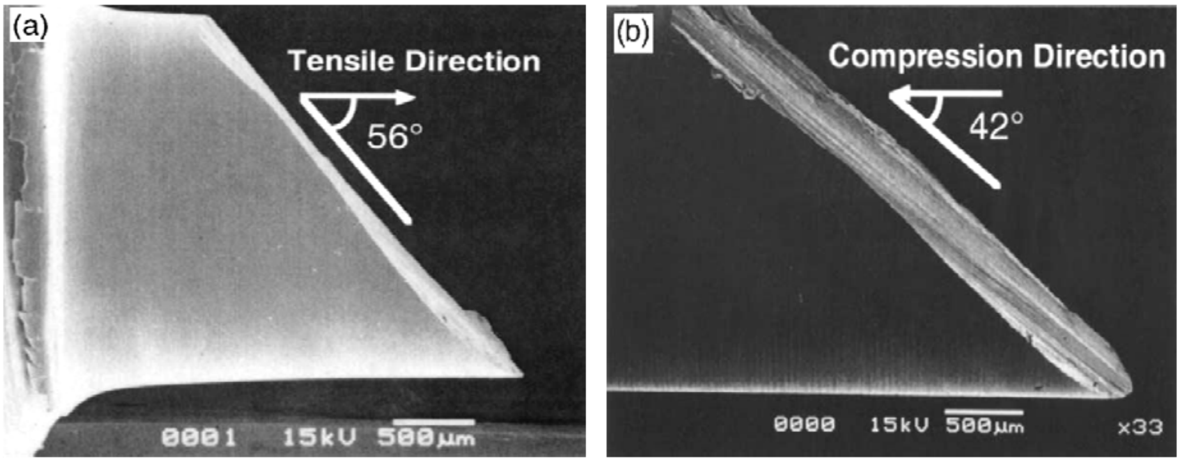

Figure 2.17 Typical side view of the $Pd_{40}Ni_{40}P_{20}$ BMGs with (a) tensile (θ_T) and (b) compressive (θ_c) fracture angle at a low strain rate [115].

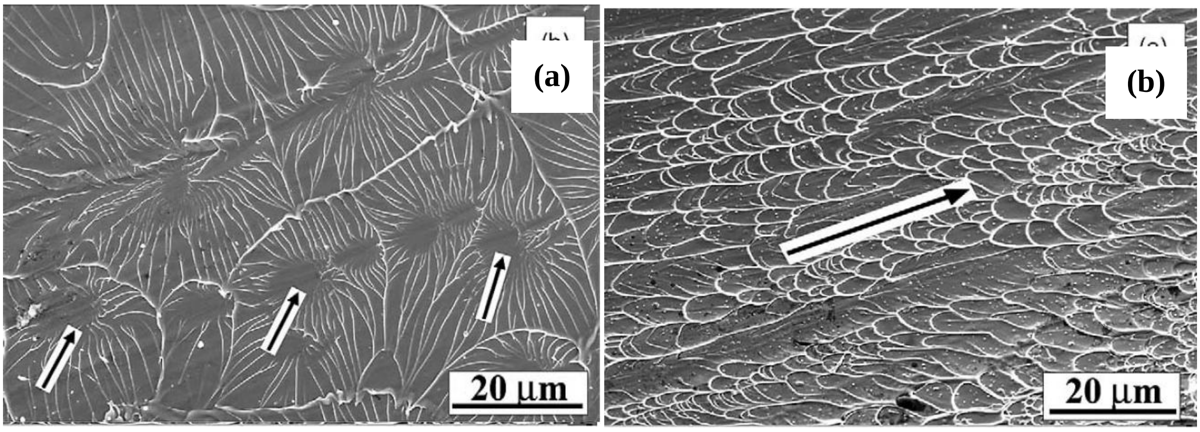

Figure 2.18 Typical fracture morphologies of the $Zr_{59}Cu_{20}Al_{10}Ni_8Ti_3$ BMGs with tensile and compressive fracture surfaces [97].

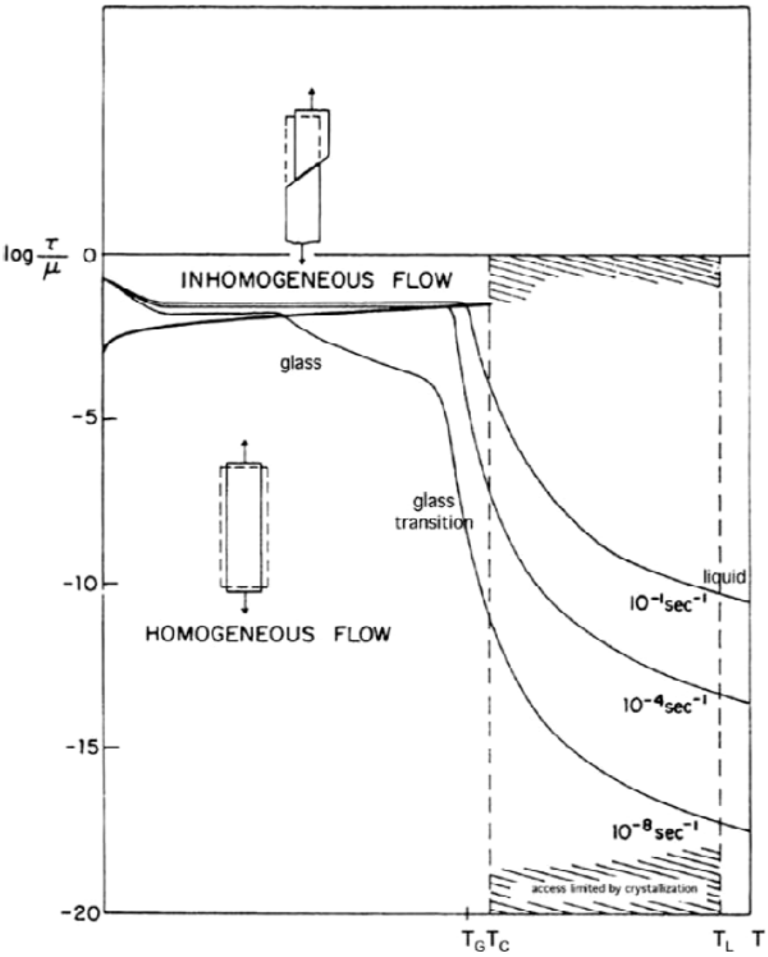

Figure 2.19 Schematic deformation mechanism map of a metallic glass [118].

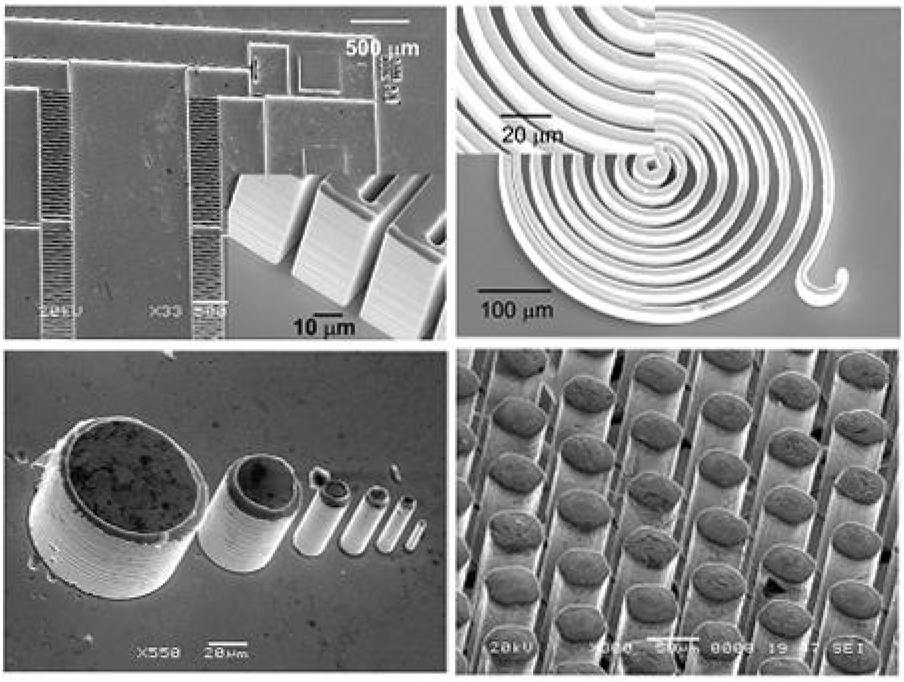

Figure 2.20 Device applied to the MEMS for BMGs [119].

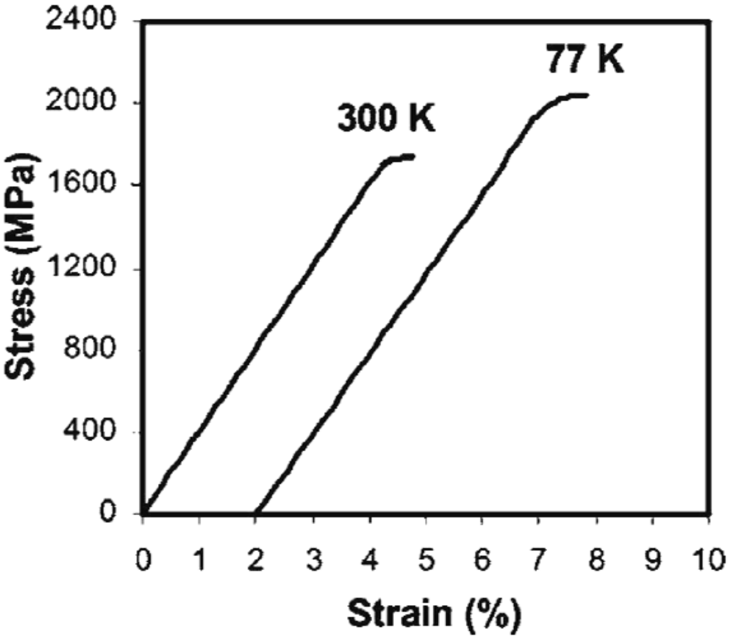

Figure 2.21 Compressive stress-strain curves of the Zr-based BMG at room temperature (300 K) and liquid nitrogen temperature (77 K) at a strain rate of $2x10^{-4}$ s^{-1} [121].

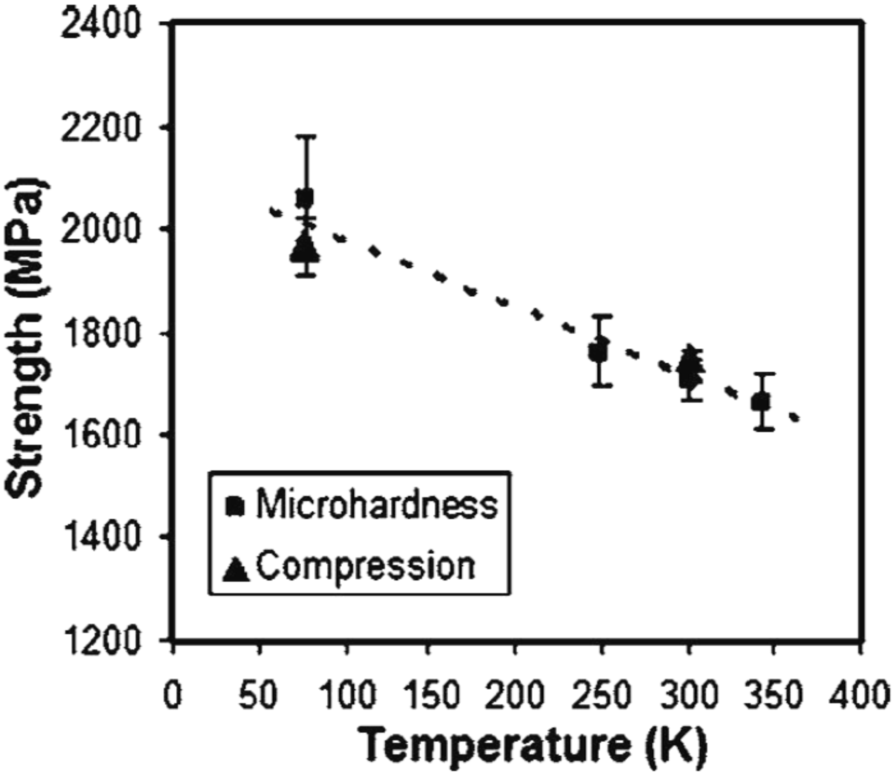

Figure 2.22 Dependence of strength variation as a function of testing temperatures in compression and microhardness [121].

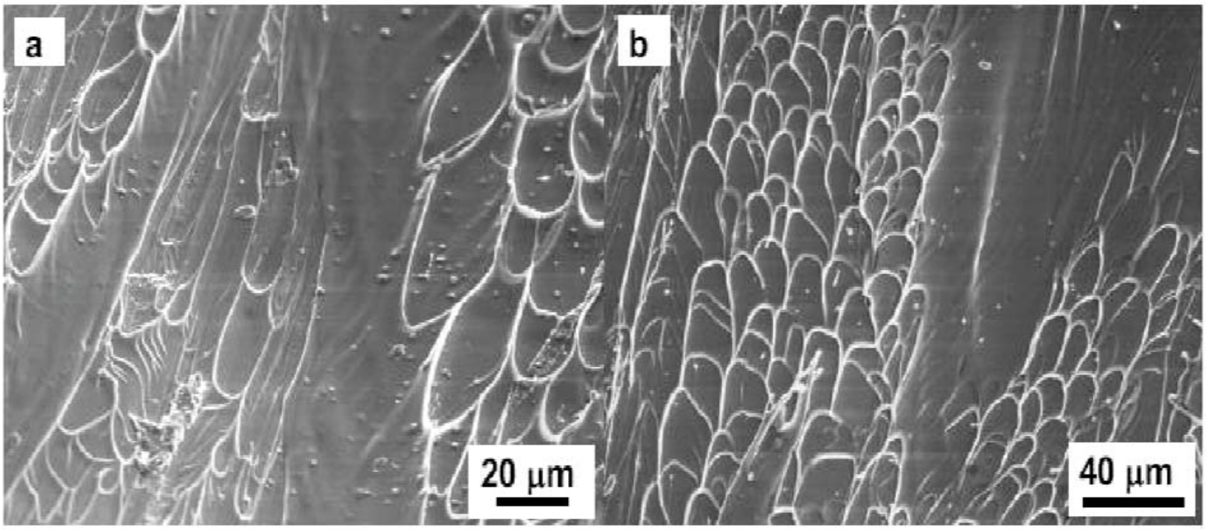

Figure 2.23 SEM micrographs of fracture surfaces of BMG samples tested at (a) 300 K and (b) 77 K under compression tests [122].

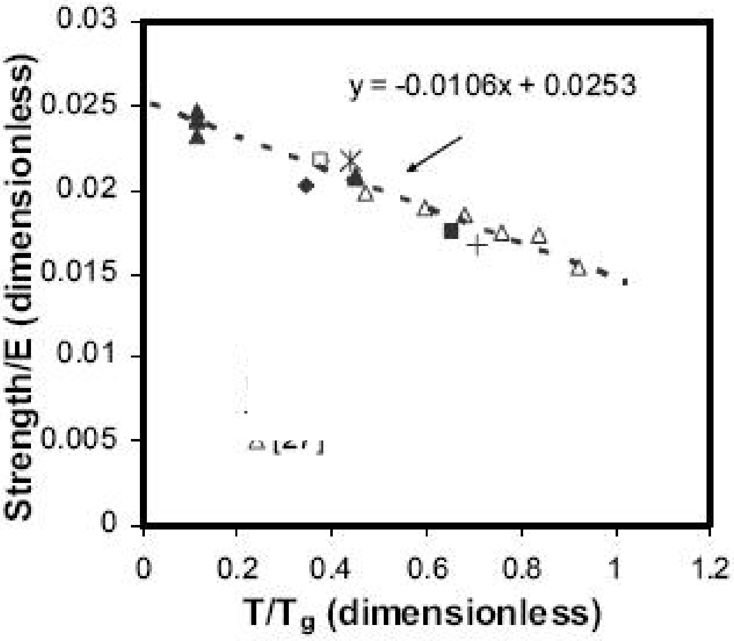

Figure 2.24 Dependence of the normalized strength as a function of the normalized temperature for the BMGs deformed under compression tests [122].

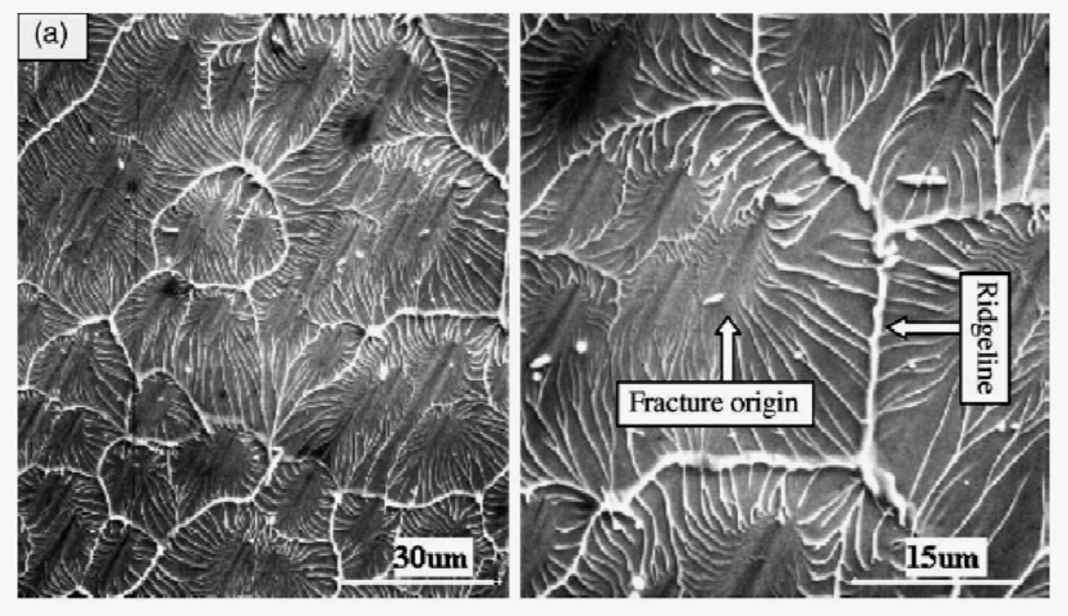

Figure 2.25 Fracture surface morphologies of the $Zr_{52.5}Al_{10}$Ni10$Cu_{15}Be_{12.5}$ BMG at low strain rates under the tensile deformation [125].

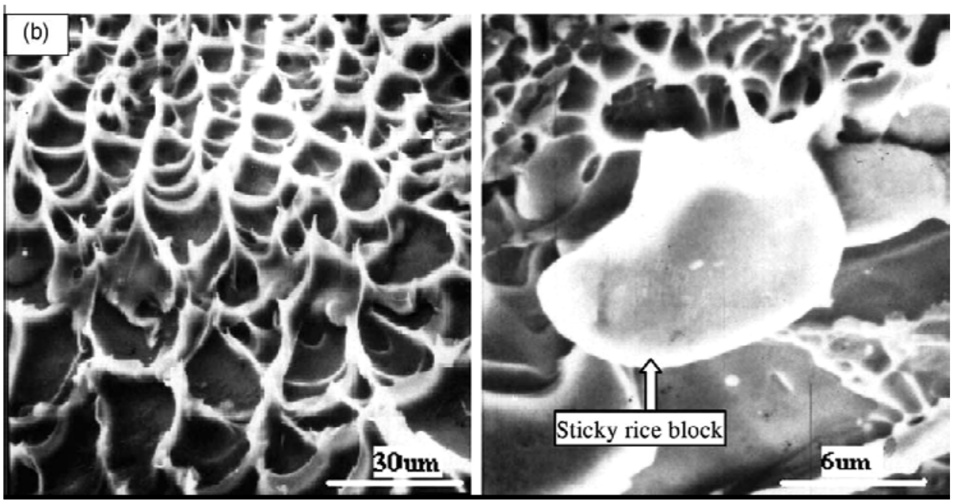

Figure 2.26 Fracture surface morphologies of the $Zr_{52.5}Al_{10}$Ni10$Cu_{15}Be_{12.5}$ BMG at high strain rates under the tensile deformation [125].

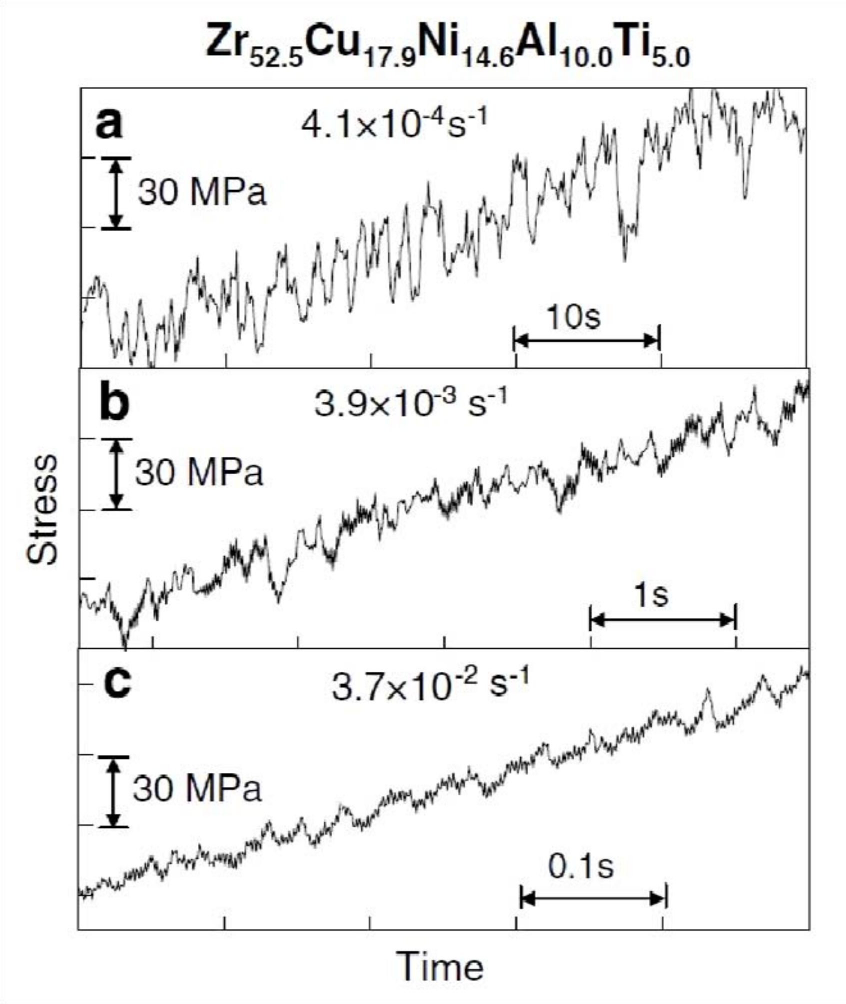

Figure 2.27 Stress as a function of time of of Zr-based BMGs at various applied strain rates of (a) 4.1 x 10^{-4} s^{-1}, (b) 3.9 x 10^{-3} s^{-1} and (c) 3.7 x 10^{-2} s^{-1} [127].

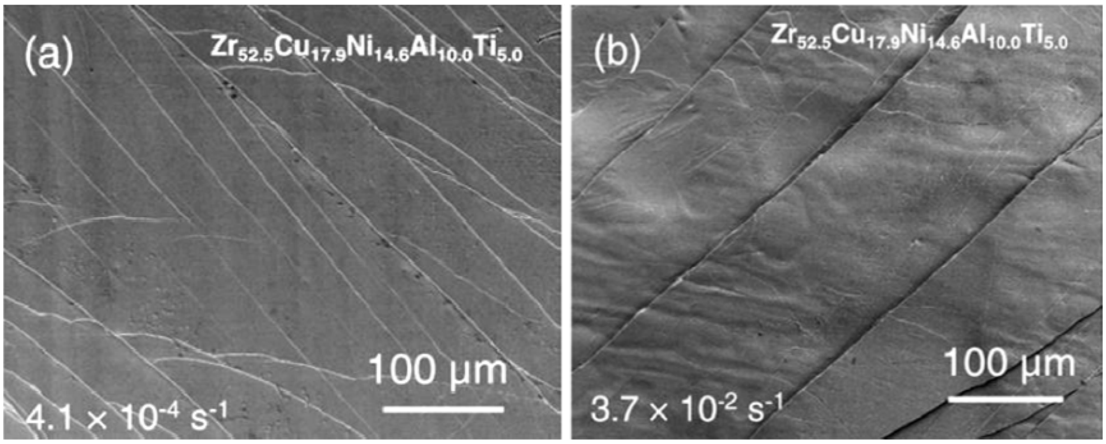

Figure 2.28 SEM micrographs of sample outer appearances of Zr-based BMG tested to a plastic strain of 26.4% at the strain rates of (a) 4.1 x 10^{-4} s^{-1} and 3.7 x 10^{-2} s^{-1} [127].

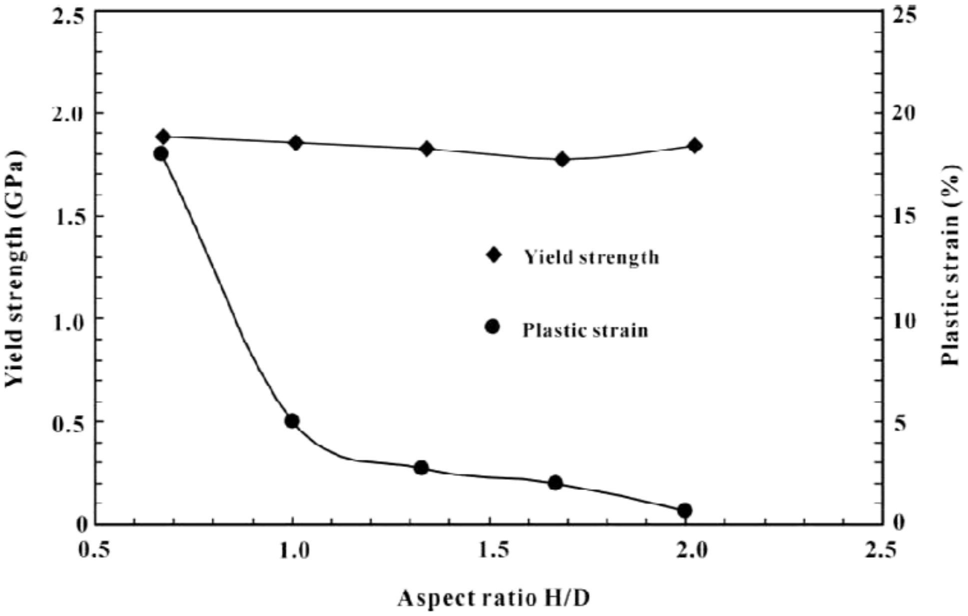

Figure 2.29 Dependence of yield strength and plastic strain on the aspect ratio of the $Zr_{59}Cu_{20}Al_{10}Ni_8Ti_3$ BMGs in compression [92].

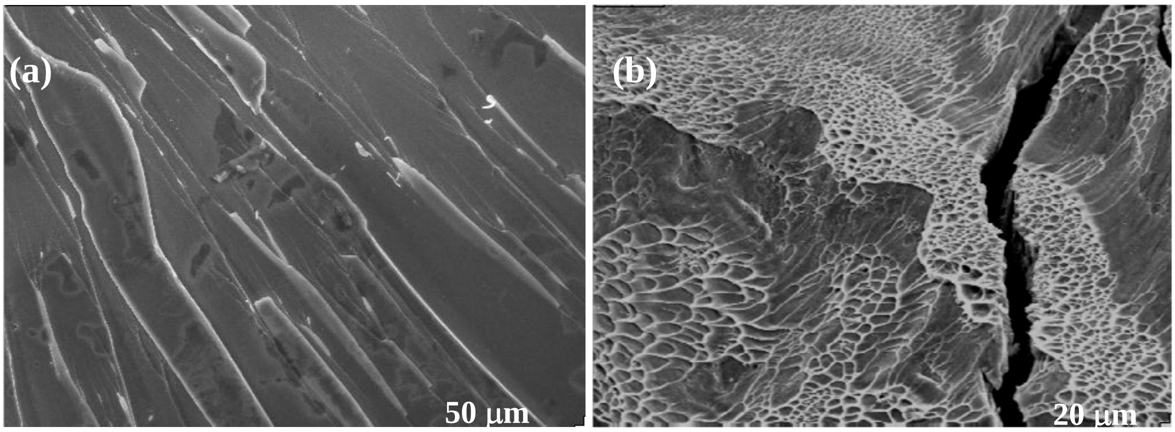

Figure 2.30 Fracture surfaces of the cylindrical $Mg_{65}Cu_{25}Gd_{10}$ samples with the aspect ratio of (a) 2 and (b) 0.25 in compression [95].

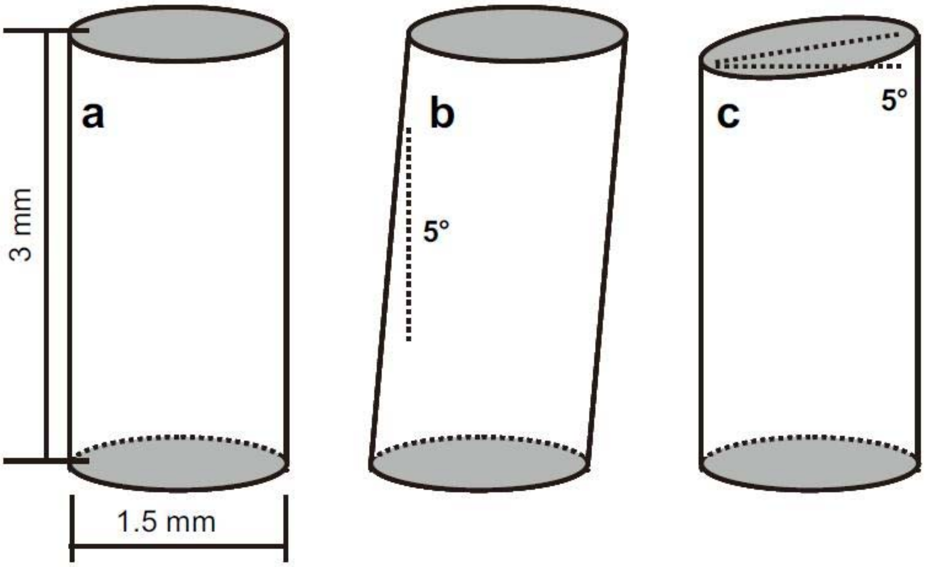

Figure 2.31 BMG samples with three various designed geometries (a) orthogonal, (b) monoclinic and (c) transitional [139].

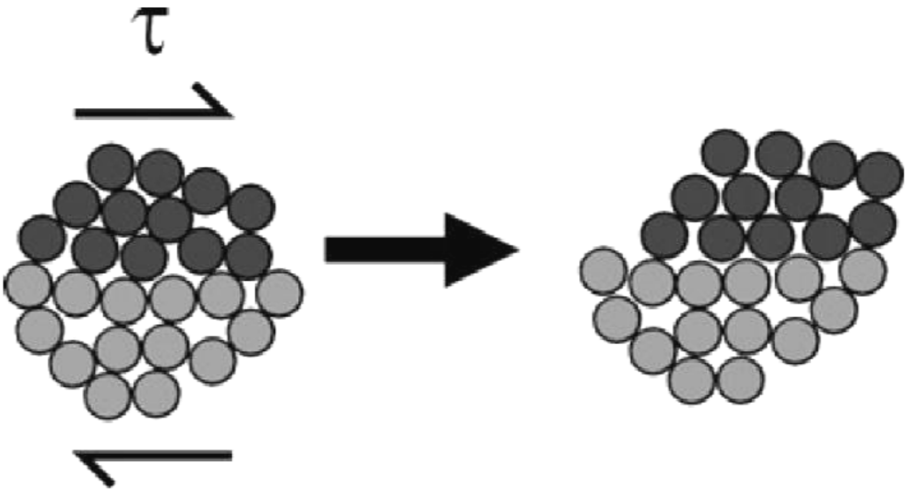

Figure 2.32 Two-dimensional schematic diagram of atomistic deformation mechanism for metallic glasses under applied loading [10].

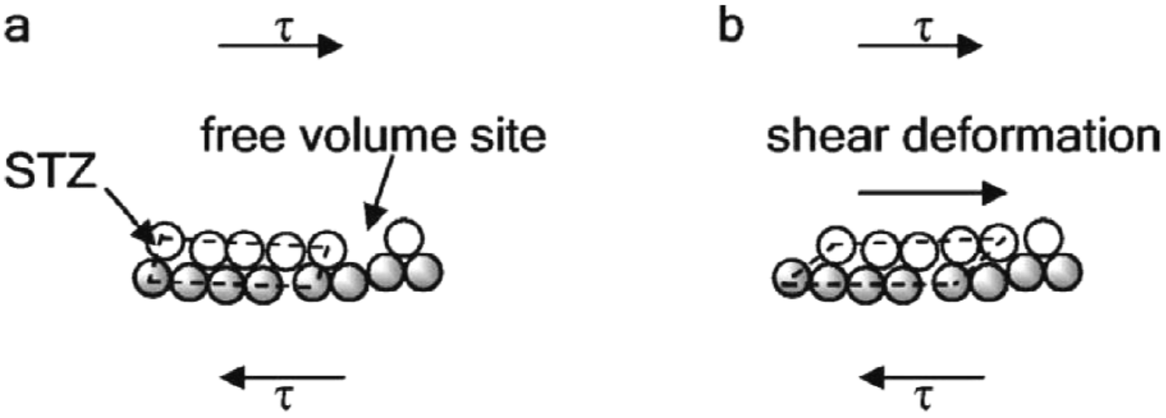

Figure 2.33 Simplified illustration of STZ deformation. (a) STZ before shear deformation and (b) STZ after shear deformation [146].

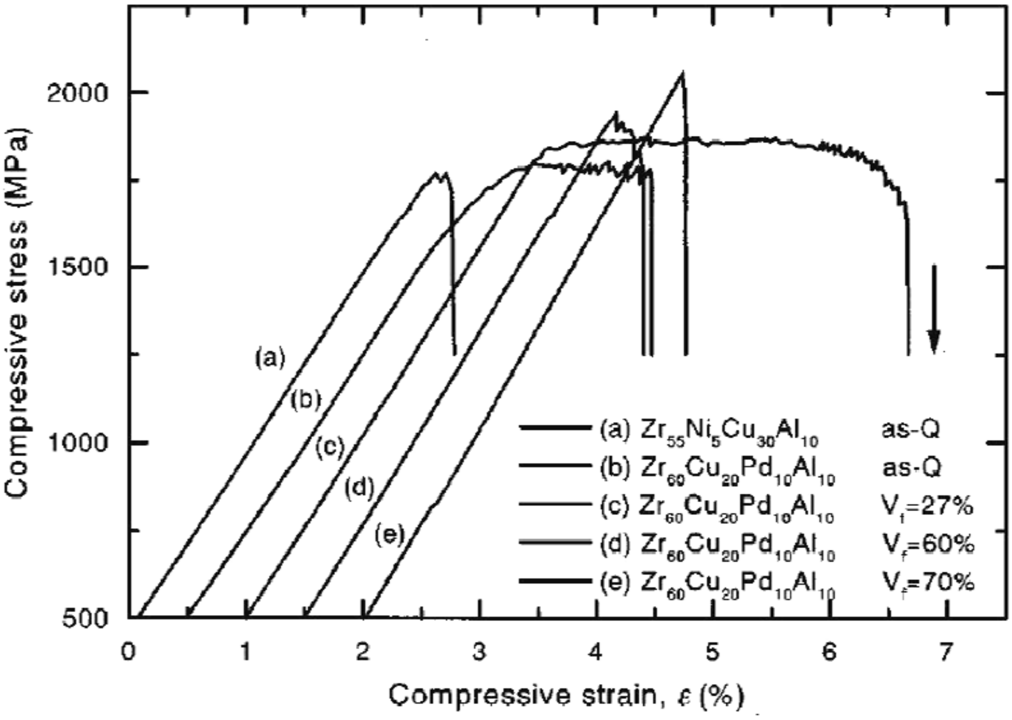

Figure 2.34 Compressive stress-strain curves of the $Zr_{60}Al_{10}Cu_{20}Pd_{10}$ BMG and BMGCs with various volume fraction of Zr_2(Cu, Pd) precipitated nanocrystals [65].

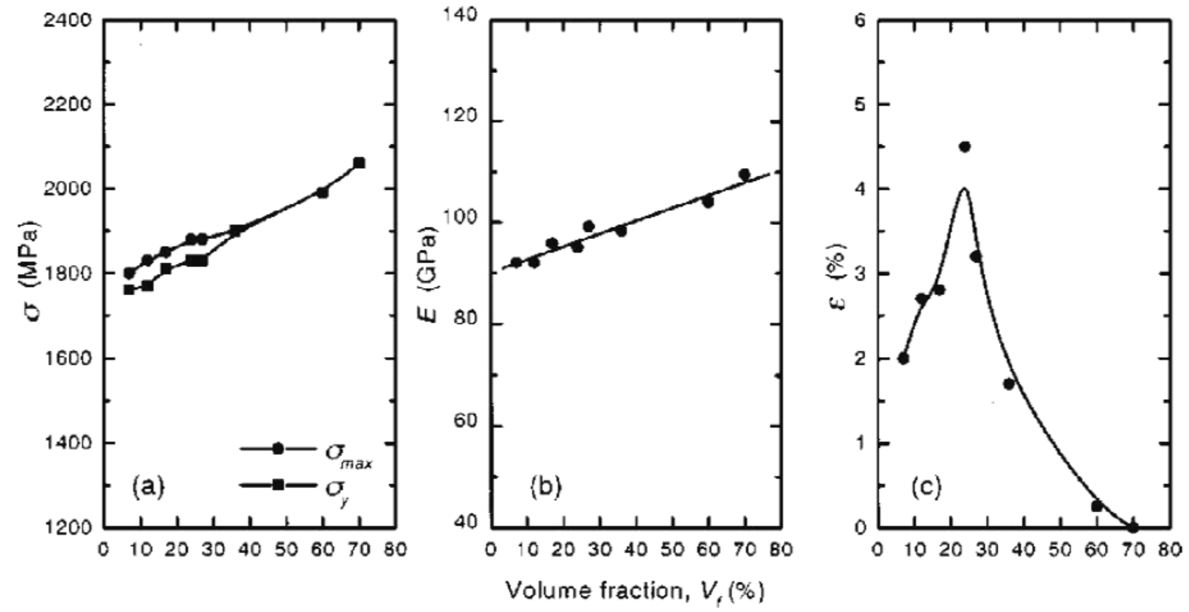

Figure 2.35 Mechanical properties of the $Zr_{60}Al_{10}Cu_{20}Pd_{10}$ BMG and BMGCs with various volume fraction of Zr_2(Cu, Pd) precipitated nanocrystals: (a) yield strength, σ_y, and the maximum fracture strength, σ_{max}; (b) Young's modulus, E and (c) plastic strain to failure after yielding, ε_p [65].

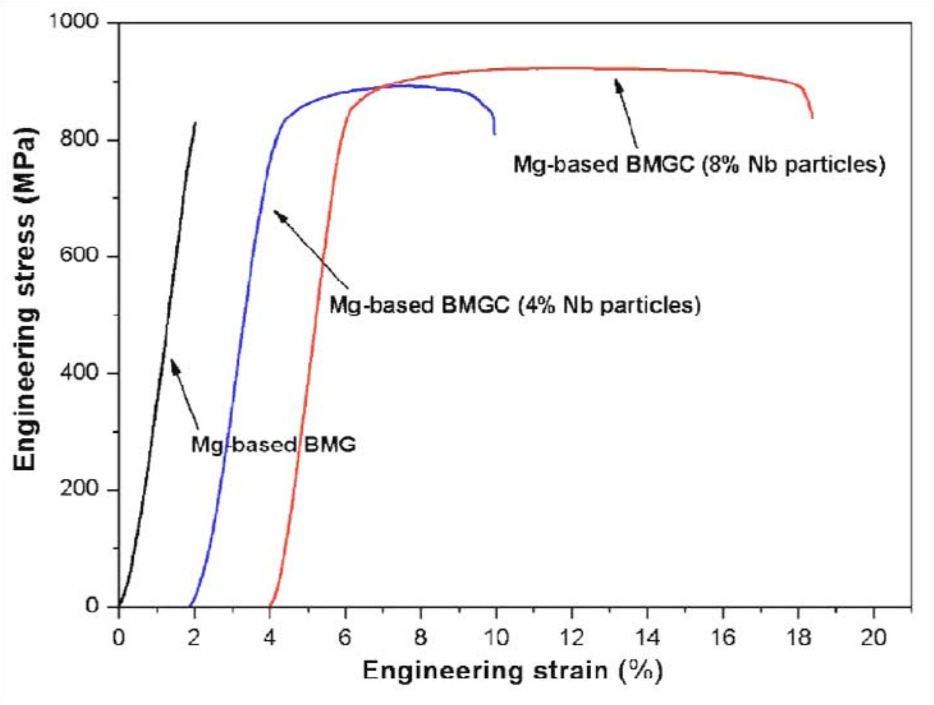

Figure 2.36 Compressive stress-strain curves for the monolithic Mg-based BMG and Nb-containing Mg-based BMGC with volume fraction of 4% and 8%, respectively [165].

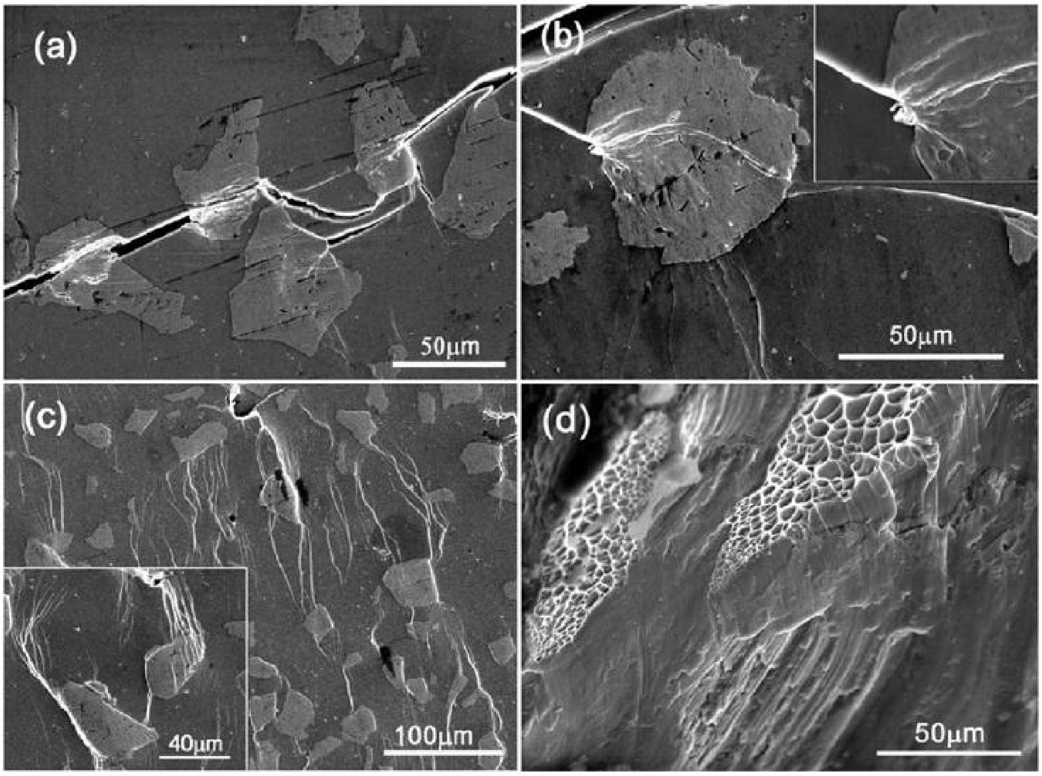

Figure 2.37 SEM micrographs of (a) outer surface and (d) fracture surface for the Mg-based BMGC. The inset in (b) shows the enlarged view of the interface where a shear band travels into a particle; the inset in (c) shows the shear bands propagation and branching from deformed Nb particles [165].

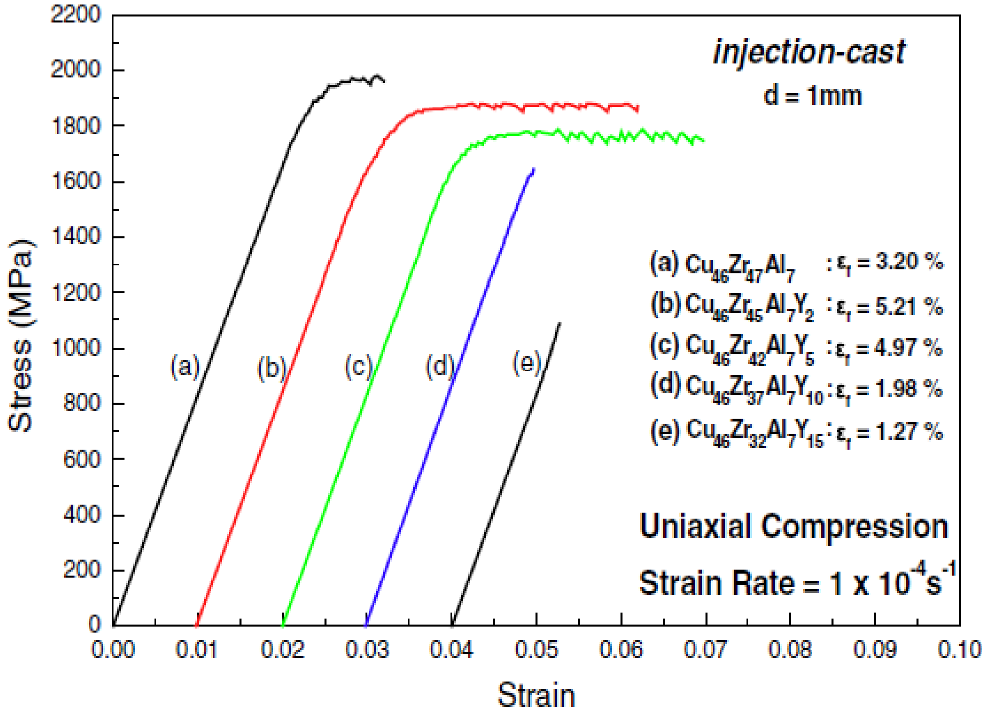

Figure 2.38 Stress-strain curves obtained from the uniaxial compression test of $Cu_{46}Zr_{47-x}Y_xAl_7$ (x = 0, 2, 5, 10, 15) rod samples of 1 mm in diameter [23].

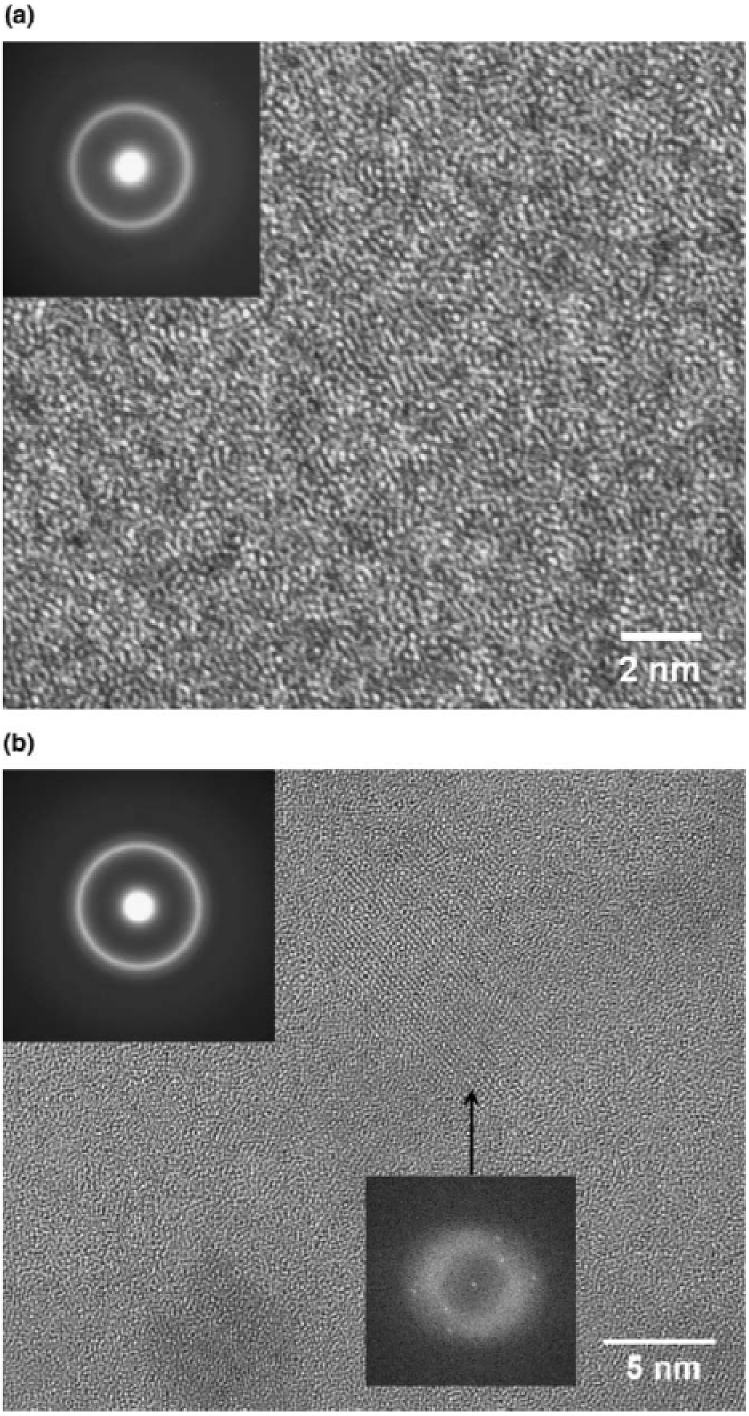

Figure 2.39 HRTEM images, SADPs, and diffraction pattern obtained from Fourier transform of HRTEM images for: (a) as-cast BMG rod sample with x = 5 (1 mm diameter) and (b) BMG rod sample with x = 5 (1 mm diameter) heated to 753 K in the DSC experiment, shows the 5-7 nm nanocrystals embedded in the amorphous matrix [23].

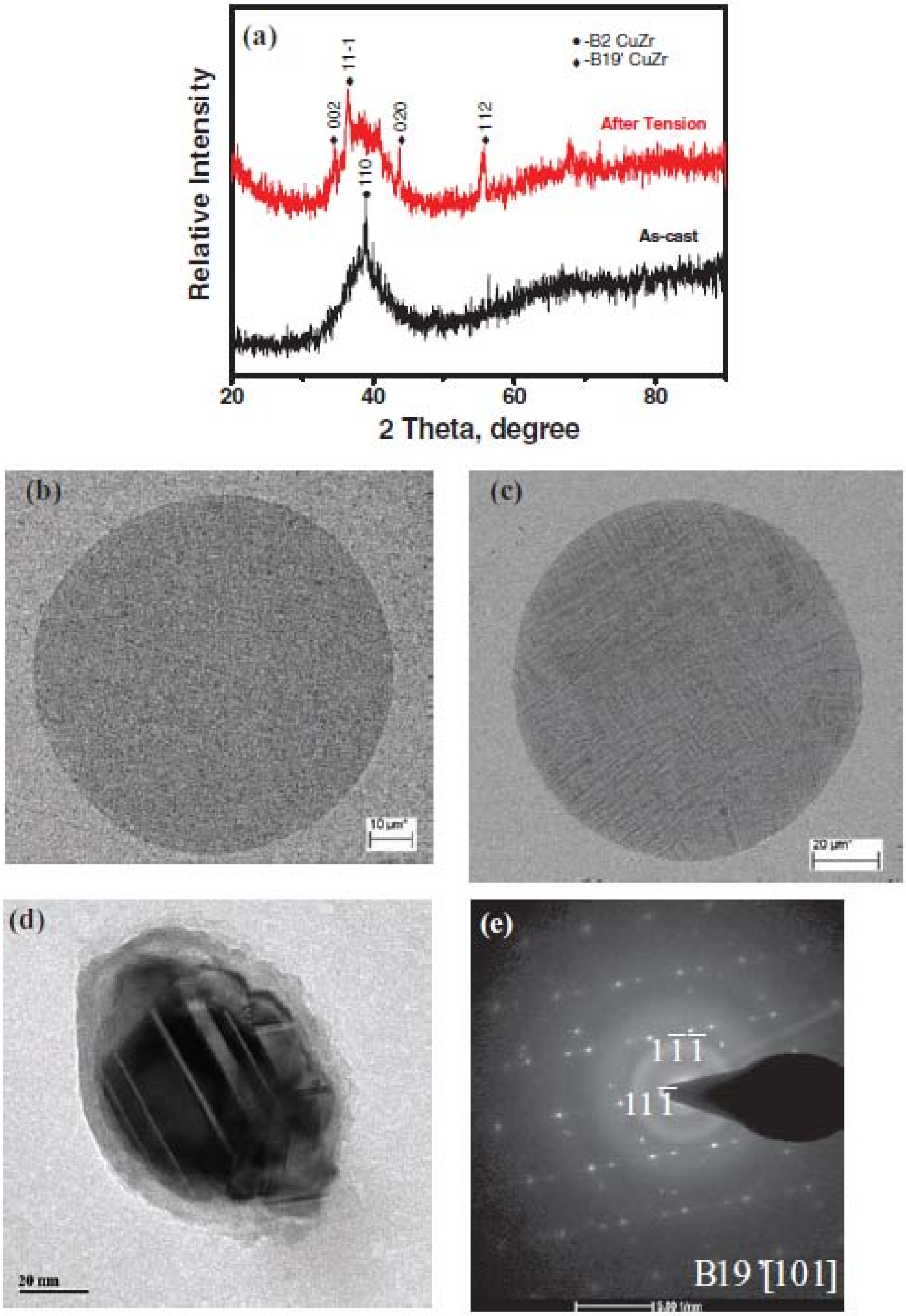

Figure 2.40 XRD patterns of the as-cast and fractured samples (a) Morphology of the crystalline phase (b) before and (c) after tensile testing. (d) TEM image of the small crystalline phase after tension and (e) an SAED pattern of a transformed crystalline phase [33].

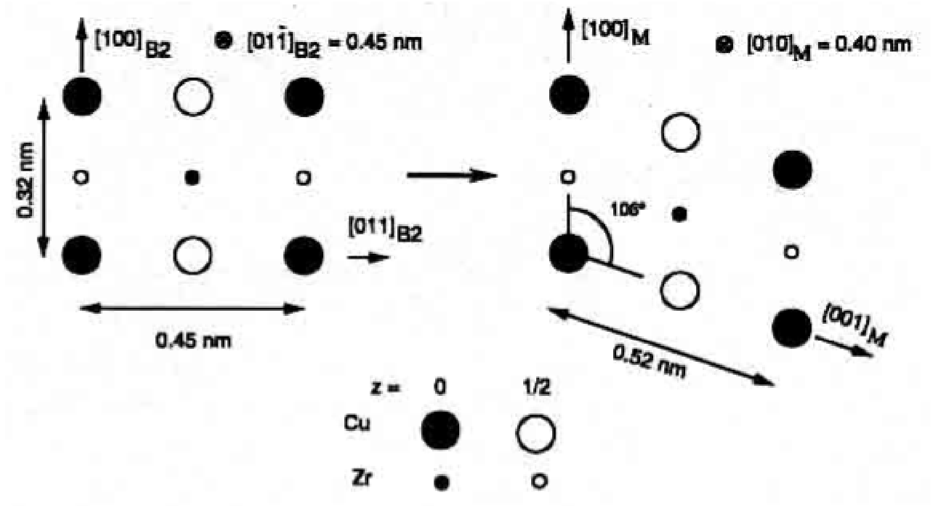

Figure 2.41 Schematic of the distortions transforming the CuZr B2 into the B19’ structure [176].

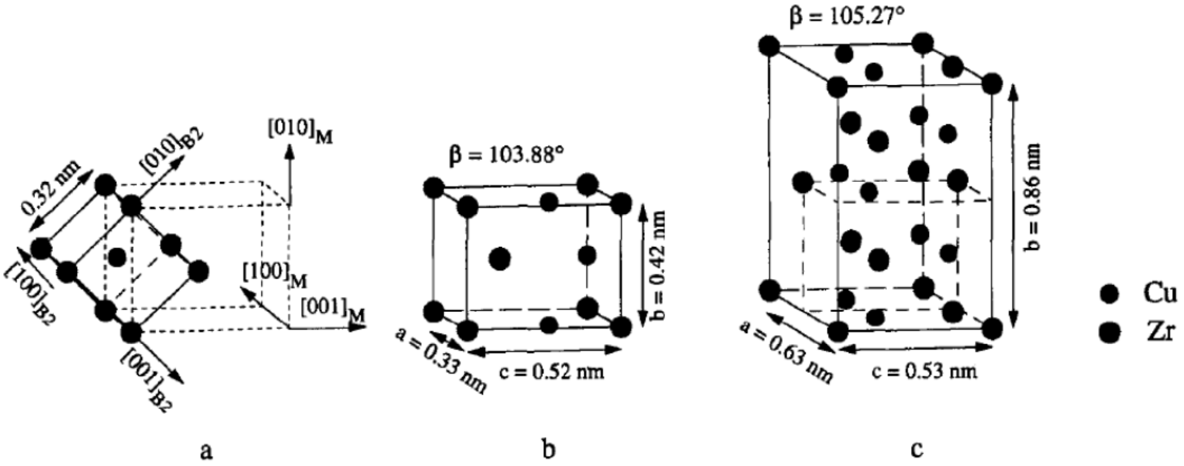

Figure 2.42 Schematics of (a) the B2 austenite, (b) the basic and (c) superstructure martensite including the suggested crystallographic relation [175].

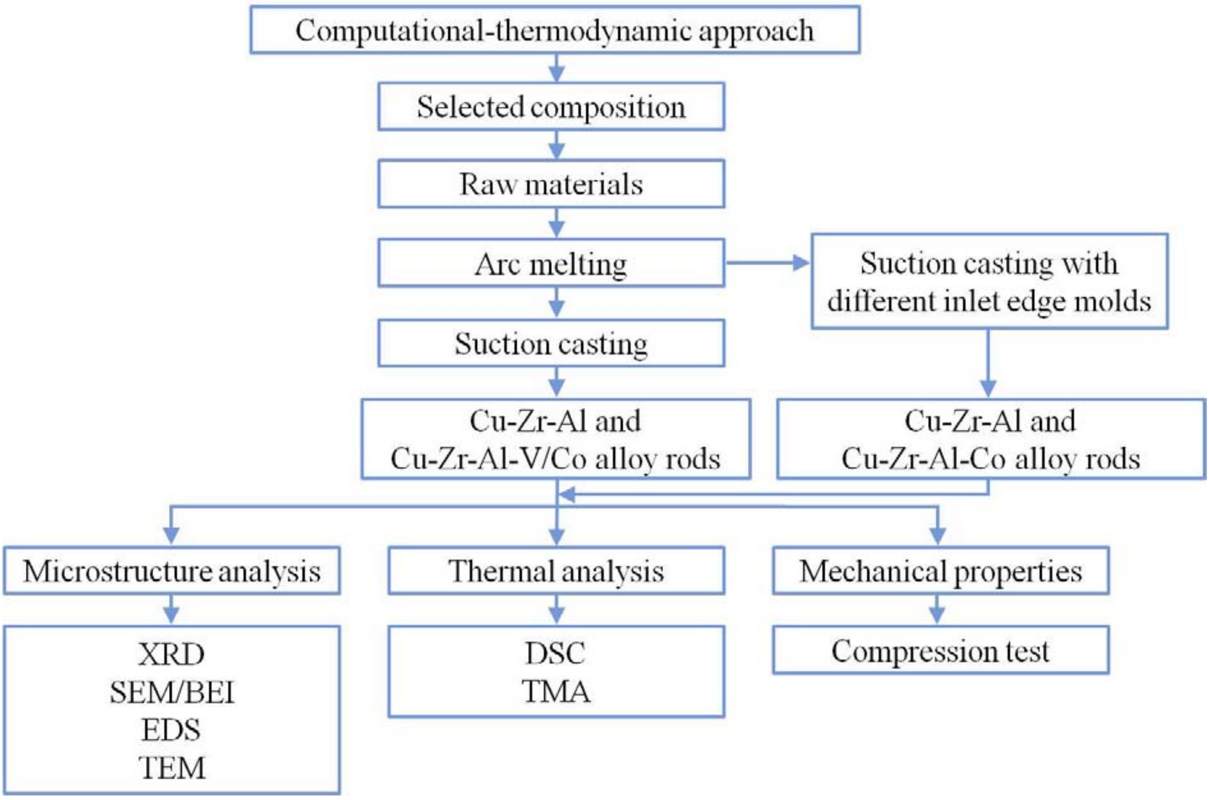

Figure 3.1 The flow chart of experimental procedures.

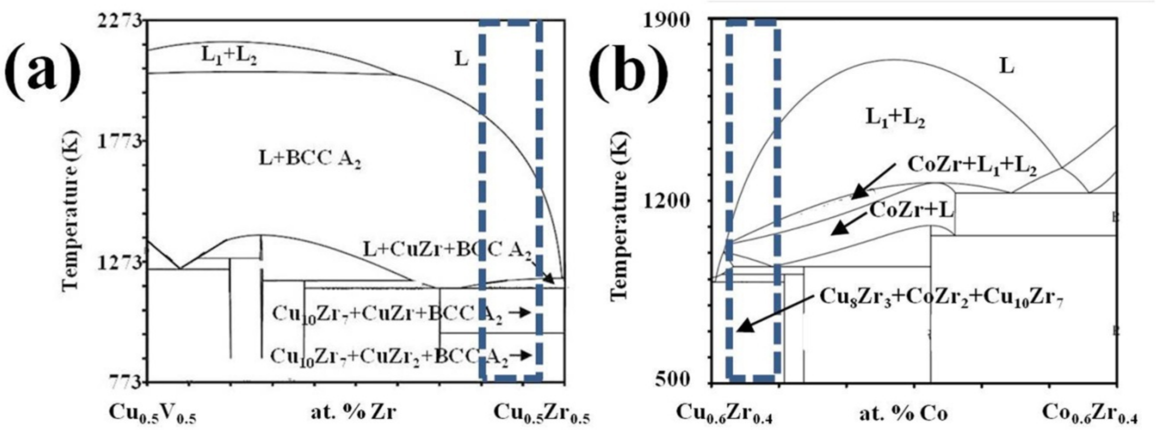

Figure 3.2 The vertical section of (a) the Cu-Zr-V alloy system at 50 at% Cu, and (b) the Cu-Zr-Co alloy system at 40 at% Zr. The selected composition range in this study is indicated by the frame. (c) XRD curves for the alloys with V and Co contents from 0 to 10 at%.

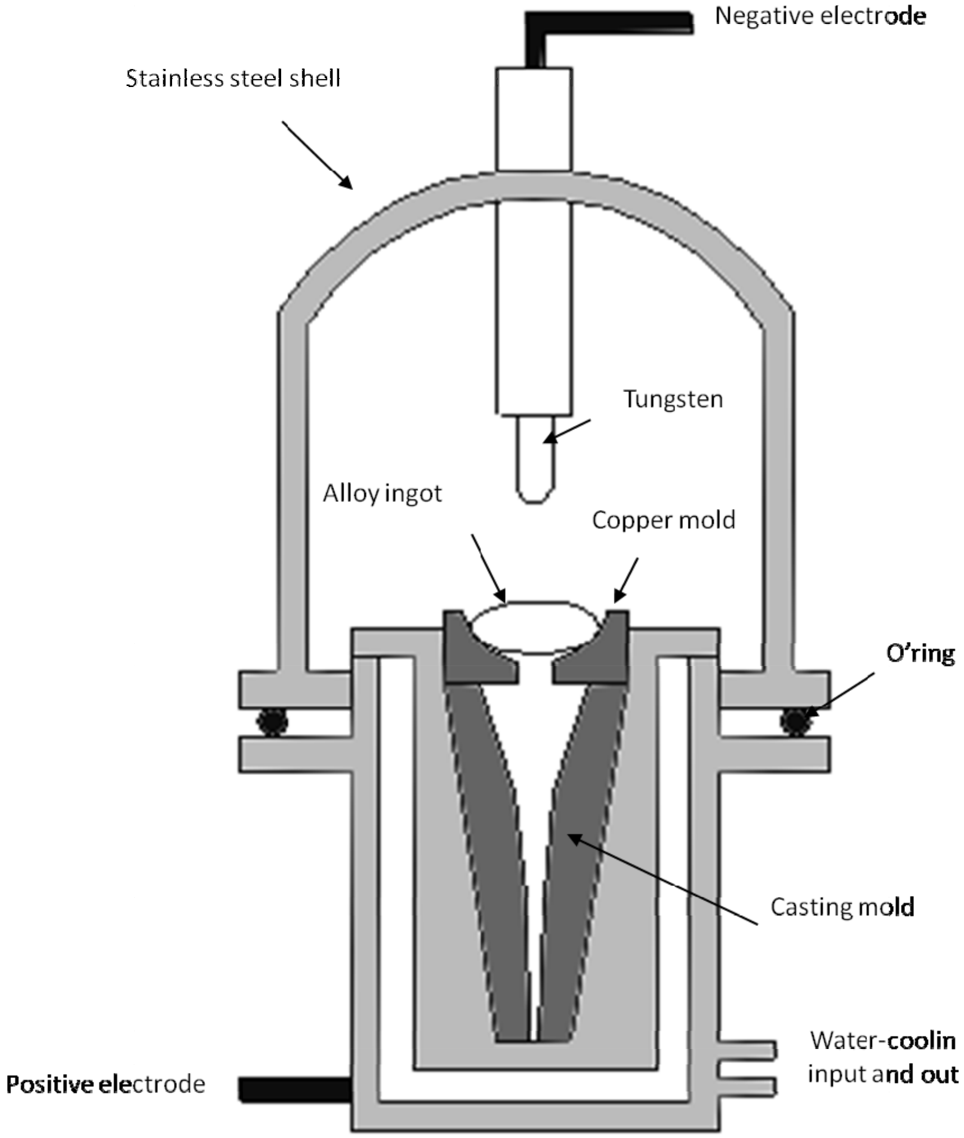

Figure 3.3 Illustration of an arc melting and suction casting furnace.

Figure 3.4 Illustration of mini-suction casting machine.

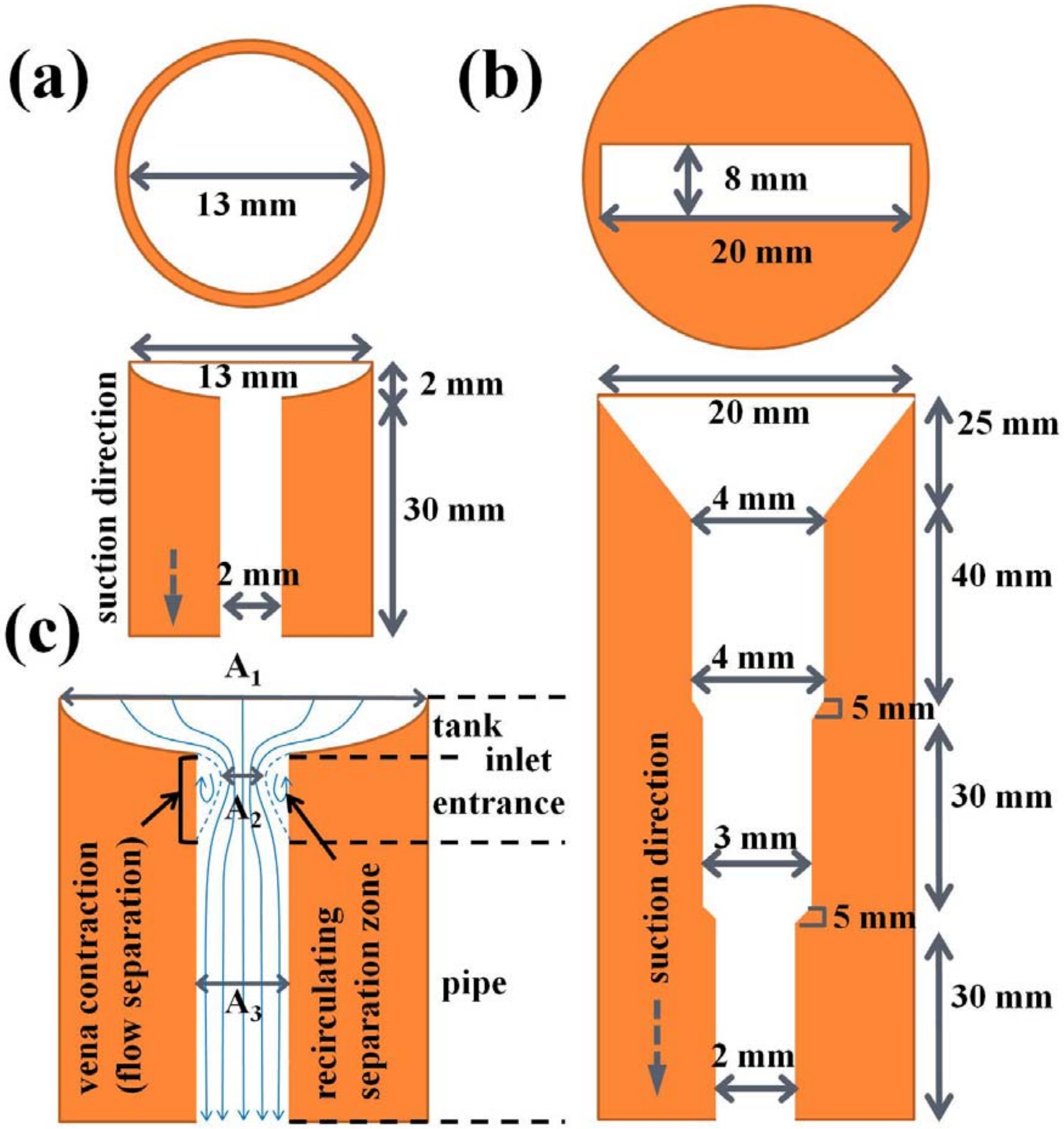

Figure 3.5 Schematic drawings of the two suction cast furnaces with different inlet edges from the tank to the pipe and different area-reduction rates: (a) the sharp (S) mold with the inlet suddenly shrunk from 13 mm to 2 mm in diameter, and (b) the blunt (B) mold with the inlet gradually narrowed from 20 to 4, 3 and 2 mm in three steps. (c) The vena contraction caused by the sudden inlet shrinking in the S mold.

Figure 3.6 Instron 5582 universal testing machine equipped with the linear variable differential transformer (LVDT) displacement transducer.

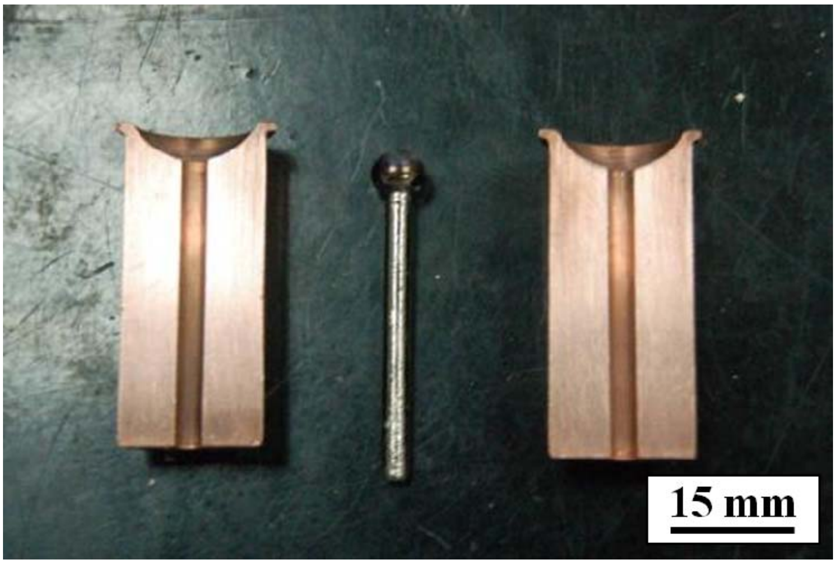

Figure 4.1 The appearance of the $Cu_{50}Zr_{43}Al_7$ alloy rod.

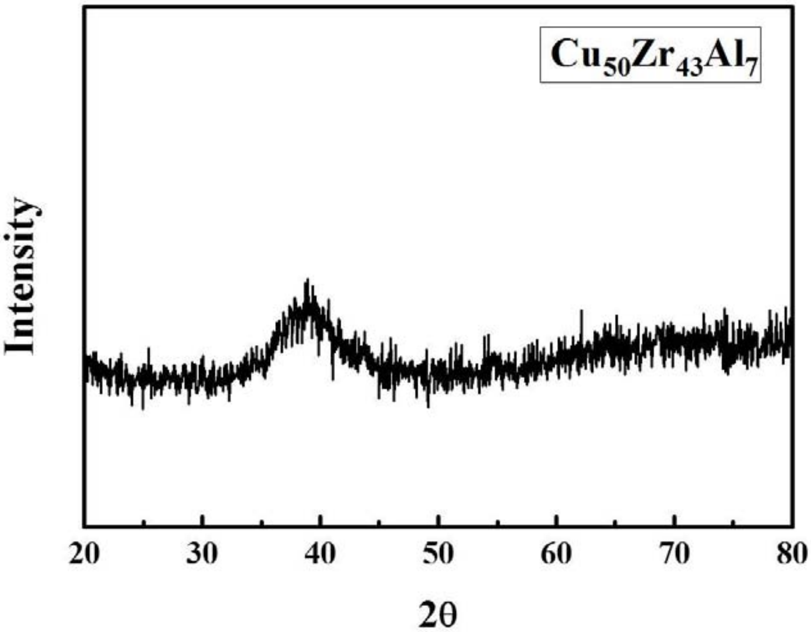

Figure 4.2 The XRD pattern of the as-cast $Cu_{50}Zr_{43}Al_7$ alloy rod with 2 mm in diameter.

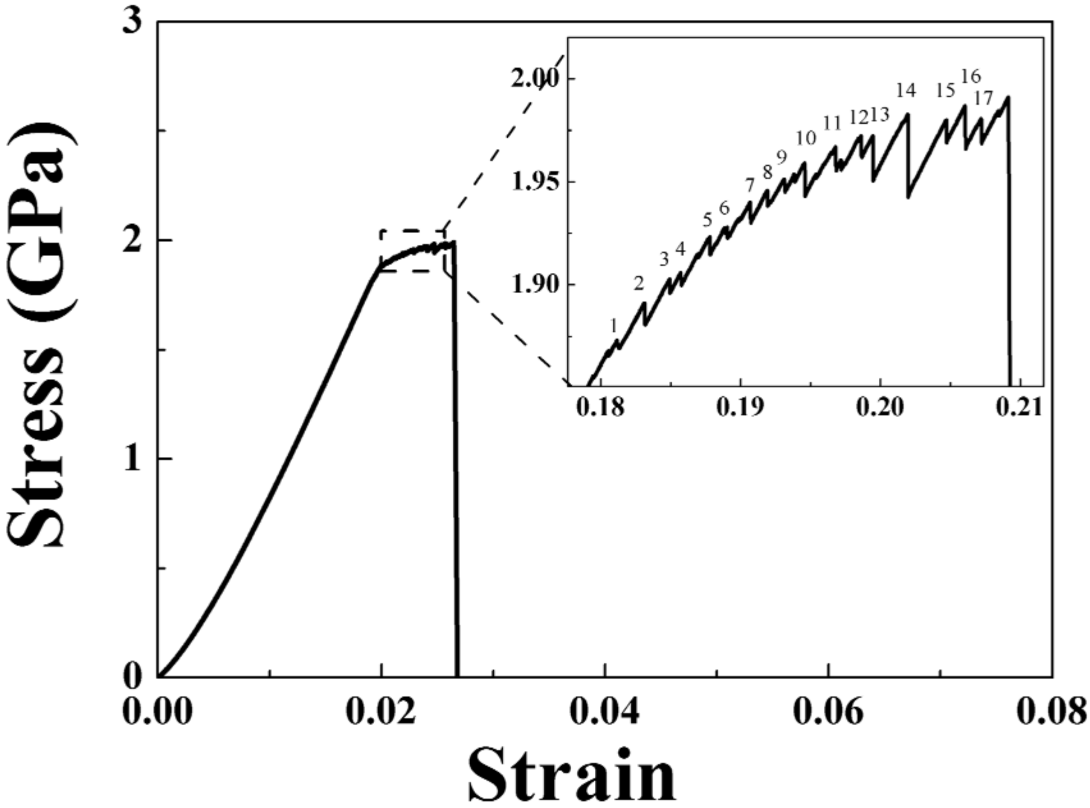

Figure 4.3 Typical engineering stress-strain curve for the $Cu_{50}Zr_{43}Al_7$ BMG at a normal strain rate of $1x10^{-4}$ s^{-1} in compression. The inset shows the enlarged view in the serrated region.

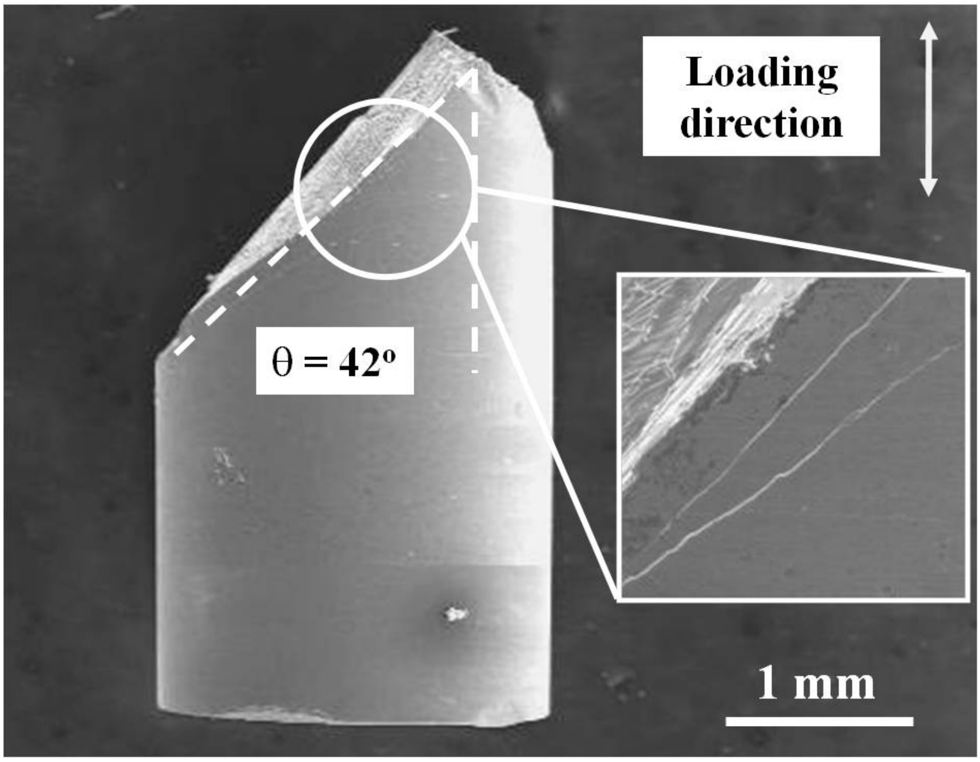

Figure 4.4 SEM observation on the side view of the deformed $Cu_{50}Zr_{43}Al_7$ BMG, showing a fracture angle and shear bands.

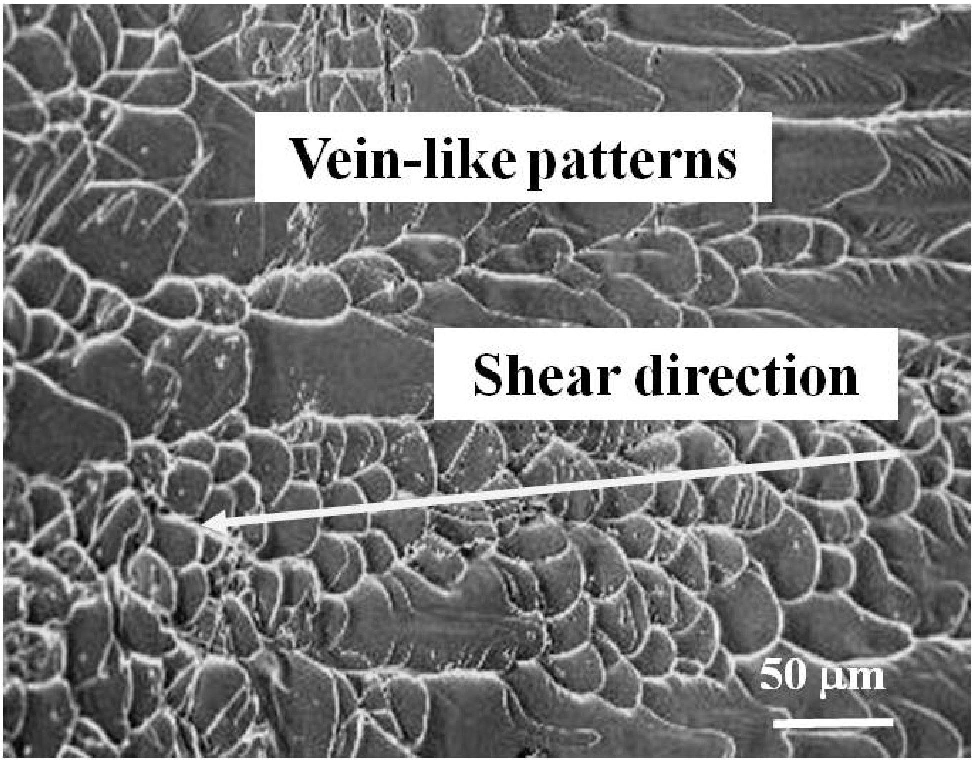

Figure 4.5 SEM observations on the fracture surface of the deformed $Cu_{50}Zr_{43}Al_7$ BMG, showing the vein-like patterns.

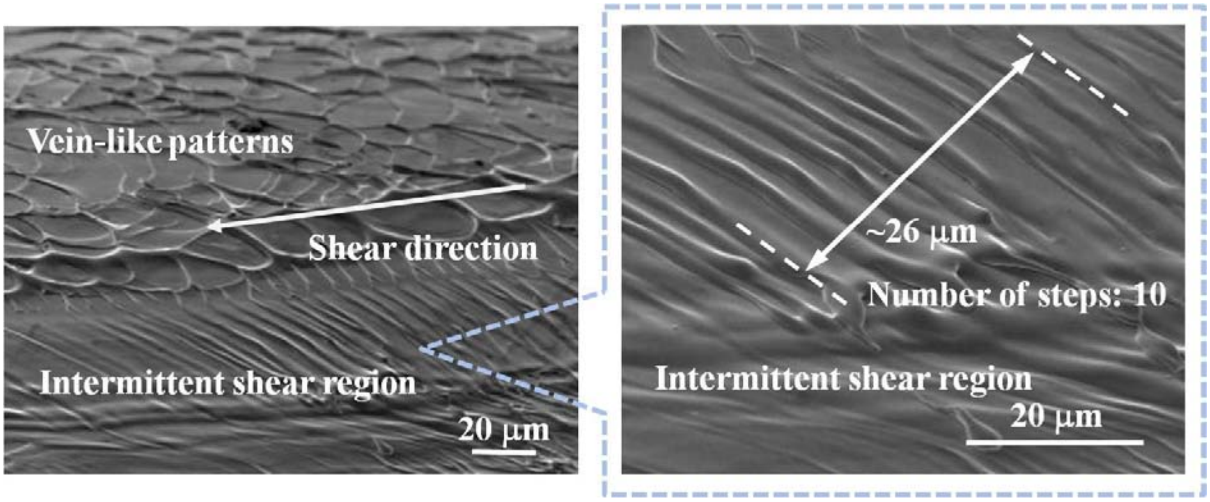

Figure 4.6 SEM observations on the fracture surface of the deformed $Cu_{50}Zr_{43}Al_7$ BMG, showing the intermittent shear region.

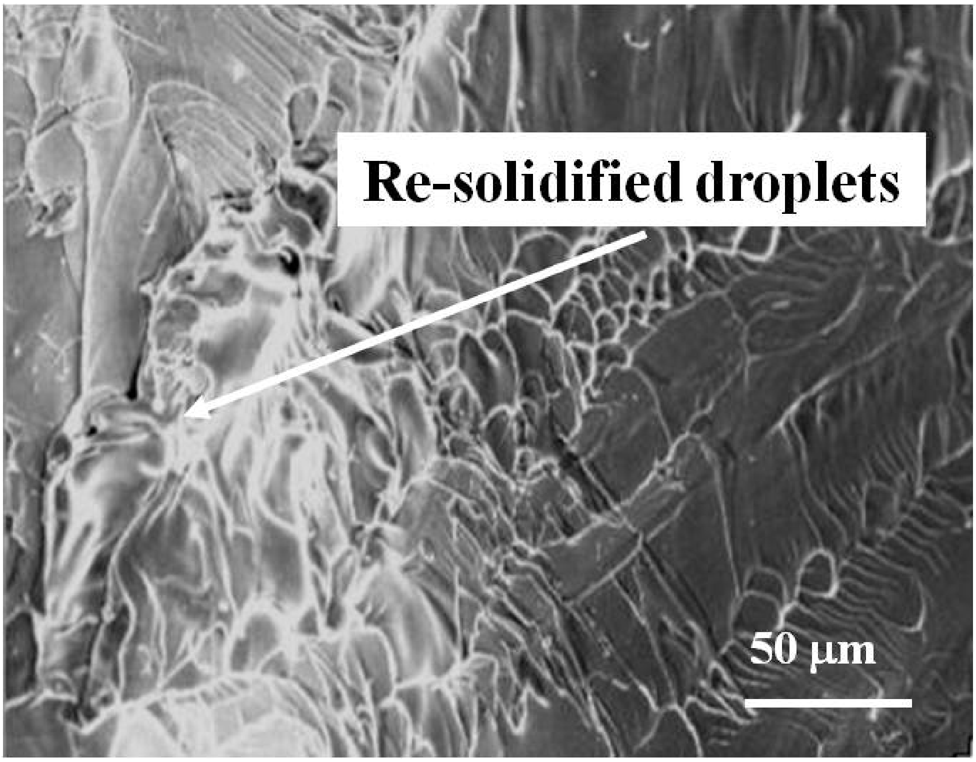

Figure 4.7 Fracture morphologies of the deformed $Cu_{50}Zr_{43}Al_7$ BMG, showing the resolidified-like droplets.

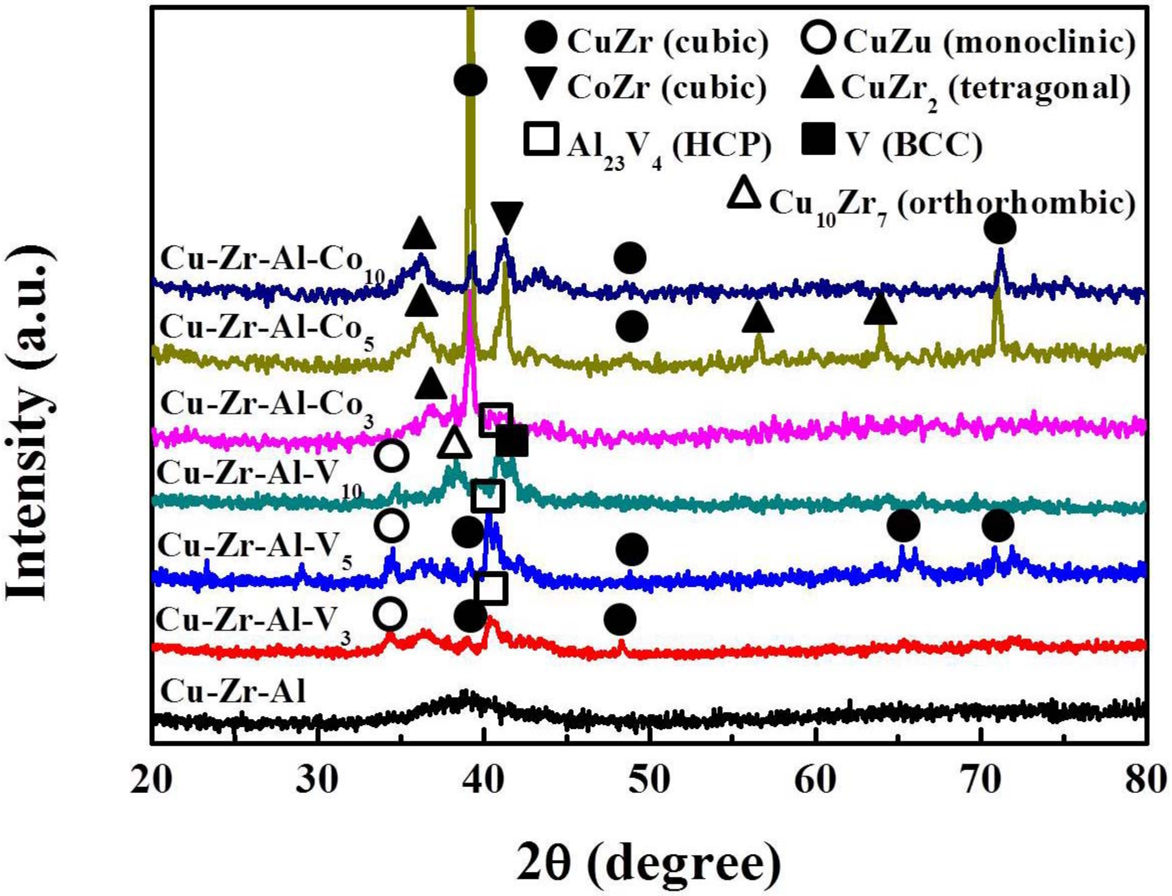

Figure 4.8 XRD curves for the alloys with V and Co contents from 0 to 10 at%.

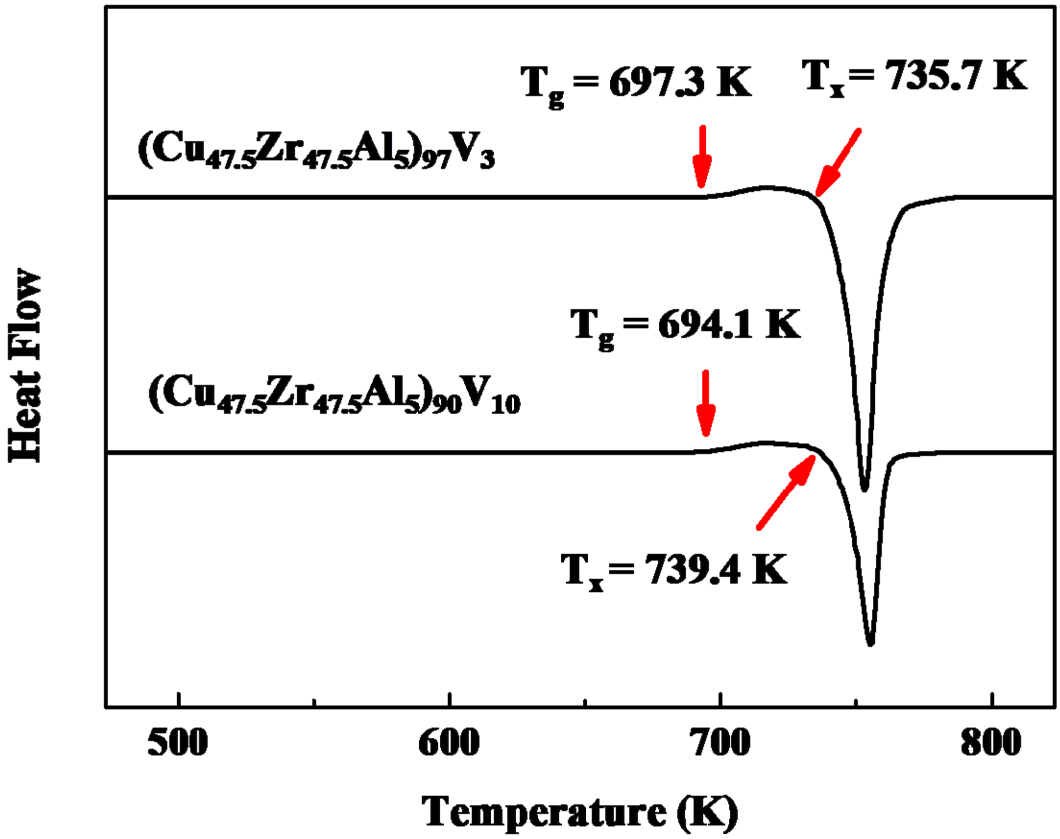

Figure 4.9 DSC curves for the two alloys with V contents of 3 and 10 at%.

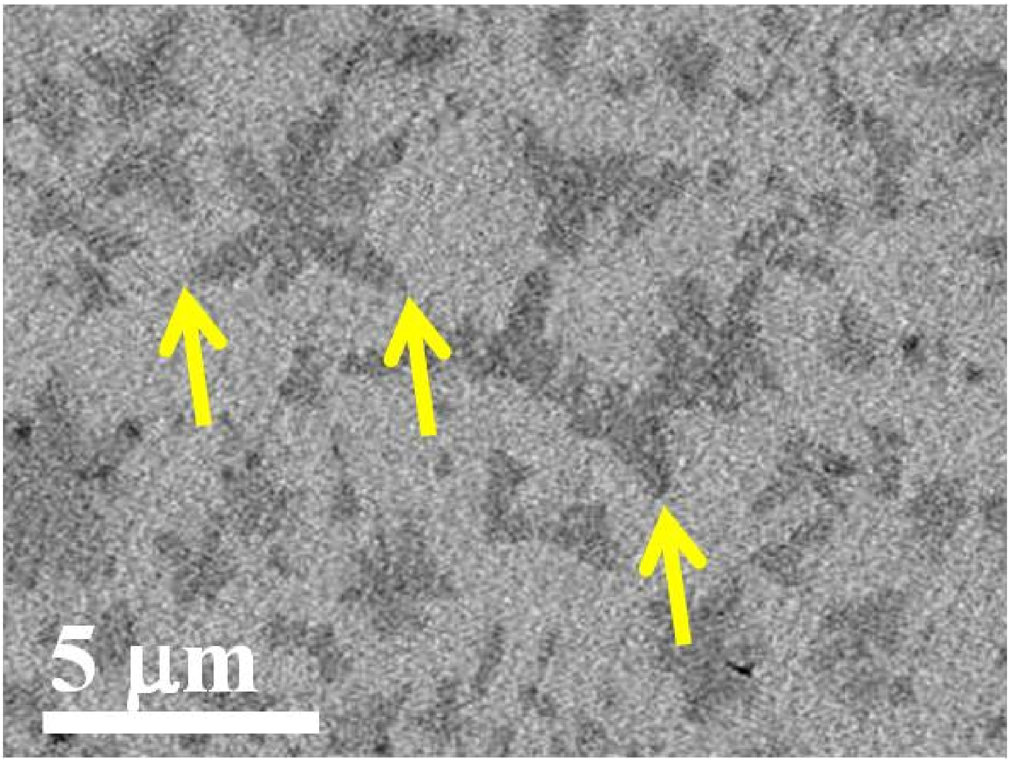

Figure 4.10 The backscattered electron image (BEI) SEM micrographs showing the as cast $(Cu_{47.5}Zr_{47.5}Al_5)_{97}V_3$ alloy microstructures, the sharp dendritic gray phases (as indicated by arrows) are the V-rich phases (including pure V and $Al_{23}V_4$).

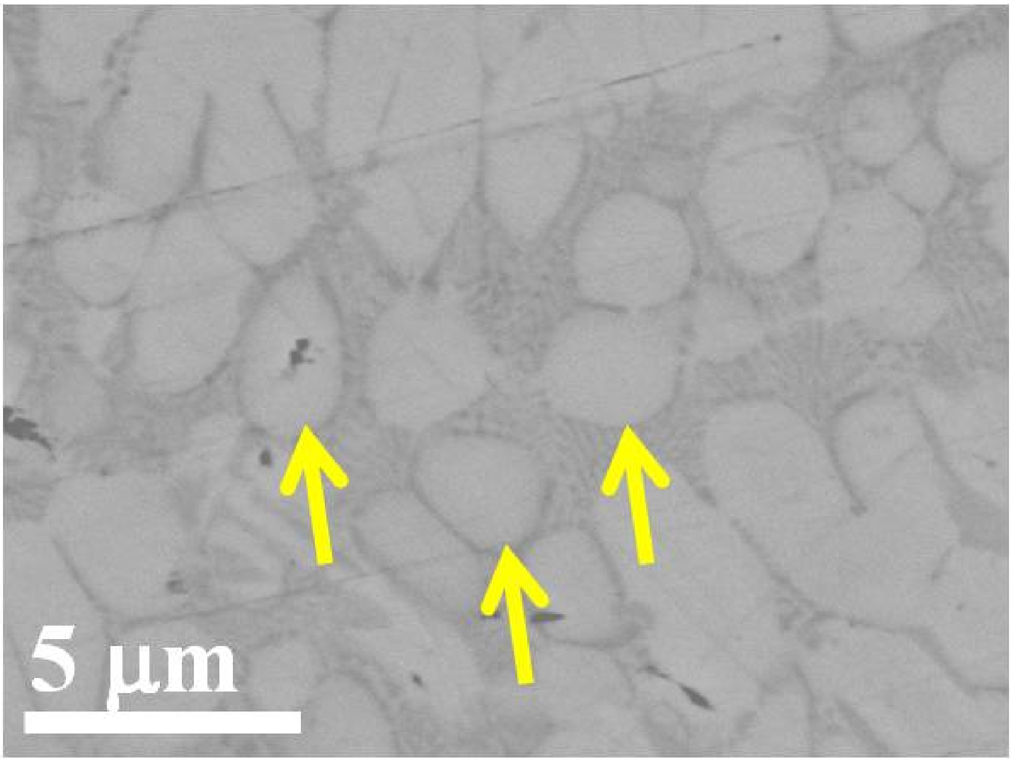

Figure 4.11 The backscattered electron image (BEI) SEM micrographs showing the as cast $(Cu_{47.5}Zr_{47.5}Al_5)_{97}Co_3$ alloy microstructures, the rounded brighter precipitated phases (as indicated by arrows) are the Co_2Zr plus minor $CuZr_2$.

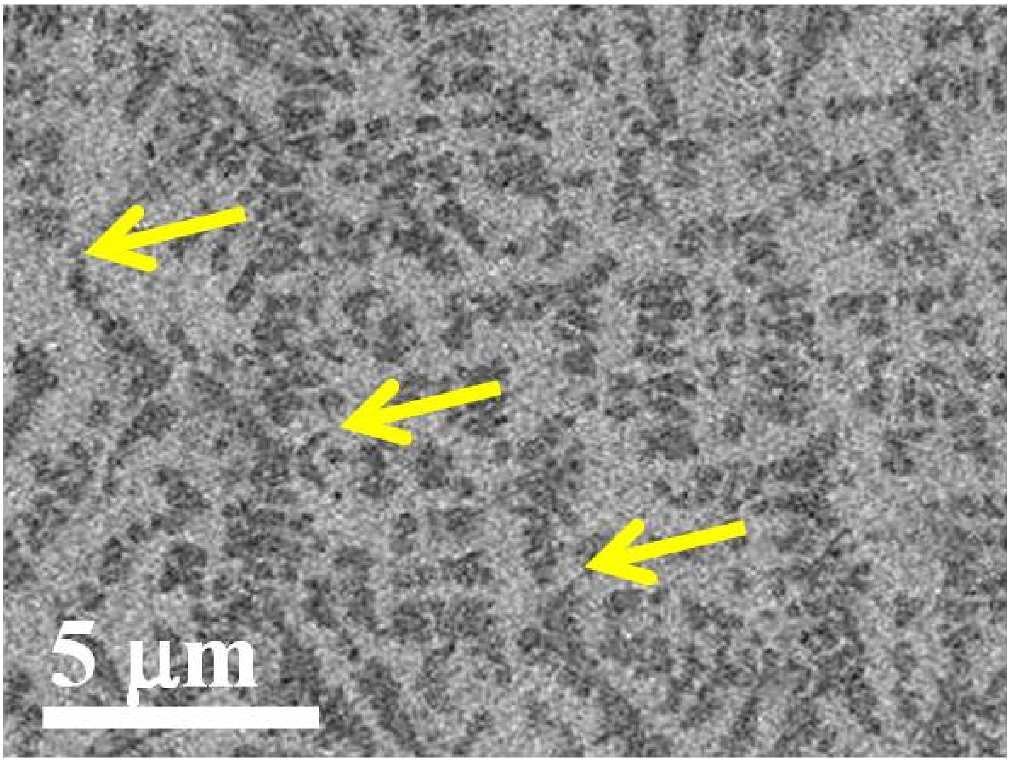

Figure 4.12 The backscattered electron image (BEI) SEM micrographs showing the as cast $(Cu_{47.5}Zr_{47.5}Al_5)_{90}V_{10}$ alloy microstructures, the sharp dendritic gray phases (as indicated by arrows) are the V-rich phases (including pure V and $Al_{23}V_4$).

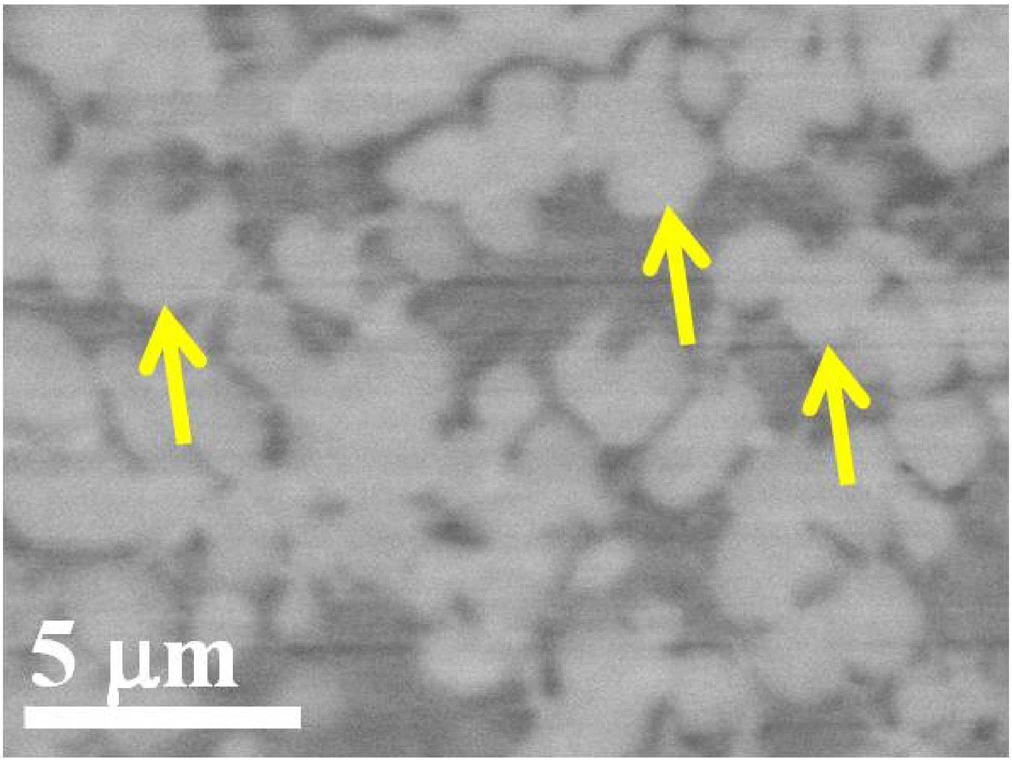

Figure 4.13 The backscattered electron image (BEI) SEM micrographs showing the as cast $(Cu_{47.5}Zr_{47.5}Al_5)_{90}Co_{10}$ alloy microstructures, the rounded brighter precipitated phases (as indicated by arrows) are the Co_2Zr plus minor $CuZr_2$.

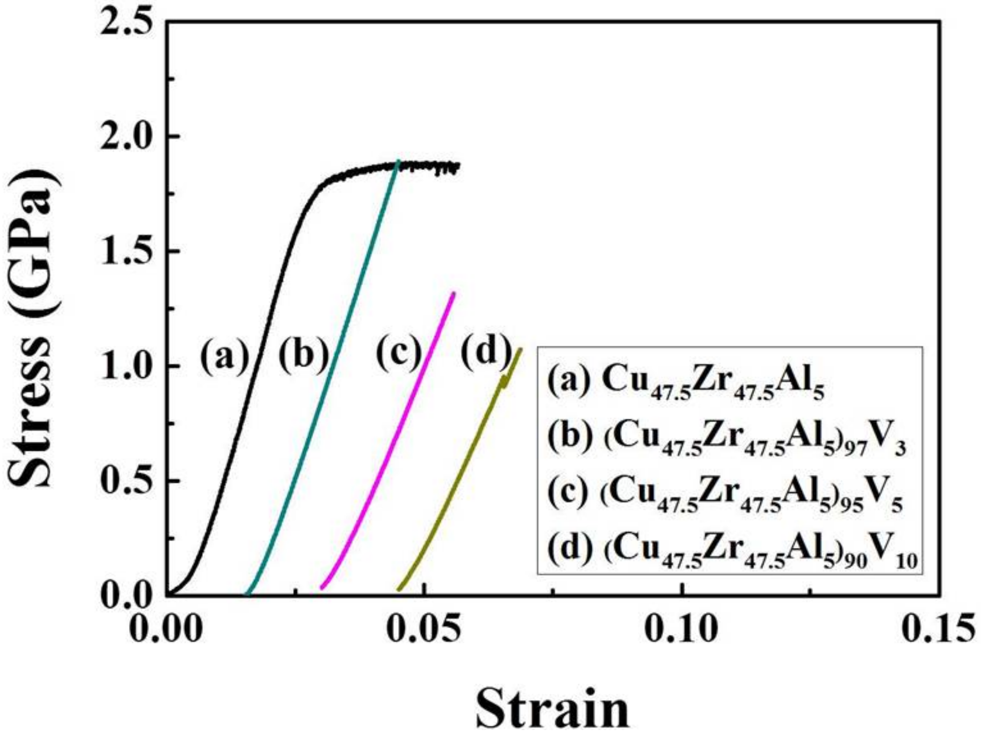

Figure 4.14 Engineering stress and strain curves for the four CuZrAl-V alloys under study.

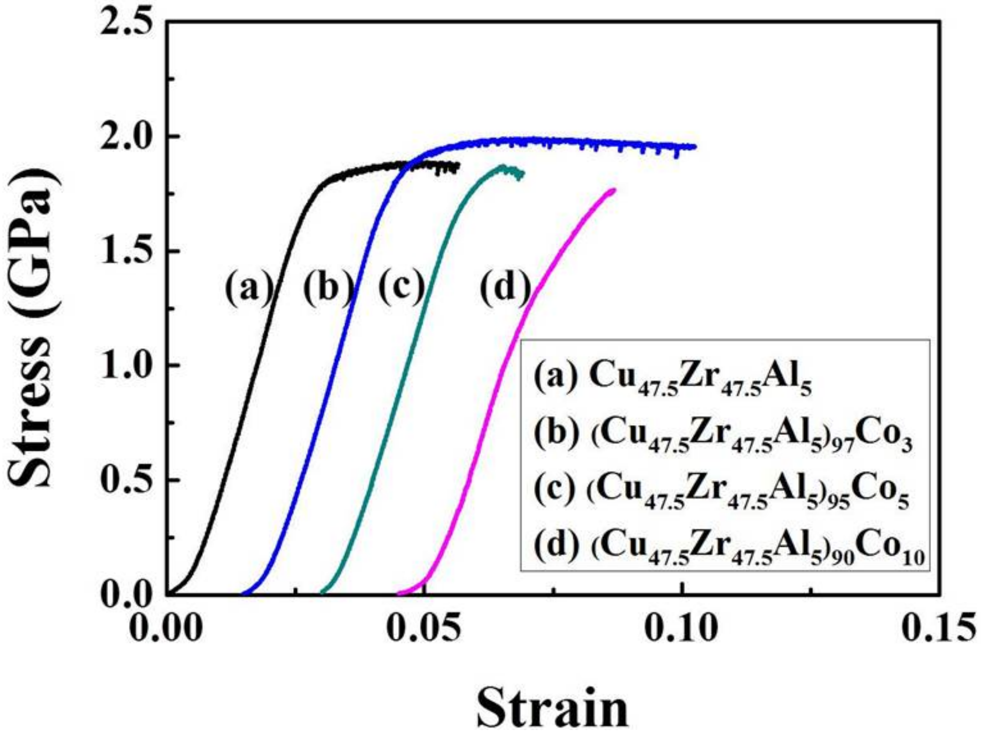

Figure 4.15 Engineering stress and strain curves for the four CuZrAl-Co alloys under study.

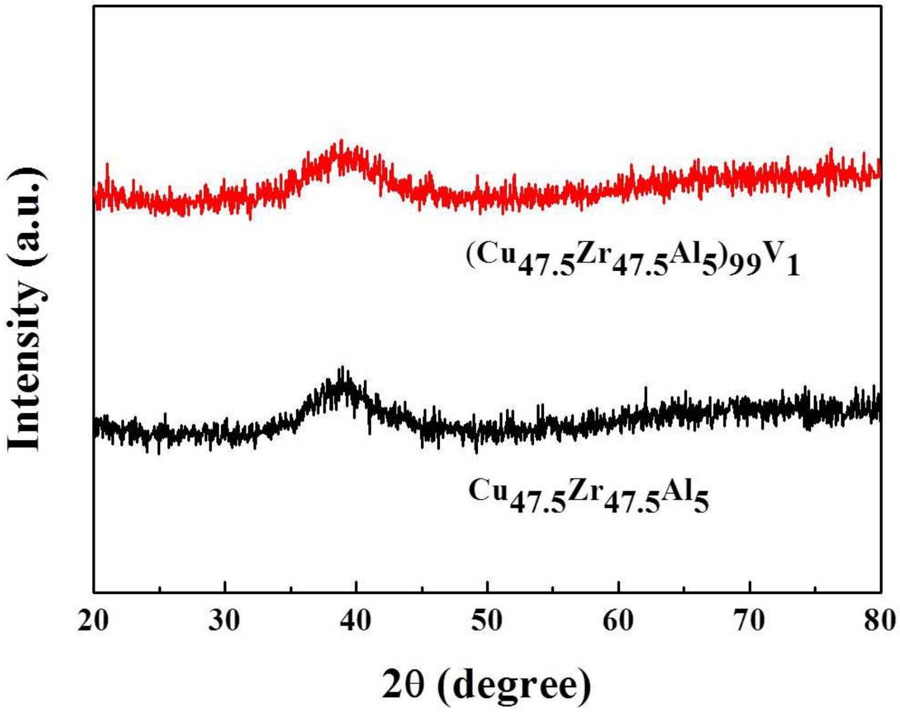

Figure 4.16 XRD curves for the Cu-Zr-Al-V alloys with V contents of 0 and 1 at%.

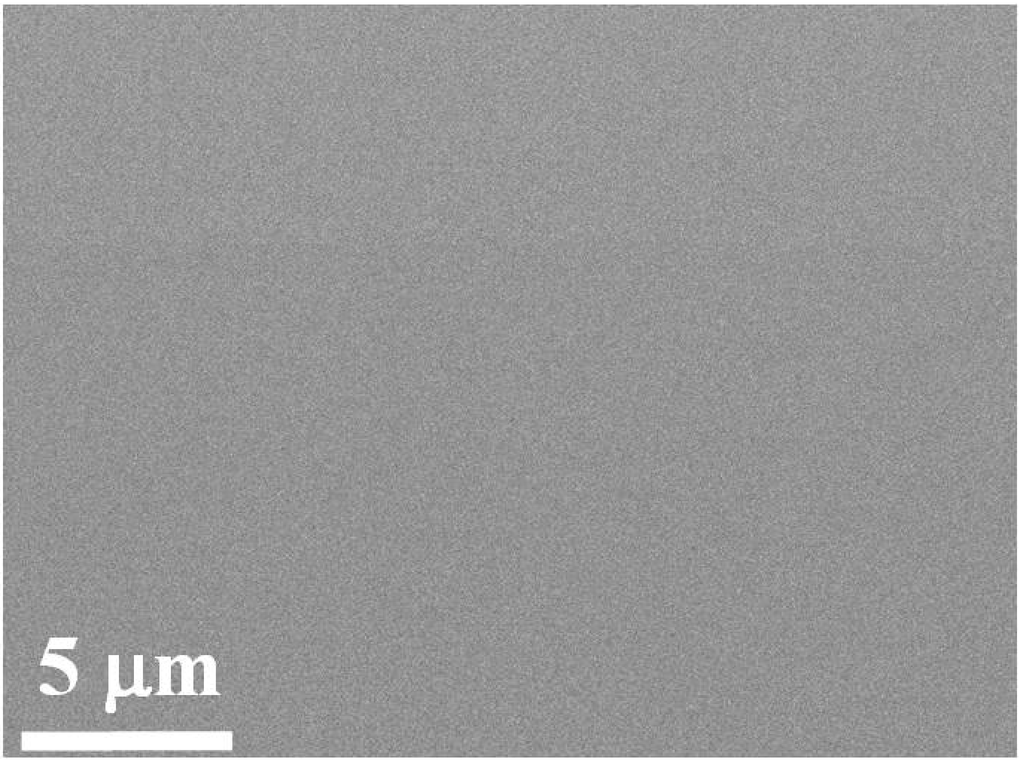

Figure 4.17 SEM micrographs showing the as cast $Cu_{47.5}Zr_{47.5}Al_5$ alloy microstructures, there is no phase contrast, indicating a homogeneous microstructure without any micro-sized phase.

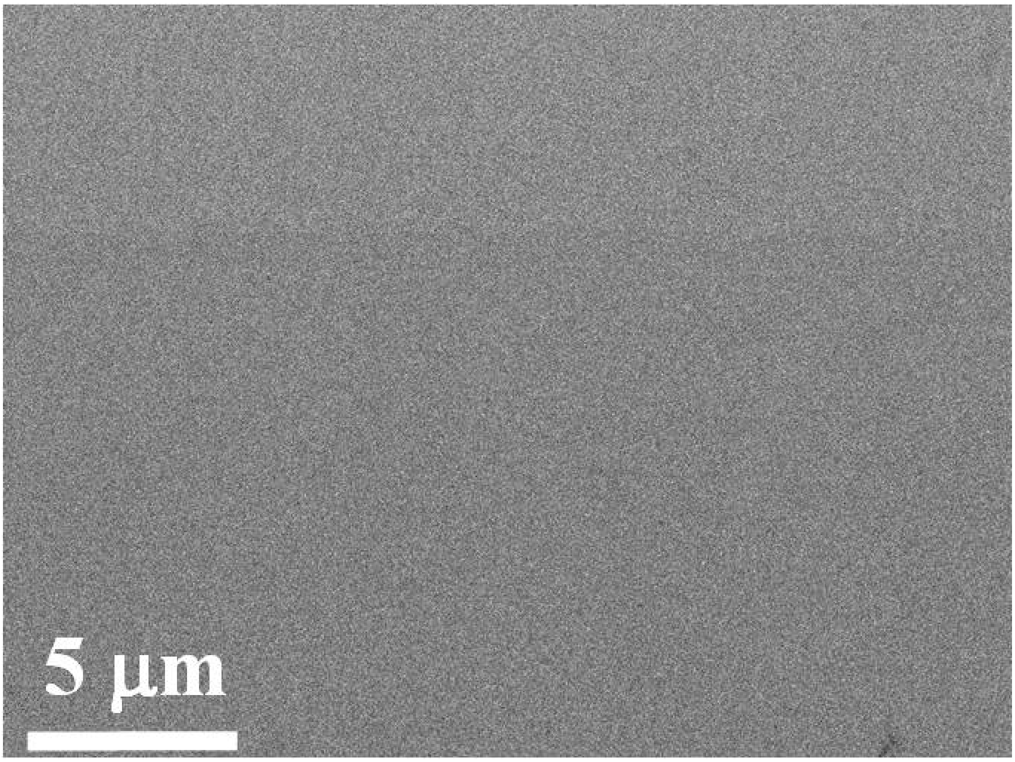

Figure 4.18 SEM micrographs showing the as cast $(Cu_{47.5}Zr_{47.5}Al_5)_{99}V_1$ alloy microstructures, there is no phase contrast, indicating a homogeneous microstructure without any micro-sized phase.

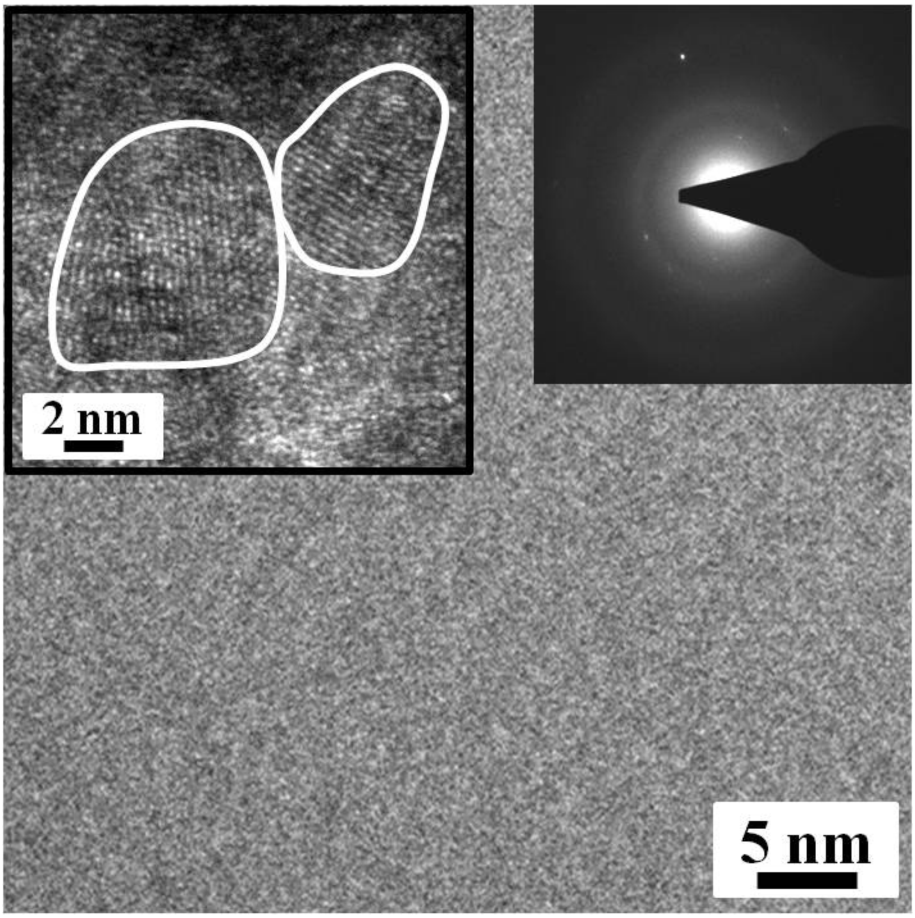

Figure 4.19 TEM bright field images with the inserted high resolution images and associated diffraction patterns for the deformed $Cu_{47.5}Zr_{47.5}Al_5$ sample. The few fine nano B2 phase is not apparent in the diffraction pattern, but can be clearly seen in high resolution micrographs where the fine B2 CuZr precipitates are imbedded in the amorphous matrix.

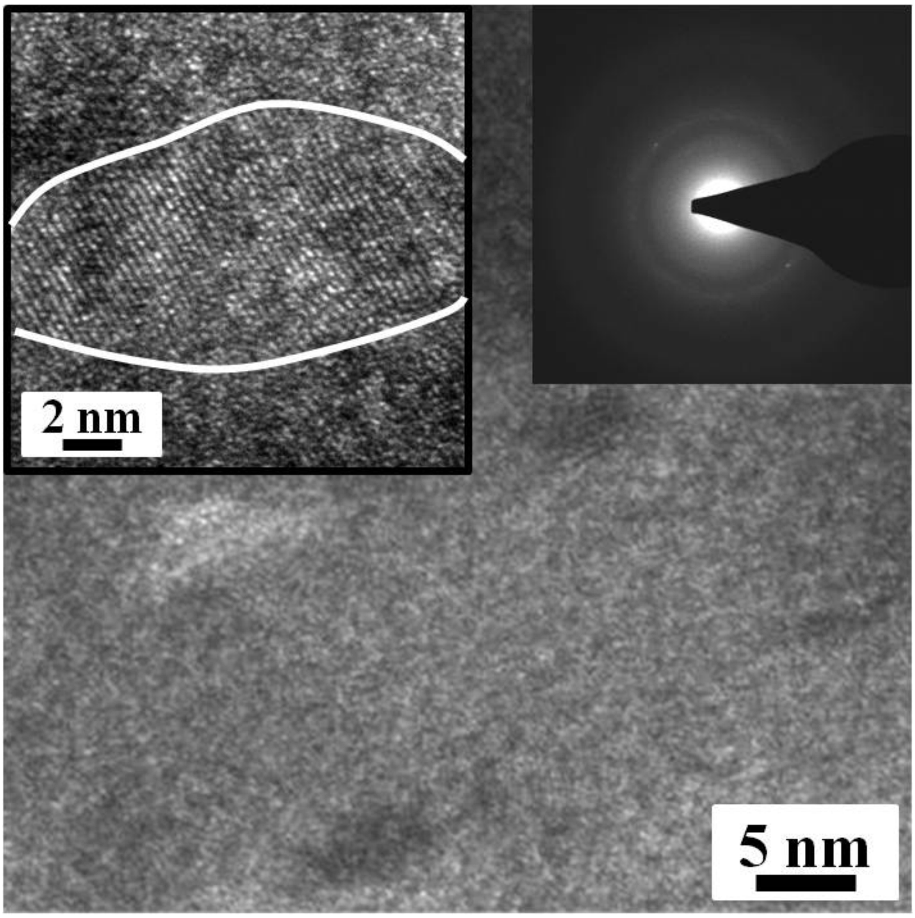

Figure 4.20 TEM bright field images with the inserted high resolution images and associated diffraction patterns for the deformed $(Cu_{47.5}Zr_{47.5}Al_5)_{99}V_1$ sample. The few fine nano B2 phase is not apparent in the diffraction pattern, but can be clearly seen in high resolution micrographs where the fine B2 CuZr precipitates are imbedded in the amorphous matrix.

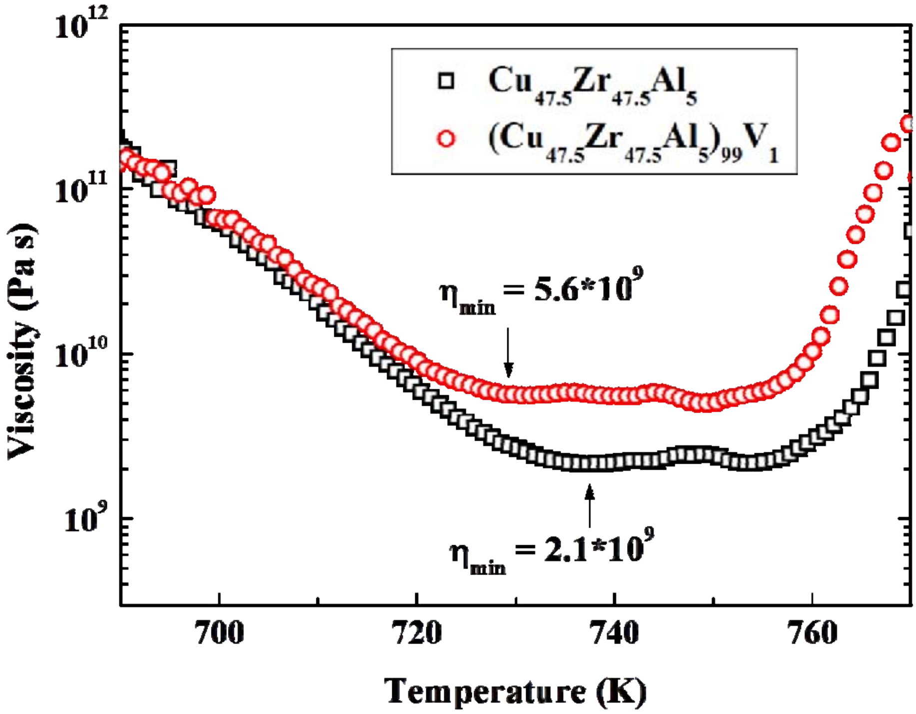

Figure 4.21 Variation of viscosity (measured by TMA) as a function temperature for the $Cu_{47.5}Zr_{47.5}Al_5$ and $(Cu_{47.5}Zr_{47.5}Al_5)_{99}V_1$ alloys.

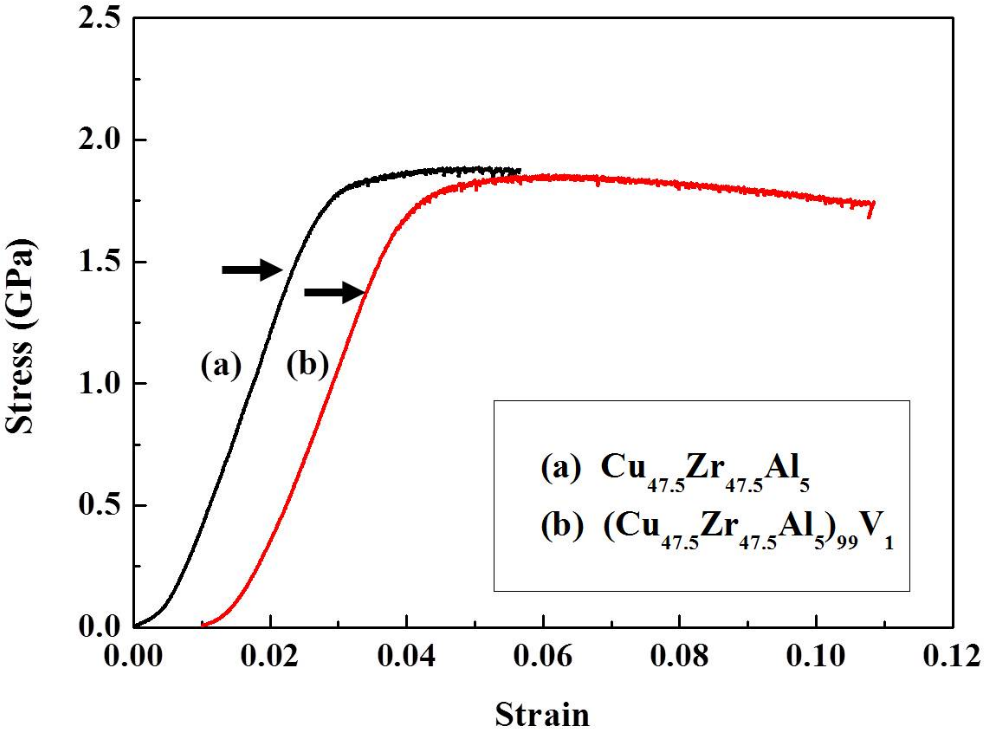

Figure 4.22 Engineering stress and strain curves for the $Cu_{47.5}Zr_{47.5}Al_5$ and $(Cu_{47.5}Zr_{47.5}Al_5)_{99}V_1$ alloys studied. The curve of $(Cu_{47.5}Zr_{47.5}Al_5)_{99}V_1$ sample is shifted to the right by 0.01 strain for easy comparison.

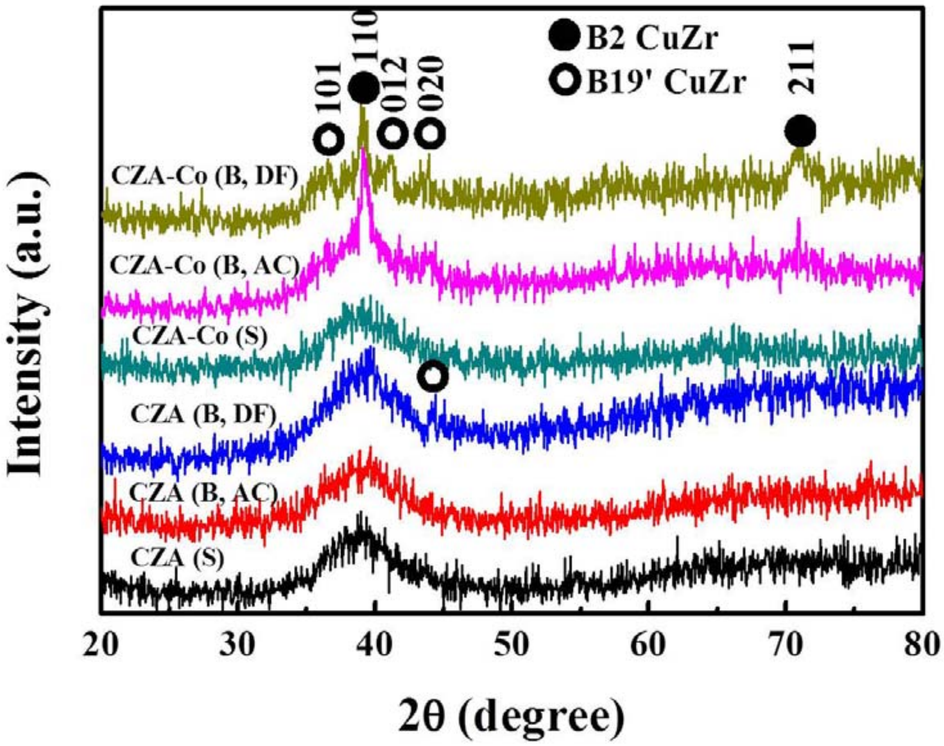

Figure 4.23 XRD patterns of the $Cu_{47.5}Zr_{47.5}Al_5$ (CZA) and $Cu_{47.5}Zr_{48}Al_4Co_{0.5}$ (CZA-Co), cast by the S or B mold under the as-cast (AC) or deformed (DF) condition. The patterns for the CZA and CZA-Co cast by the S mold, under the AC and DF conditions are both the same; so only the AC scans are shown.

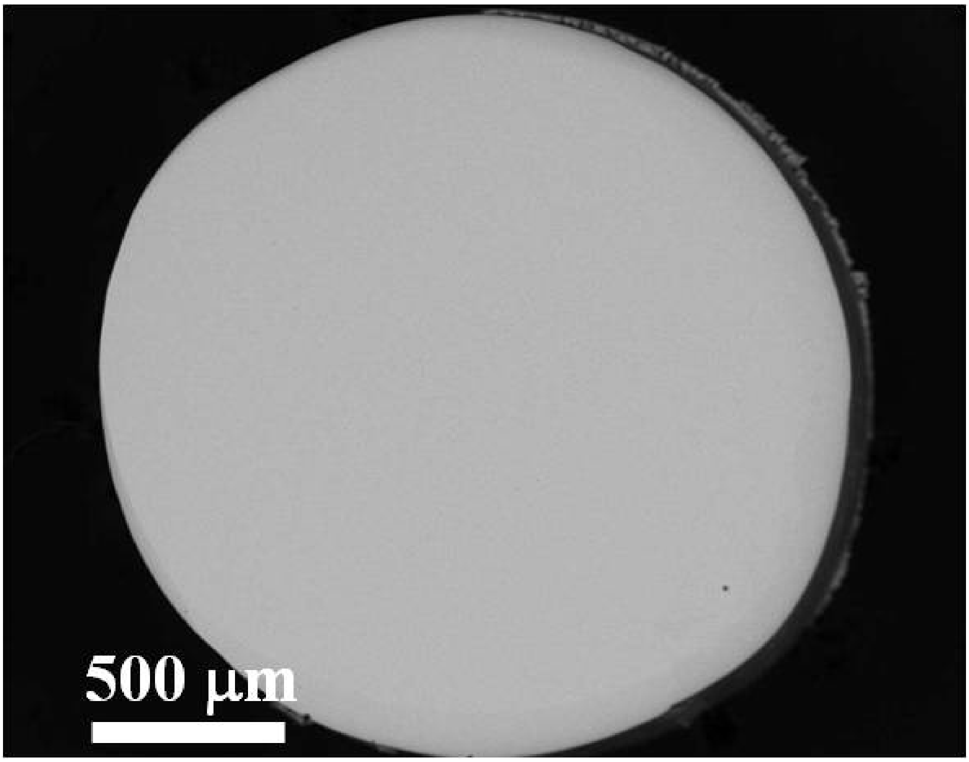

Figure 4.24 The backscattered electron image (BEI) SEM micrographs showing the microstructure of $Cu_{47.5}Zr_{48}Al_4Co_{0.5}$ alloy cast by the S mold, showing a monolithic amorphous structure without micro-sized precipitates.

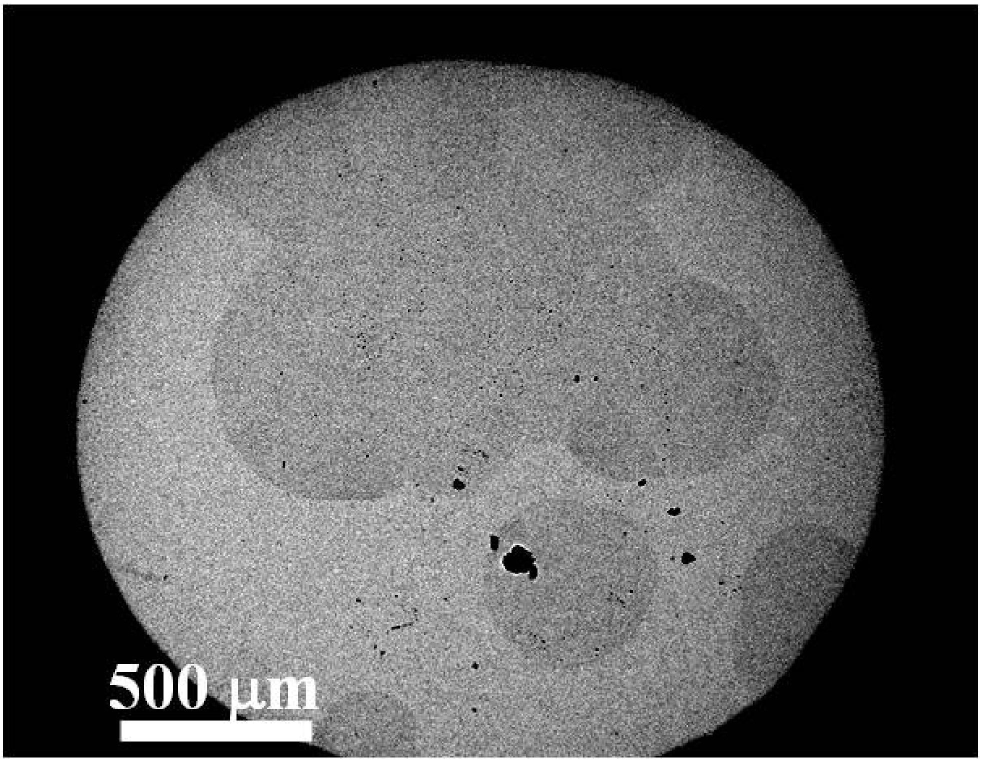

Figure 4.25 The backscattered electron image (BEI) SEM micrographs showing the microstructures of $Cu_{47.5}Zr_{48}Al_4Co_{0.5}$ alloy cast by the B mold, showing several near-spherical-shaped gray regions full of the CuZr nanophases embedded in the amorphous matrix.

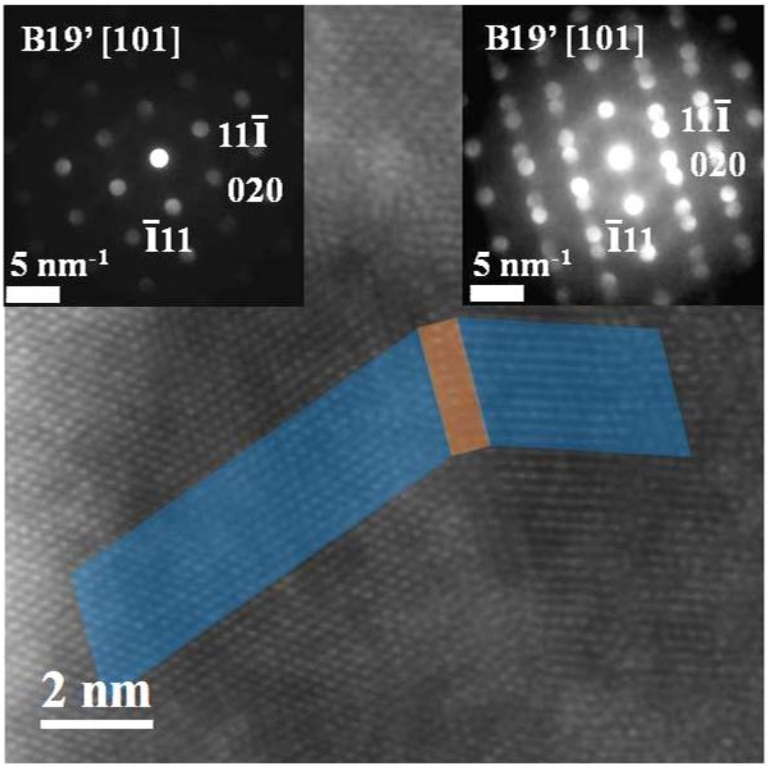

Figure 4.26 The TEM HR image presents the twin associated with the B19' phase in the $Cu_{47.5}Zr_{47.5}Al_5$ deformed sample cast by the B mold, with the inserted selected area diffraction (SAD) patterns for areas without (left) and with (right) twining.

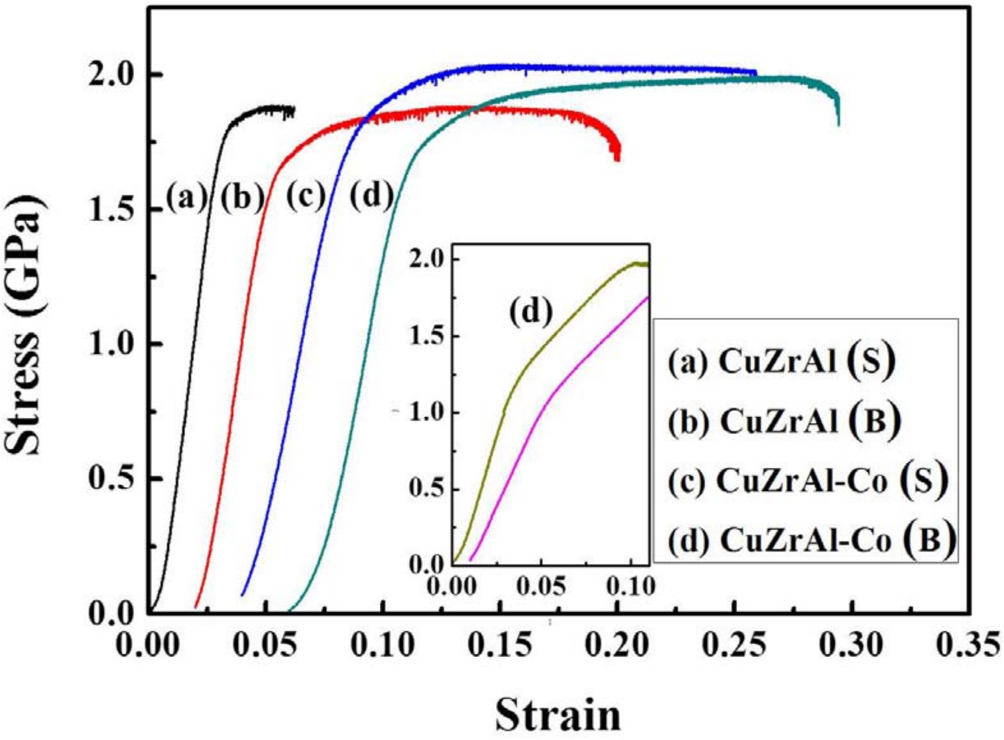

Figure 4.27 Engineering stress and strain curves for the four alloys studied. For easy observation, each stress-strain curve is shifted horizontally. The inserted curves show the apparent work hardening behavior in the Co-containing alloy cast by the B mold.

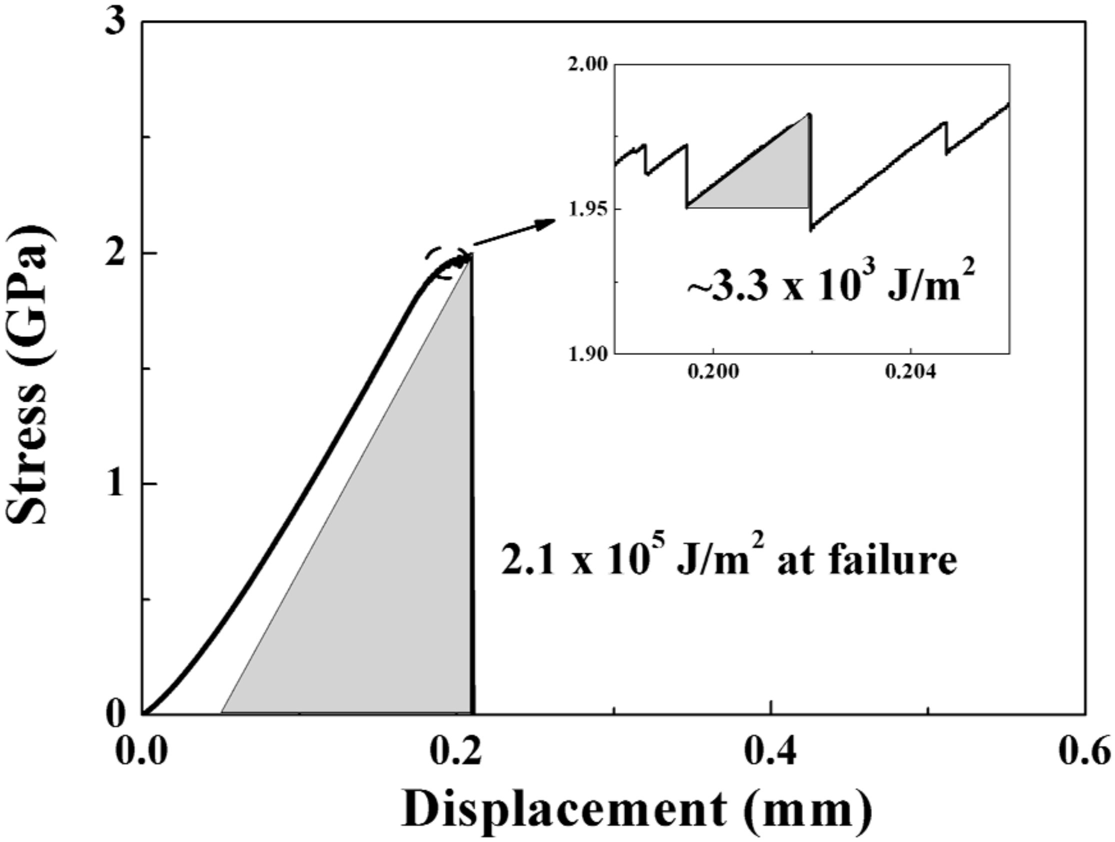

Figure 5.1 The compressive load-displacement curve of the $Cu_{50}Zr_{43}Al_7$ BMG. The triangles represent the energy release during one serration and at failure.

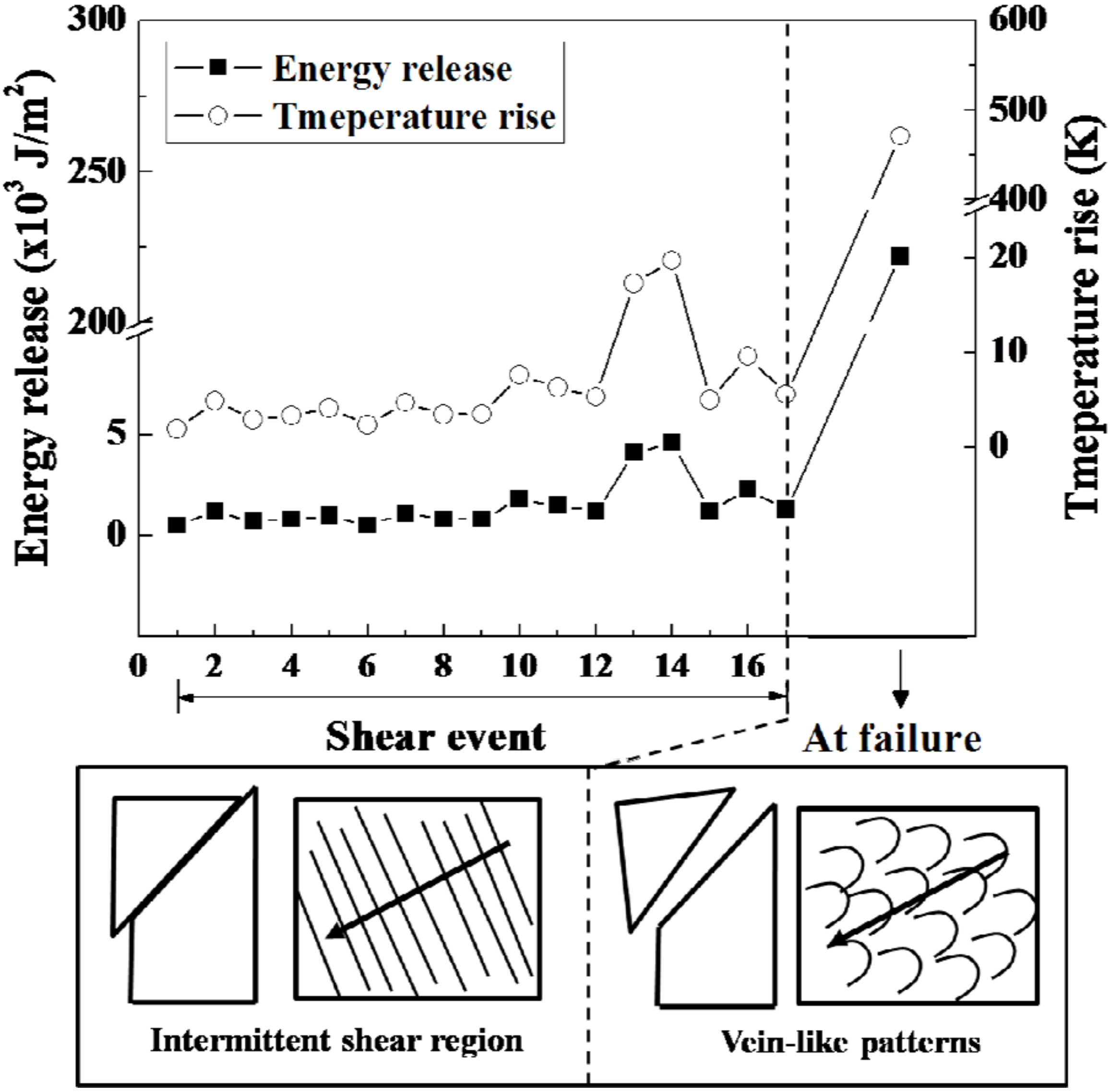

Figure 5.2 The dependences of energy releases and the corresponding temperature rises as a function of shear events during plastic deformation for the $Cu_{50}Zr_{43}Al_7$ BMG, together with fracture morphologies.

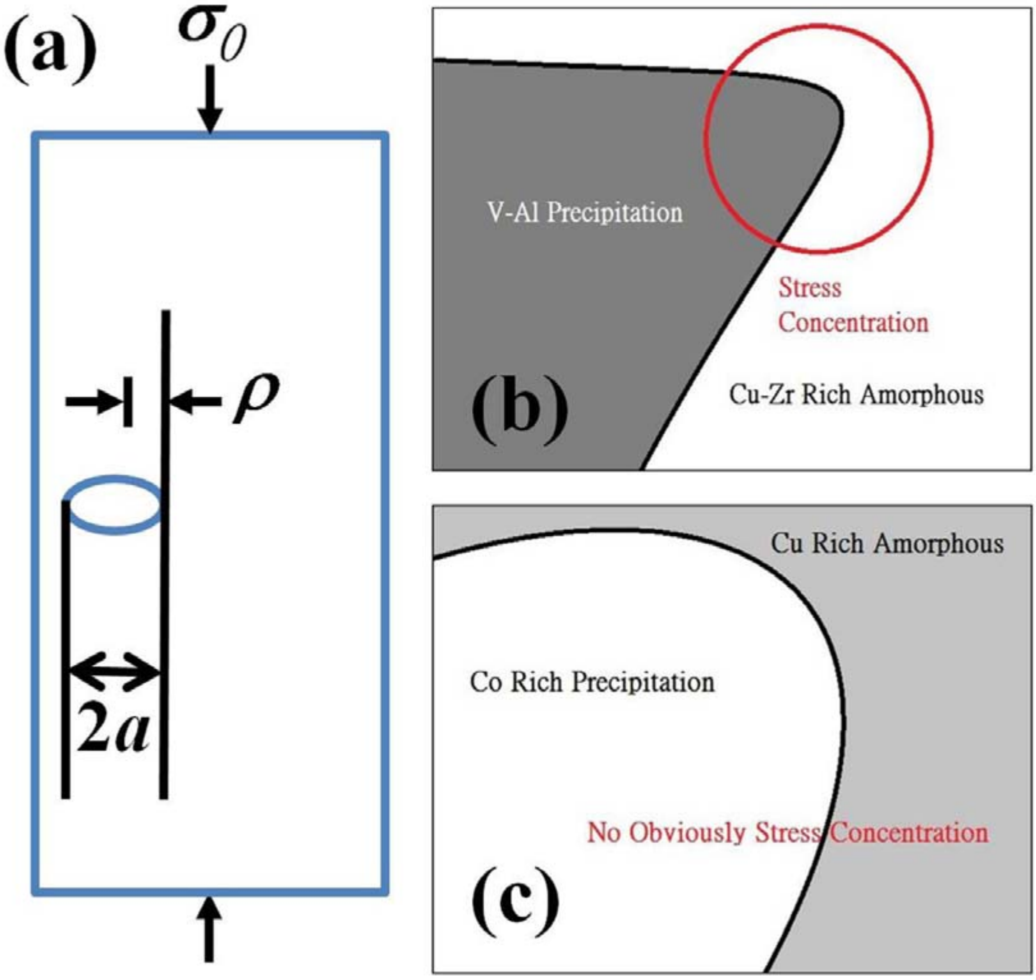

Figure 5.3 (a) Nomenclature for the geometry and coordinate axes for stress analysis in the specimen with a notch under compression. (b) and (c) show the difference in stress concentration with different precipitation shapes in the V and Co-containing alloy systems.

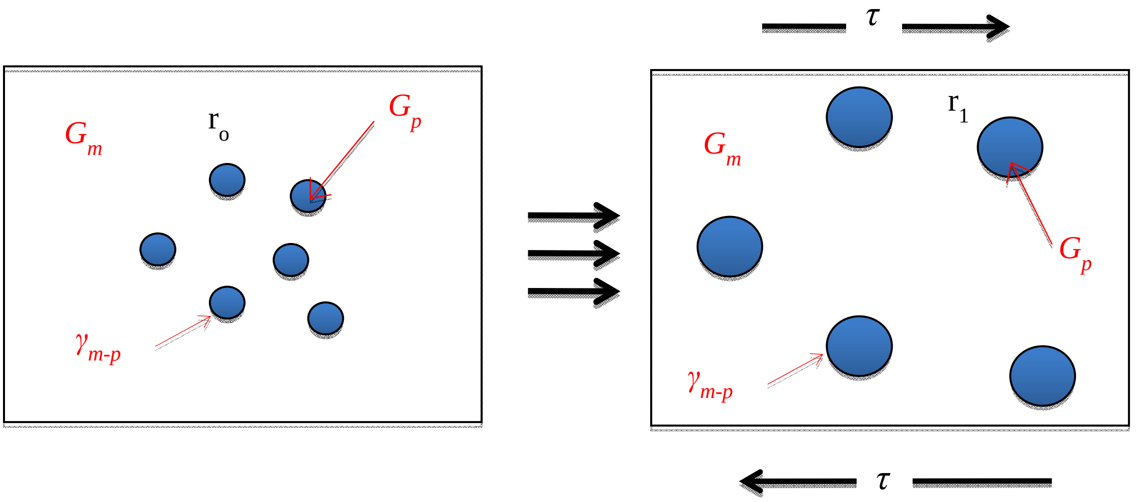

Figure 5.4 The initial and final energy densities of the system.

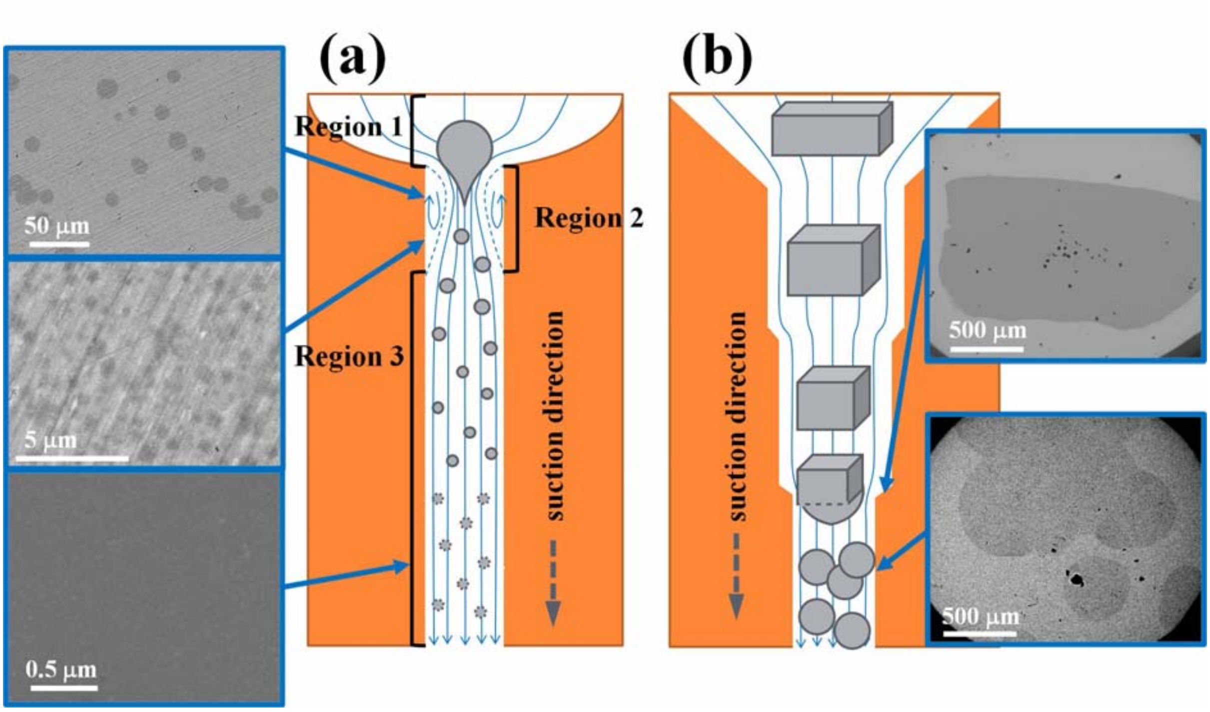

Figure 5.5 Schematic drawings of the evolution of the liquid-phase separation region from the top ingot melt down to the 2 mm pipe: (a) the S mold, showing the violent separation into small droplets with the observed SEM images at different locations, and (b) the B mold, showing the large near-rectangle-shaped separation region gradually change its shape an dispersion into the final near-spherical regions with the corresponding SEM images.

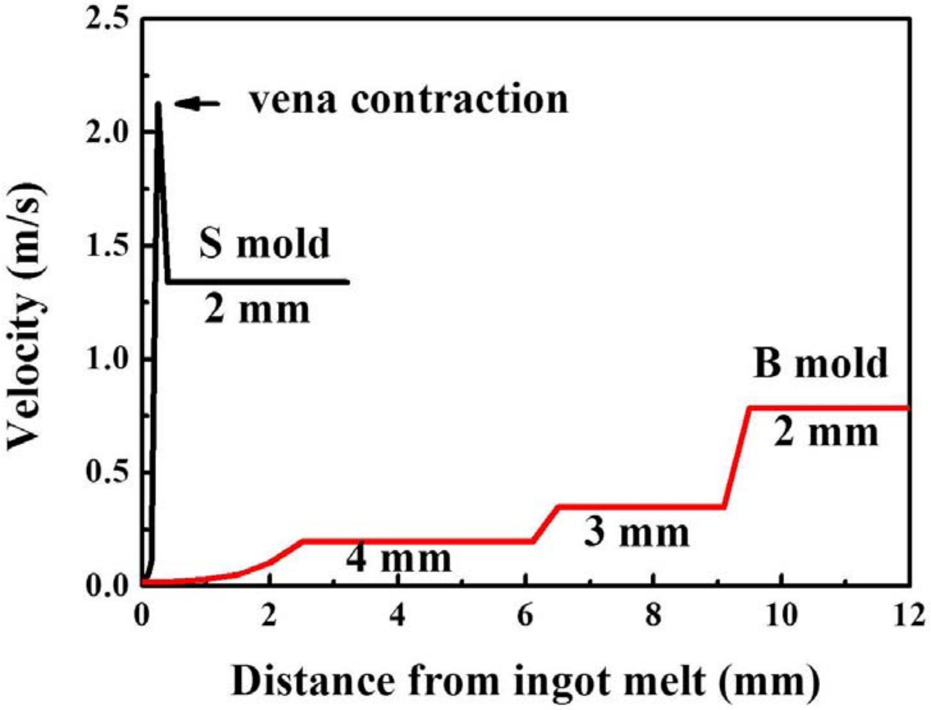

Figure 5.6 The variation of the fluid velocity at different locations with different distances from the upper ingot melt, in the case of the S or B mold.